CHALMERS
UNIVERSITY OF TECHNOLOGY

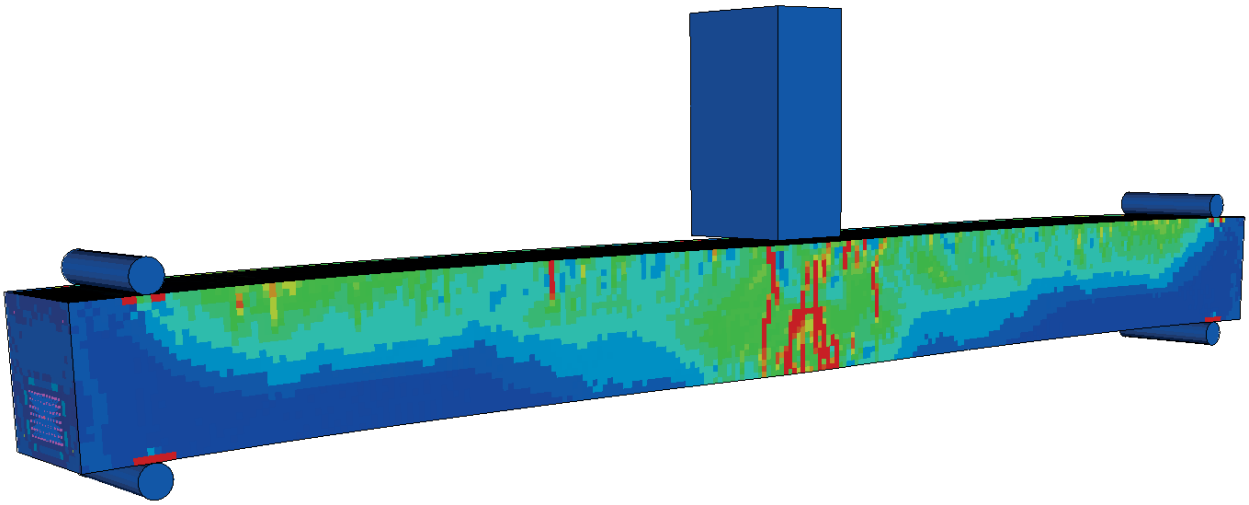

Structural Behaviour of Prestressed Concrete Beams During Impact Loading

Evaluation of Concrete Material Models and Modelling of Prestressed Concrete in LS-DYNA

Master's thesis in the Master's Programme Structural Engineering and Building Technology

ADAM JOHANSSON
JOHAN FREDBERG

Department of Civil and Environmental Engineering
Division of Structural Engineering
Concrete Structures
CHALMERS UNIVERSITY OF TECHNOLOGY
Gothenburg, Sweden 2015
Master's thesis 2015:74

MASTER'S THESIS 2015:74

Structural Behaviour of Prestressed Concrete Beams During Impact Loading

Evaluation of Concrete Material Models and Modelling of Prestressed Concrete in LS-DYNA

Master's thesis in the Master's Programme Structural Engineering and Building Technology

ADAM JOHANSSON
JOHAN FREDBERG

Department of Civil and Environmental Engineering
Division of Structural Engineering
Concrete Structures
CHALMERS UNIVERSITY OF TECHNOLOGY

Gothenburg, Sweden 2015

Structural Behaviour of Prestressed Concrete Beams During Impact Loading
Evaluation of Concrete Material Models and Modelling of Prestressed Concrete in LS-DYNA
ADAM JOHANSSON
JOHAN FREDBERG

Master's thesis 2015:74
ISSN 1652-8557
Department of Civil and Environmental Engineering
Division of Structural Engineering
Concrete Structures
Chalmers University of Technology
SE-412 96 Gothenburg
Sweden
Telephone: +46 (0)31-772 1000

Cover:
Crack pattern on a prestressed concrete beam in upward deflection after impact of a drop-weight

Chalmers Reproservice
Gothenburg, Sweden 2015

Structural Behaviour of Prestressed Concrete Beams During Impact Loading
Evaluation of Concrete Material Models and Modelling of Prestressed Concrete in LS-DYNA
Master's thesis in the Master's Programme Structural Engineering and Building Technology
ADAM JOHANSSON
JOHAN FREDBERG
Department of Civil and Environmental Engineering
Division of Structural Engineering
Concrete Structures
Chalmers University of Technology

ABSTRACT

There are numerous structures that use prestressed concrete such as nuclear power plants and protective shelters. There is always the possibility of severe collisions, either it is intentional or unintentional. Therefore it is very important to be aware of the effects of prestressing in a beam subjected to dynamic loads.

Through numerical analysis using LS-DYNA, a reinforced concrete beam was subjected to static loads and secondly a drop weight experiment was simulated. This was done as both a verification of the modelling techniques and an evaluation of the three material models CDPM2, CSCM and Winfrith. A suitable material model was then used to test a method where temperature was applied to the reinforcement in order to simulate a prestressing. An equivalent and a prestressed beam was then compared for both static and dynamic loads to investigate the effect of prestressing.

From the evaluation of material models it was found that all the models gave good results both in the static and dynamic cases. CDPM2 was shown to be the better, but due to technical issues with LS-DYNA CSCM was used to model the prestressing. The temperature method to model prestressing behaved in a satisfactory way, although some control over the exact prestressing force was lost.

The prestressed beams behaved in a good way during static loads with a delayed crack initiation and increased capacity in Stadium I i.e uncracked state. The results from drop weight simulations on the prestressed beams showed an increased crack pattern in the top part of the beam compared to the equivalent beam and as a results an increased upward deflection for low velocity impacts.

Keywords: Prestressing, CDPM2, CSCM, Winfrith, Impact, Drop-weight

CONTENTS

Abstract i

Contents iii

Preface v

Nomenclature vii

1 Introduction 1
1.1 Background . . . 1
1.2 Aim and objectives . . . 1
1.3 Methodology . . . 1
1.4 Limitations . . . 2
1.5 Outline of thesis . . . 2

2 Basic Theory of dynamics 4
2.1 Velocity and acceleration . . . 4
2.2 Work and kinetic energy . . . 4
2.3 Momentum and impulse . . . 6
2.4 Free vibration . . . 7
2.5 Forced vibrations . . . 9
2.6 Equation of Motion . . . 10
2.7 Central difference method . . . 11

3 Material responses 12
3.1 Linear elastic material . . . 12
3.2 Ideal plastic material . . . 13
3.3 Elastoplastic and trilinear materials . . . 14
3.4 Damage formulation during loading and unloading . . . 15
3.4.1 Plasticity model . . . 15
3.4.2 Damage model . . . 15

4 Concrete Theory 17
4.1 Plain concrete . . . 17
4.2 Reinforced concrete . . . 18
4.3 Prestressed concrete . . . 19
4.4 Concrete subjected to dynamic loading . . . 21
4.4.1 Strain rate . . . 21
4.4.2 Forced crack path due to fast loading rate . . . 23
4.4.3 Inertia forces . . . 23
4.4.4 Fracture behaviour due to strain rate effects . . . 25
4.4.5 Wave propagation . . . 30

5 Beam tranformation SDOF **32**
5.1 Transformation factor for the mass . . . 33
5.2 Transformation factor for the force . . . 34
5.3 Transformation factor for the stiffness . . . 34
5.3.1 κ_k for a linear elastic material . . . 35
5.3.2 κ_k for a ideal plastic material . . . 37
5.3.3 κ^{elpl} for trilinear material . . . 38
5.4 SDOF of a prestressed beam . . . 38

6 FE-Modeling techniques **41**
6.1 Material Models . . . 41
6.1.1 Concrete damage plasticity model 2 . . . 41
6.1.2 Continuous surface cap model . . . 44
6.1.3 Winfrith . . . 46
6.2 Reinforcement modelling . . . 48
6.2.1 Reinforcement concrete share nodes . . . 48
6.2.2 Constrained Lagrange in solids, CLIS . . . 49
6.3 Solid Elements . . . 50
6.4 Hourglassing . . . 50
6.5 Contact surfaces . . . 51

7 Beam Case I - Drop-weight experiment on a reinforced concrete beam **52**
7.1 Experimental test set-up for Beam Case I . . . 52
7.1.1 Experimental results for Beam Case I . . . 53
7.2 Creation of the FE-model - Beam Case I . . . 54
7.3 Verification of the FE-model - Beam Case I . . . 55
7.3.1 Static load case - Means of verification and verification results . . . 55
7.3.2 Dynamic load case - Means of verification and verification results . . . 58

8 Evaluation of the material models with regard to performance during impact loading **62**
8.1 Static performance . . . 62
8.2 Dynamic performance . . . 65
8.2.1 Mesh convergence . . . 65
8.2.2 Hourglass sensitivity . . . 67
8.2.3 Comparison towards experimental results . . . 70
8.3 Discussion regarding performance of the material models . . . 75
8.3.1 CDPM2-Bilinear . . . 75
8.3.2 CDPM2-Linear . . . 76
8.3.3 CSCM . . . 77
8.3.4 Winfrith . . . 78
8.4 Decision on material model to use for remaining models . . . 79

9 Beam Case II- and III - Drop-weight analysis on a reinforced prestressed beam and an equivalent reinforced beam **80**
9.1 Beam Case II - Reinforced- and prestressed beam . . . 80
9.2 Beam Case III - Equivalent reinforced beam . . . 81
9.3 Creation of the FE-models for Beam Case II- and III . . . 82

9.3.1 Modeling of the prestressing effect . . . 82
9.4 Creation of the FE-model - Beam Case III . . . 84
9.5 Verification of the FE-models - Beam Case II- and III . . . 85
9.5.1 Means of verification and verification results . . . 85

10 Results from drop-weight analyses on Beam Case II and Beam Case III - Effect of prestressing 92
10.1 0.15m drop-height . . . 92
10.2 1.0m drop-height . . . 95
10.3 2.0m drop-height . . . 98
10.4 3.0m drop-height . . . 100

11 Discussion 102
11.1 The effect of prestressing on dynamically loaded concrete beams . . . 102
11.2 Discussion about modelling technique and LS-DYNA . . . 103
11.3 Discussion about material model evaluation . . . 103
11.4 Discussion about SDOF . . . 104
11.5 Further Research . . . 104

12 References 105

Appendix A Material models in LS-DYNA 107
A.1 CDPM2 . . . 107
A.2 CSCM . . . 107
A.3 Winfrith . . . 108
A.4 Steel . . . 108
A.5 Rigid bodies . . . 109

Appendix B Prestressed Beam LS-DYNA 110

Appendix C SDOF calculations in MATLAB 119
C.1 Main algorithm . . . 119
C.2 Resisting Forces . . . 123
C.3 Central Difference Method . . . 124

Appendix D Reinforcement with different material models 126

Appendix E Mathcad calculations 128
E.1 Capacity of Beam Case 1 . . . 129
E.2 Verification of Beam Case 2 during tensioning . . . 139
E.3 Capacity of Beam Case 2 . . . 144
E.4 Capacity of Beam Case 3 . . . 154

PREFACE

In this Master's thesis numerical analysis using LS-DYNA on reinforced and prestressed concrete were performed. To investigate the influence of prestressing during dynamic loading, and to evaluate the material model CDPM2.

The project was carried out in collaboration with ÅF consult and the Department of Civil and Environmental Engineering, Division of structural Engineering. The supervisors for the project where Senior Lecturer Joosef Leppänen at Chalmers, Frida Holmquist and Emil Carlson at ÅF. The work was carried out at ÅF in Gothenburg, Sweden.

We would like to start by thanking Joosef Leppänen for all of his invaluable guidance and help in the capacity of both supervisor and examiner. We also would like to show our appreciation to Frida Holmquist and Emil Carlson for all of their help and valuable feedback during the project. Also a big thank you to the entire department at ÅF for being very welcoming and helpful when we experienced issues and all the very nice coffee breaks.

Gothenburg July 2015

Adam Johansson and Johan Fredberg

NOMENCLATURE

Abbreviations

CDPM2	Concrete Damage Plasticity Model 2
CSCM	Continuous Surface Cap Model
DIF	Dynamic Increase Factor
FE	Finite Element
FP	Fracture Process
FPZ	Fracture Process Zone
FZ	Fracture Zone
SDOF	Single Degree Of Freedom

Roman upper case letters

A	Amplitude, Area
DIF_{ft}	Dynamic increase factor for tensile strength
$DIF_{l_{micro}}$	Dynamic increase factor for the combined length of microcracks
E	Kinetic Energy, Young's Modulus
F	Force
F_{appl}	Applied force
F_e	Equivalent force
F_l	Projected Force
G	Shear modulus
G_f	Fracture energy
H_p	Strain hardening
I	Impulse, Moment of Inertia
K	Stiffness
K'	Stiffness in elastoplastic range
N	Axial force
N_{cr}	Cracking force for concrete
N_u	Yield force for concrete
M	Moment
P	Point load
R	Resisting force
R_{cr}	Resting force when entering elastoplastic region
R_y	Resisting yield force
T_0	Period
V	Shear force
W	Work

Roman lower case letters

a	Acceleration
b	Width
c	Damping coefficient
d	Damage parameter
f	Frequency
f_y	Yield strength
f_u	Ultimate strength
f_{pu}	Ultimate strength
$f_{p0,1}$	Characteristic 0,1% proof-stress
f_t	Tensile strength of concrete
h	Height
k	Stiffness
k_b	Stiffness of beam
k_e	Equivalent stiffness
l	Length
l_{FZ}	Width of the fracture zone
l_{macro}	Length of the macro crack
l_{micro}	Length of the micro cracks
m	Mass
m_b	Mass of beam
m_e	Equivalent mass
p	Momentum
q	Distributed load
t	Time
u	Displacement
u''	Curvature
u_s	Displacement of system point
u_{cr}	Displacement when entering elastoplastic region
u_{pre}	Initial displacement due to prestressing
$\dot{u}_s$	Velocity of in system point
$\ddot{u}_s$	Acceleration in system point
v	Velocity
x	Coordinate
$\dot{x}$	Velocity
$\ddot{x}$	Acceleration

Greek letters

α	Phase angle, agitation
β	Shape factor
γ	Shear angle
ε	Strain
$\varepsilon_{p0,1}$	Characteristic 0,1% proof-strain
ε_{pl}	Plastic strain
ε_{pu}	Ultimate strain
ε_{tot}	Total strain
κ	History variable
κ^{elpl}	Transformation of the elastoplastic region
κ_F	Transformation factor for force
κ_k	Transformation factor for stiffness
κ_m	Transformation factor for mass
σ	Stress
$\dot{\sigma}$	Stress rate
σ_{appl}	Applied stress
σ_c	Concrete stress
σ_{cc}	Concrete Compressive stress
σ_{ct}	Concrete tensile stress
σ_{nom}	Nominal stress
σ_y	Yeild stress
τ	Shear Stress
υ	Poisson's Ratio
φ	Angle
ω	Angle frequency
ω_{max}	Maximum eigenfrequency, damage parameter

1 Introduction

1.1 Background

In today's society there are numerous of prestressed concrete structures such as nuclear power plants, protective shelters, railway sleepers and bridges that might be subjected to severe impact loadings both intentionally or unintentionally. How the structural response during impact loading is affected when prestressing is introduced into the structure is not very well studied. It is desirable to extend the knowledge within this area and hence it also becomes relevant to develop effective numerical analysis methods capable of simulating the impact following the structural response. This is of interest within the field since it would not only save time and money spent on experimental research but it also gives the opportunity to accurately study the structural response at any desired time step.

1.2 Aim and objectives

The aim of this study was to provide a good modeling technique for modeling of prestressed concrete structures subjected to dynamic loads in the FE-software LS-DYNA. This model was then used to give a better understanding of the effect of prestressing in dynamically loaded concrete beams. The work has been divided into objectives used to move the project forward, those are to:

- Based on informed choices with regard to available FE-modeling techniques in LS-DYNA develop a FE-model of a prestressed concrete beam which is successively verified in order to ensure a good performance.
- Evaluate four concrete material models that are implemented into the LS-DYNA software with regard to their performance during impact loading. Considered models are CDPM2-Bilinear, CDPM2-Linear, CSCM and Winfrith.
- With the help of the created FE-model examine what effect prestressing has on dynamically loaded concrete beams.

1.3 Methodology

A literature study was performed in order to obtain necessary knowledge and a fundamental understanding of the factors involved with dynamic loading. The study was focused on principles behind dynamics, different material responses, damage formulations and dynamic response of concrete. This knowledge created a foundation, which upon better decisions could be made when creating the FE-models regarding choice of element type, material models etc. In order to meet the stated objectives three "Beam Cases" were created and used during the work. The work itself can be sub-divided into four different stages to make the whole procedure more comprehensible.

Stage I – Creation and verification of Beam Case I
A real life experiment where a falling drop-weight hits a reinforced concrete beam was recreated in LS-DYNA and called "Beam Case I". The FE-model was statically verified using hand calculations according to Eurocode and the dynamic performance of the model was evaluated by comparisons to

the experimental test results. As an additional mean of verification the impact was also analyzed by the use of a SDOF-system.

Stage II – Choice of a suitable concrete material model
The statically- and dynamically verified FE-model of Beam Case I was used to run simulations with the concrete material models CDPM2-Bilinear, CDPM2-Linear, CSCM and Winfrith. Some comparison parameters were defined and each material model was evaluated with regard to their performance when subjected to impact loads. The most suitable material model according to the evaluation procedure was chosen to be used in all further analyses.

Stage III – Creation and verification of Beam Case II- and III
Beam Case II is a reinforced- and prestressed beam while Beam Case III is a regular reinforced beam. Those beams use the same geometries and are equivalent to each other with regard to their ultimate capacities. This equivalency was desirable in order to evaluate the effect of prestressing when the beams were subjected to identical loads. In this stage a possible alternative to model post-tensioned concrete beams in LS-DYNA was developed. The model was statically verified by hand calculations according to Eurocode.

Stage IV – Simulation of Beam Case II- and III subjected to dynamic loads
Beam Case II and Beam Case III were subjected to dynamic loads with the purpose of evaluating the prestressing effect during dynamic loading.

1.4 Limitations

All analyses in this work are limited to a test set-up consisting of a simply supported beam subjected to a static load or a falling drop weight hit the middle of the span of the beam. Only short term responses are considered and extracted results are limited to cracking loads, ultimate capacity loads, midspan deflections and crack patterns. Gravity loads are omitted in both the static and dynamic load case. Further, the evaluated concrete material models are CDPM2-Bilinear, CDPM2-Linear, CSCM and Winfrith.

1.5 Outline of thesis

Chapters 2 to 5 works as an introductory part where relevant theory is introduced to provide an understanding of the physics behind dynamically loaded concrete structures. The remainder of the thesis is then focused on the working procedure.

Chapter 2 explain basic definitions in dynamics and the theory behind it.

Chapter 3 describes material responses and damage formulations that are of relevance for the work.

Chapter 4 deals with concrete theory and the fundamental behaviour of plain concrete, reinforced concrete and prestressed concrete. The latter part of this chapter focuses on the dynamic response of concrete, and especially the theory behind strain rate effects.

Chapter 5 describes the principles behind a single degree of freedom system (SDOF-system). I.e. how a beam can be transformed into a mass-spring system describing the motion of a system point moving in one specified direction.

Chapter 6 addresses FE-modeling techniques. The concrete material models CDPM2-Bilinear, CDPM-Linear, CSCM and Winfrith are introduced in this chapter and the theory behind them are explained. Further, ways of modeling reinforcement, choice of element types, hourglass theory and contact surfaces are discussed.

Chapter 7 introduces a real life drop-weight experiment performed on a reinforced concrete beam. This experiment is referred to as "Beam Case I"

Chapter 8 explains how Beam Case I, presented in chapter 7, is recreated in LS-DYNA. The FE-model is verified statically as well as dynamically.

Chapter 9 treats the evaluation of the concrete material models. The evaluation takes into consideration how well the material models perform during both static and dynamic loading. Moreover, parameters such as mesh convergence ability, computational efficiency, sensitivity towards hourglass calibration and ease of use are examined.

Chapter 10 introduces Beam Case II and Beam Case III which is a reinforced- and prestressed concrete beam and a regular reinforced concrete beam. Those are equivalent to each other with regard to their ultimate capacities which is of importance since their structural responses will be compared during impact loading.

Chapter 11 explains how Beam Case II and Beam Case III, presented in chapter 10, are modeled in LS-DYNA. The verified modeling techniques, used in chapter 8 to model reinforced concrete beams, are now supplemented by modeling of a prestressing effect. The created FE-model of a prestressed concrete beam is statically verified with hand calculations according to Eurocode.

Chapter 12 presents results obtained from simulations on Beam Case II and Beam Case III when subjected to dynamic loads. The presented data is used as basis upon which the effect of prestressing is evaluated.

Chapter 13 summarizes the most important aspects of the performed work in the thesis. This includes discussions regarding the evaluated concrete material models, FE-modeling of concrete structures in LS-DYNA and the influence of prestressing on dynamically loaded concrete structures.

Chapter 14 List of references used in the report.

2 Basic Theory of dynamics

The following chapter will act as an introduction to dynamics and explain the basics concepts behind it. The chapter is based upon a similar chapter in Räddningsverket (2005).

2.1 Velocity and acceleration

Velocity, v, is defined as the time it takes to travel a certain distance. A particle that is travelling from point x_0 to x_1 over the time t_1 has a mean velocity which is then found by dividing the distance travelled by the time it took:

$$v = \frac{x_1 - x_0}{t_1 - t_0} \tag{2.1.1}$$

This can be expressed as the time-derivative of the distance:

$$v = \frac{dx}{dt} = \dot{x} \tag{2.1.2}$$

Acceleration, a, is the rate of change of the velocity i.e. the time it takes to reach a different velocity, as illustrated in Figure 2.1.1. If there is an increase in velocity this is called acceleration, while a decrease is called retardation.

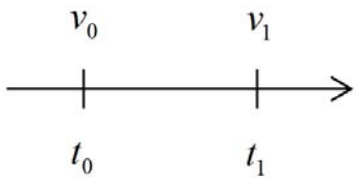

Figure 2.1.1: *Change in velocity over time.*

The mean change in velocity over time can be expressed as:

$$a = \frac{v_1 - v_0}{t_1 - t_0} \tag{2.1.3}$$

Which is defined in Equation (2.1.4) as the time-derivative of velocity or the second time-derivative of displacement:

$$a = \frac{d^2x}{dt^2} = \ddot{x} \tag{2.1.4}$$

2.2 Work and kinetic energy

When an object is stationary all forces acting upon it are in equilibrium. If this is disturbed by an external force it will start to move. A force, F, can be defined as the ability to accelerate an object, and can by Newton's second law of motion be expressed as:

$$F = m\ddot{x} \tag{2.2.1}$$

When a force acts upon a particle and moves the distance, l, as can be seen in Figure 2.2.1, a work, W, is performed. This is defined as:

$$W = Fl\cos(\varphi) = F_l l \tag{2.2.2}$$

where φ is the angle between the direction of the force and the direction of motion. F_l is the projection of the force along the direction of motion.

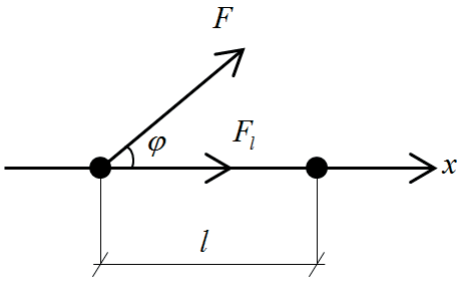

Figure 2.2.1: *Work performed by a force acting upon a particle.*

In dynamics the force is often variable and therefore it is better to express the work as an integral where the force is a function of x:

$$W = \int_0^l F_l(x)dx \tag{2.2.3}$$

Objects with mass, m, that are in motion have a kinetic energy, E, which is defined as:

$$E = \frac{m\dot{x}^2}{2} \tag{2.2.4}$$

In Figure 2.2.2 the particle subjected to a force in the direction of motion is seen. If $v_1 \neq v_0$, there will be a change in kinetic energy which is equal to the work performed by the force:

$$\frac{m\dot{x}_1^2}{2} - \frac{m\dot{x}_0^2}{2} = F_l l \tag{2.2.5}$$

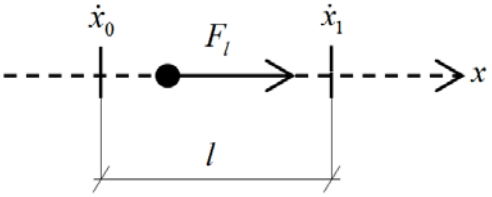

Figure 2.2.2: *Change in kinetic energy of a particle.*

2.3 Momentum and impulse

As mentioned in the previous section in a dynamic analysis the forces are often variable and varying in time, compared to static where the force is constant and the effects of time are considered as an equivalent static effect. Dynamic forces are therefore better expressed as an impulse acting on the particle. Any object in motion has a direction and momentum which is defined as:

$$p = m\dot{x} \tag{2.3.1}$$

where:

$p =$ momentum
$m =$ mass
$\dot{x} =$ velocity

The momentum can be changed by an impulse. By again taking the system in Figure 2.2.2 but this time investigating the momentum before and after a time dependant force is applied the following is obtained:

$$m\dot{x}_1 = m\dot{x}_0 + \int_{t_0}^{t_1} F(t)dt \tag{2.3.2}$$

The integral on the right hand side of Equation (2.3.2) is the impulse, I, acting on the particle:

$$I = \int_{t=0}^{t=t_1} F(t)dt \tag{2.3.3}$$

where $t = 0$ is moment of loading and $t = t_1$ is moment of unloading.

2.4 Free vibration

One example of a free vibration system is a mass connected to a spring with the stiffness, k, and length, l that is allowed to move freely in x-direction, can be seen in Figure 2.4.1. where the spring

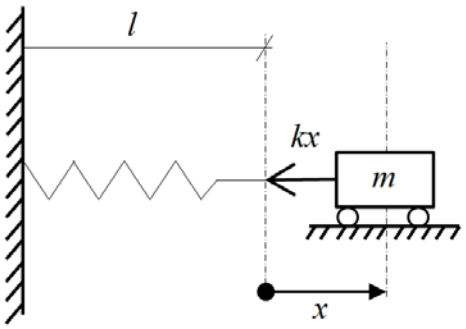

Figure 2.4.1: *Mass-spring system that is allowed to move in x-direction.*

is massless and follows Hooke's law, and by substituting F with Equation (2.2.1) the following is obtained:

$$F = -kx \tag{2.4.1}$$

$$m\ddot{x} = -kx \tag{2.4.2}$$

$$m\ddot{x} + kx = 0 \tag{2.4.3}$$

The solution to the system is found by dividing by m:

$$\ddot{x} + \frac{k}{m}x = 0 \tag{2.4.4}$$

where:

$$\frac{k}{m} = \omega^2 \Rightarrow \omega = \sqrt{\frac{k}{m}} \tag{2.4.5}$$

Here ω is the angular frequency and the solution to Equation (2.4.3) becomes:

$$x = A\sin(\omega t + \alpha) \tag{2.4.6}$$

The movement of the mass in Figure 2.4.1 is represented by a sine curve as can be seen in Figure 2.4.2, where A is the amplitude and α is the phase angle.

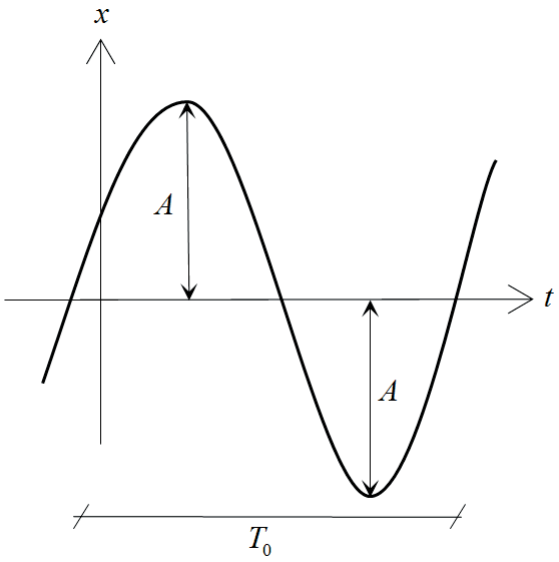

Figure 2.4.2: *Sine curve expressing the movement of the mass.*

T_0 in Figure 2.4.2 is the time it takes for the system to complete a full oscillation or period. The frequency, f, of the oscillation can then be calculated by Equation (2.4.7):

$$f = \frac{1}{T_0} \tag{2.4.7}$$

From the relationship between T_0, ω and f in Equation (2.4.8) it can be seen that the period and frequency depends on the mass and stiffness of the spring. The oscillations of the system seen in Figure 2.4.1 are undamped and referred to as harmonic.

$$T_0 = \frac{1}{f} = \frac{2\pi}{\omega} = 2\pi\sqrt{\frac{m}{k}} \tag{2.4.8}$$

2.5 Forced vibrations

If the mass is subjected to a time dependent force, $F(t)$, as shown in Figure 2.5.1 a forced vibration will occur.

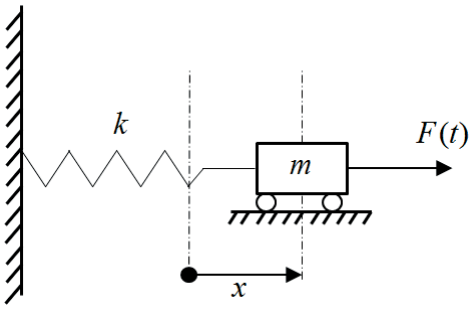

Figure 2.5.1: *Mass-spring system with external force.*

The system will then be expressed by a harmonic oscillation, see Section 2.4, and an agitation, φ, which is based upon the time history of the force. The agitation can also arise from offsetting the fixed end of the spring. The system can then be expressed as:

$$x = A\sin(\omega t + \alpha) + \varphi(t) \tag{2.5.1}$$

If the agitation is periodic and has a frequency close to the frequency of the oscillating system a phenomenon called resonance will occur. Which causes the motions in the system to magnify. If the agitation is expressed by Equation (2.5.2) the solution to the system is expressed as seen in Equation (2.5.3).

$$\varphi(t) = c\sin(\varepsilon t) \tag{2.5.2}$$

$$x = A\sin(\omega t + \alpha) + \frac{c}{1 - \frac{\varepsilon^2}{\omega^2}}\sin(\varepsilon t) \tag{2.5.3}$$

The motion of the system above and the system in Section 2.4 are both undamped, and therefore the system would be forever oscillating. But in reality there are always some type of damping in a system, for example friction, which causes the system to slow down an example of this can be seen in the next section.

2.6 Equation of Motion

The equation of motion is based upon the dynamic equilibrium of a system. In Figure 2.6.1 a mass suspended from a spring and a damper, the mass is subjected to gravity and an external force.

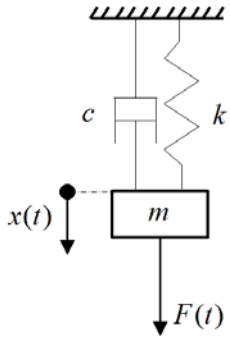

Figure 2.6.1: *Mass-spring system with a damper and an external force.*

By isolating the system as in Figure 2.6.2 if the corresponding forces are in equilibrium the sum of them is equal to zero.

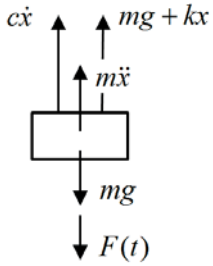

Figure 2.6.2: *Isolated system with corresponding forces.*

From this the equation of motion becomes:

$$F(t) + mg - (mg + kx) - c\dot{x} - m\ddot{x} = 0 \tag{2.6.1}$$

$$m\ddot{x} + c\dot{x} + kx = F(t) \tag{2.6.2}$$

where:

$m =$ mass
$k =$ stiffness of spring
$c =$ Damping coefficient

Which can be solved in several ways, one is the central difference method which is explained further in Section 2.7.

2.7 Central difference method

The equation of motion as seen in Equation (2.6.2), can be solved via Newmark-method, which is a direct integration solution scheme where the equation of motion is integrated in a step-by-step procedure. In a direct integration the equation do not require a transformation into an other form before the integration is performed. In the Newmark-method there are two parameters α and δ which determine the stability of the system. If these are set to $\alpha = 0$ and $\delta = 0.5$ it becomes conditionally stable. This means that there is a critical value for which the time step, Δt can not exceed or it will become unstable. If again the equation of motion for a single degree of freedom is used:

$$m\ddot{x} + c\dot{x} + kx = F(t) \tag{2.7.1}$$

According to Bathe (1996) the acceleration at the time t can then be expressed as:

$$\ddot{x}_t = \frac{1}{\Delta t^2}(x_{t-\Delta t} - 2x_t + x_{t+\Delta t}) \tag{2.7.2}$$

And the velocity as:

$$\dot{x}_t = \frac{1}{2\Delta t}(-x_{t-\Delta t} + x_{t+\Delta t}) \tag{2.7.3}$$

The first state for the equation is known, because of this it is an explicit method. By introducing Equation (2.7.2) and Equation (2.7.3) into the equation of motion, Equation (2.7.1), the following expression for the displacement at $t + \Delta t$ is found:

$$(\frac{1}{\Delta t^2}m + \frac{1}{2\Delta t}c)x_{t+\Delta t} = F(t) - k_t x_t + \frac{2}{\Delta t^2}mx_t - (\frac{1}{\Delta t^2}m - \frac{1}{2\Delta t}c)x_{t-\Delta t} \tag{2.7.4}$$

As can be seen in the equation above for the first iteration, $t = 0$, the displacement at $U_{0-\Delta t}$ is needed. This is expressed in the following manner based upon the displacement, velocity and acceleration at $t = 0$.

$$x_{0-\Delta t} = x_0 - \Delta t\dot{x}_0 + \frac{\Delta t^2}{2}\ddot{x}_0 \tag{2.7.5}$$

As mentioned previously a critical time step is needed to complete the algorithm, which is calculated as:

$$\Delta t_{cr} = \frac{2}{\omega_{max}} \tag{2.7.6}$$

Here ω_{max} is the maximum eigenfrequency, which depends on m and k. The stiffness of the system depends on the Young's Modulus and therefore varies depending on the material properties chosen. Which will be further explained in Chapter 3.

3 Material responses

In order to evaluate the response of a structure it is of great importance to define the behaviour of the involved materials. This thesis will treat three common material responses, namely linear elasticity, plasticity and elasto-plastic behaviour. Those material responses will be briefly described in this section since they are used to explain the behaviour of concrete in the beam analyses.

3.1 Linear elastic material

A linear elastic material behaviour is described by Hooke's Law:

$$\sigma = E\varepsilon$$

It states that the stress, σ, and the strain, ε, is linear proportional to each other via Young's modulus, E. Applied on a structural level the internal resisting force, R, of the structure is linear proportional to the displacement, u, in the same manner (Nyström 2006):

$$R = Ku$$

In Figure 3.1.1 those relations is graphically presented. It should be noted that, in linear elastic models, no permanent deformations remain after unloading of the material/structure.

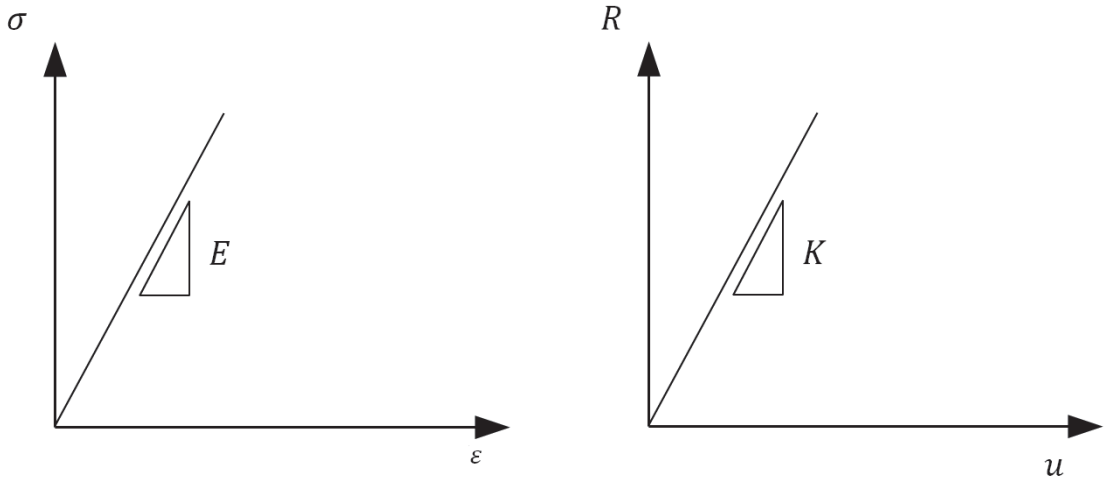

(a) *On a material level.* (b) *On a structural level.*

Figure 3.1.1: *Linear elastic material behaviour described by Hooke's law.*

3.2 Ideal plastic material

Characteristic for an ideal plastic material is that it does not undergo any deformations up to a certain stress level where, suddenly, deformations takes place without any further increase of the stress. This stress level is equal to the yield strength, σ_y, of the material. For a certain applied stress, $\sigma_{appl.}$, the material response can be described as follows (Nyström 2006):

$$\sigma = \sigma_{appl.} \quad \text{for} \quad \sigma_{appl.} < \sigma_y \quad \text{and} \quad u = 0$$

$$\sigma = \sigma_y \quad \text{for} \quad \sigma_{appl.} > \sigma_y \quad \text{and} \quad u > 0$$

As was the case for the linear elastic response also the plastic response can be described on a structural level:

$$R = P_{appl.} \quad \text{for} \quad P_{appl.} < R_y \quad \text{and} \quad u = 0$$

$$R = R_y \quad \text{for} \quad P_{appl.} > R_y \quad \text{and} \quad u > 0$$

In Figure 3.2.1 the responses are visualized graphically. In contrast to the linear elastic case the deformations obtained during plastic response becomes permanent.

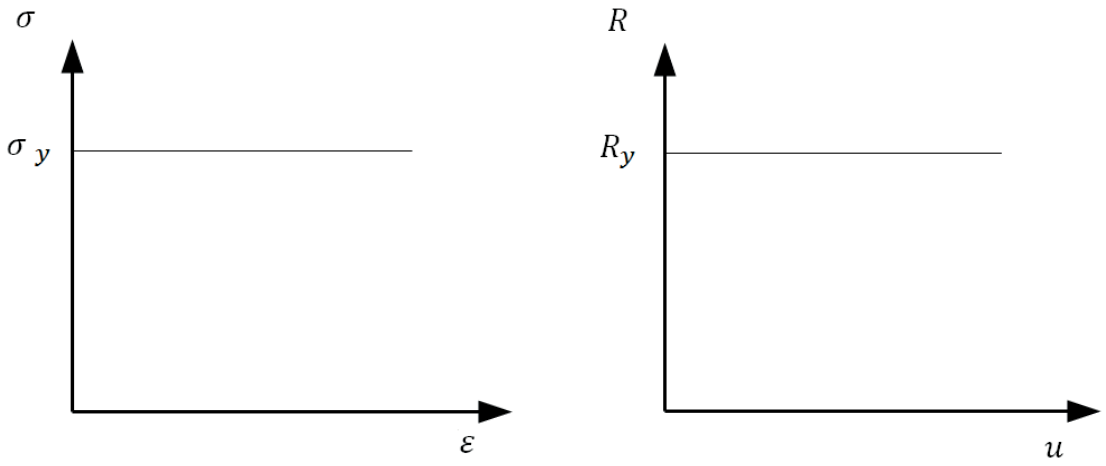

(a) *On a material level.* (b) *On a structural level.*

Figure 3.2.1: *Ideal plastic material response.*

3.3 Elastoplastic and trilinear materials

There is a wide array of materials that deform elastically up to a certain limit from which it then starts to deform plastically. This type of material response is called elastoplastic response and it is a combination of the linear- and plastic responses.

In order to describe a reinforced concrete beam in a satisfactory way a trilinear material response can be used (Nyström 2006). This behaviour can be seen in Figure 3.3.1 and it is a combination of a pure elastic part, an elastoplastic part and a pure plastic part.

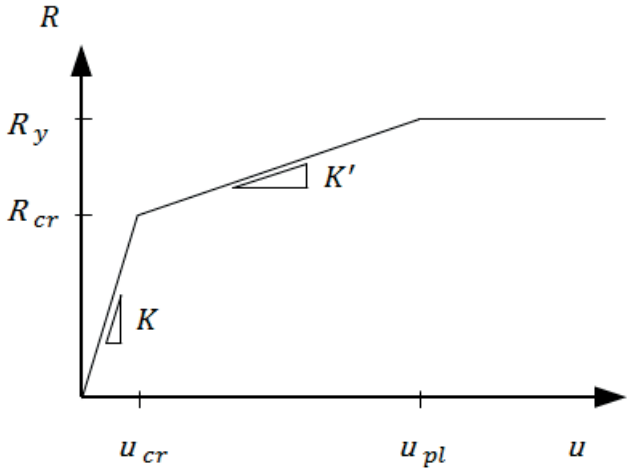

Figure 3.3.1: *Load-displacement curve for a trilinear material.*

The different parts of the curve (elastic, elastoplastic and plastic) corresponds to different states of the reinforced beam. Those would be uncracked, cracked and yielding of the reinforcement when a mechanism is formed. The first crack occurs when the internal force, R_{cr}, is reached which corresponds to a certain displacement, u_{cr}. Yielding of the reinforcement starts at R_y with a corresponding displacement of u_{pl}. Further, the stiffness of the beam changes from K during the uncracked state to K' during the cracked state and finally it becomes constant until a failure criterion is reached in the plastic state.
The trilinear material response presented in Figure 3.3.1 is formulated below (Nyström 2006):

$$R = Ku \quad \text{for} \quad P_{appl.} < R_c r$$

$$R = R_{cr} + K'(u - u_{cr}) \quad \text{for} \quad R_{cr} < P_{appl.} < R_y$$

$$R = R_y \quad \text{for} \quad P_{appl.} > R_m$$

3.4 Damage formulation during loading and unloading

A material that is subjected to a time dependant force can experience both a loading and an unloading phase. Depending on the type of material this behaviour is different. For a linear elastic material the unloading occurs along the same curve as the loading, same E, and both deformations and stress returns to zero, while for a plastic material the deformations are permanent. When the material is expressed by bi- or trilinear model the behaviour during unloading becomes more complex. In the following two sections two methods for expressing this behaviour will be explained.

3.4.1 Plasticity model

The plastic damage formulation has a plastic behaviour, where damage initiates when the ultimate capacity of the material is reached. The constitutive relationship is expressed as:

$$\sigma = E(\varepsilon_{tot} - \varepsilon_{pl}) \tag{3.4.1}$$

If the material is unloaded while still in the elastic region, ε_{pl} will be equal to zero and the system will return to its original state. Once the ultimate capacity has been reached plastic deformations occur and the material will return with the Young's modulus, E, to a new point of equilibrium, ε_{pl}. If the material is subjected to a load once again the process continues but from the new point of equilibrium which can be seen in Figure 3.4.1.

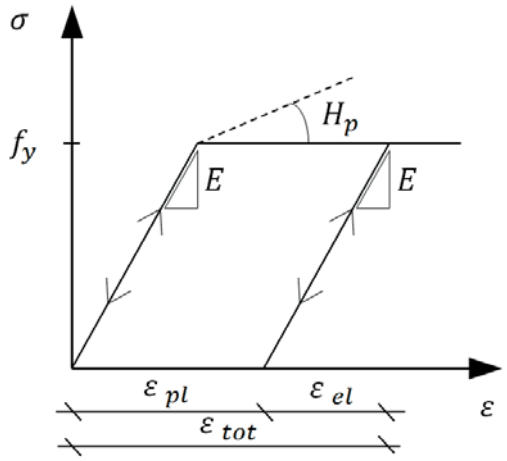

Figure 3.4.1: *Stress-strain relationship for a plasticity model. Arrows indicate loading/unloading.*

If there is strain hardening, H_p present in the material there will be a tangent modulus after the ultimate capacity of the material, $E \neq 0$ when $\sigma > f_y$. This gives the plasticity model extra capacity and therefore smaller plastic deformations.

3.4.2 Damage model

The damage model formulates the damage by continuously decreasing the Young's modulus of the material. If the material is loaded beyond its ultimate capacity and then unloaded the deformations will return to zero, as can be seen in Figure 3.4.2 it will return with a decreased Young's modulus.

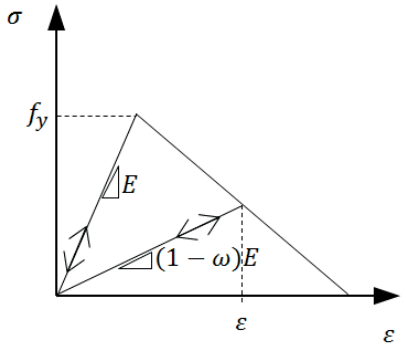

Figure 3.4.2: *Stress-strain relationship for damage model. Arrows indicate loading/unloading.*

The constitutive relationship is expressed as:

$$\sigma_{nom} = E\varepsilon(1-\omega) \quad \text{for} \quad 0 \leq \omega \leq 1 \tag{3.4.2}$$

where ω is the damage parameter, if $\omega = 0$ the material is undamaged and if $\omega = 1$ the material is fully damaged. ω is determined by inelastic strain that is accumulated in a history variable κ. The relationship between ω and κ is nonlinear, damage occurs faster in the beginning, even if the relationship between σ and ε is linear as can be seen in Figure 3.4.3. The constitutive relationship is also visible here, where the nominal stress is calculated by adding the damage parameter. In

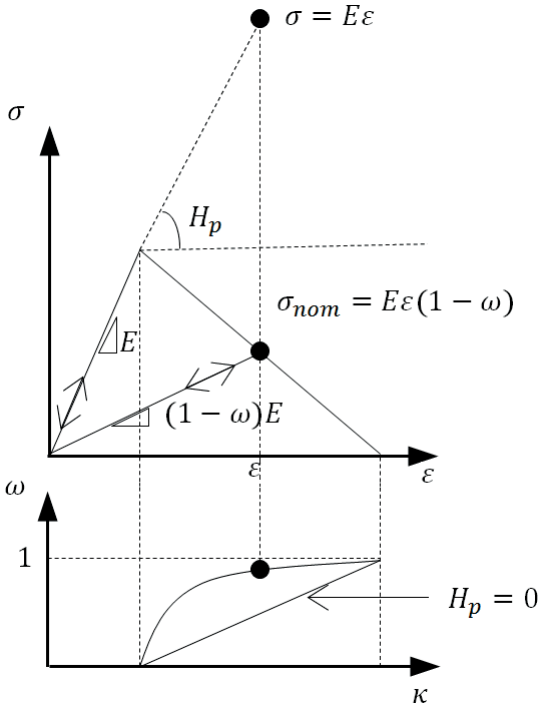

Figure 3.4.3: *The figure visualizes how the linear elastic stress σ are transformed into an nominal stress σ_{nom} by reduction of the Young's modulus. This size of the reduction depends on the damage parameter ω.*

Figure 3.4.3 the softening behaviour of the model can be seen, where stress decrease with increasing strain. This behaviour is favourable when simulating concrete materials. The damage model is as the plasticity model affected by strain hardening which is made clear in the bottom part of Figure 3.4.3.

4 Concrete Theory

Concrete is one of the most commonly used building material of today. Concrete complemented with reinforcement, stirrups, pre-stressing steel etc. gives the designer immense opportunities to control the appearance, structural behaviour, resistance and durability of a structure. In the following chapter some basic concepts will be explained.

4.1 Plain concrete

Concrete consists of aggregates, cement and water. However, on a structural level, the material can most often be regarded as homogenous. Its strength is affected by several factors where one of the more characteristic features is the materials capability to withstand high compressive forces but at the same time its incapability to manage tensile forces. This is demonstrated in Figure 4.1.1a where the principal stress-strain relationship for concrete can be seen. Figure 4.1.1b shows the load-displacement curve for a concrete member subjected to an axial tensile force, this figure can be compared with reinforced concrete in Figure 4.2.1a and prestressed concrete in Figure 4.3.1a. The two most undesirable properties of concrete regarding its resistance is the low tensile strength and the very brittle way in which it fails. Moreover, the concrete strength is highly affected by the

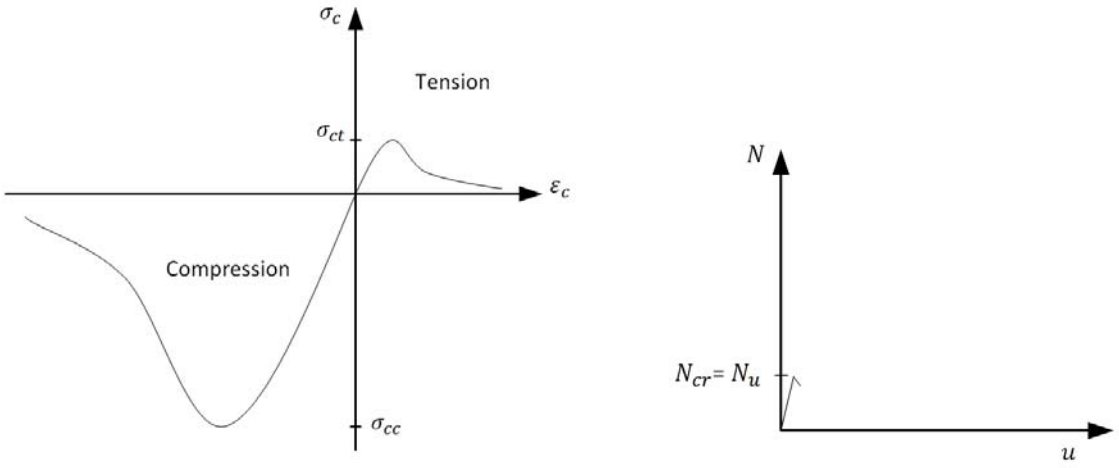

(a) *Stress-strain relationship for plain concrete.* (b) *Load-displacement curve for plain concrete.*

Figure 4.1.1: *Behaviour of plain concrete.*

applied loading state, i.e. to what combinations it is subjected to in bi- and tri-axial loading states. This behaviour is exemplified in Figure 4.1.2 for a bi-axial compressive test where $\sigma_1 = \sigma_2$. As the confining pressure is increasing so is its compressive strength. This is because σ_1 and σ_2 are restricting the shear dilation of the concrete. The increase in strength due to the surrounding pressure will be one of the parameters that increase the concrete ability to resist dynamic loads.

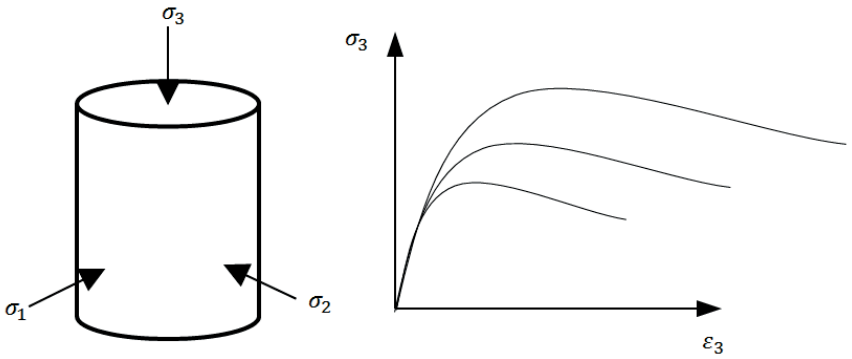

Figure 4.1.2: *Principal stress-strain relationship for a test cylinder with increasing confinement pressure where* $\sigma_1 = \sigma_2$*. The right figure shows the increase in compressive strength.*

4.2 Reinforced concrete

In order to maintain force equilibrium after cracking of the concrete, reinforcement is introduced in order to increase the load bearing capacity of the concrete. The reinforced concrete can be seen as a composite material where the reinforcement bar is anchored within the concrete and forces are transferred between the materials through bonding. Besides the reinforcement main task, to transfer tensile forces through cracked concrete zones, it also controls the crack widths as well as the distances between cracks. The composite action between concrete and reinforcing steel gives the designer opportunities to decide the stress field as well as the crack pattern of a structure that can be controlled by just adjusting the amount and distribution of reinforcement.

The principal stress-strain relationship for reinforcing steel along with a simplified and idealized stress-strain relationship according to Eurocode 2 is presented in Figure 4.2.1. Further, Figure 4.2.2 demonstrates the load-displacement curve for a reinforced concrete member subjected to an axial tensile force. This figure can be compared to the plain concrete in Figure 4.1.1b and prestressed concrete in Figure 4.3.1a.

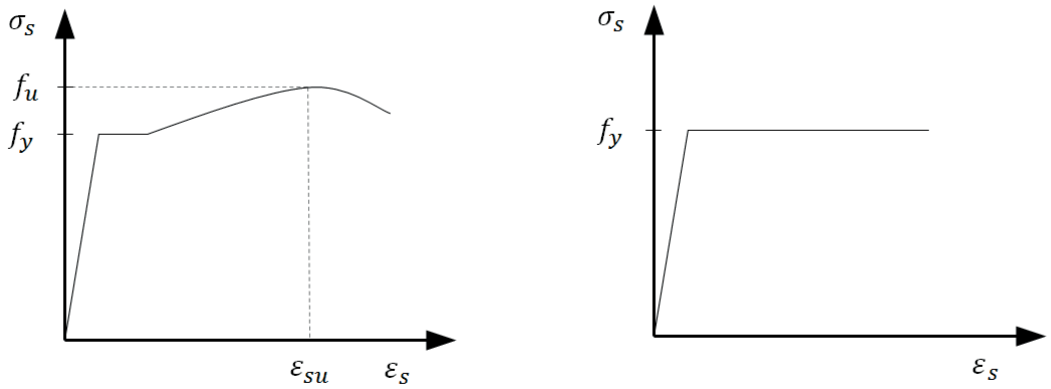

(a) *Principal stress-strain relationship for reinforcement.*

(b) *Idealized stress-strain relationship for reinforcement.*

Figure 4.2.1: *Response of reinforcement.*

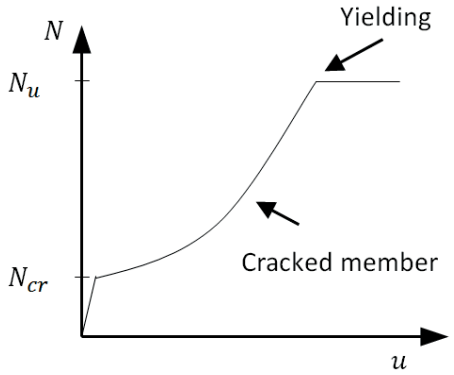

Figure 4.2.2: *Load-displacement curve for a reinforced concrete member subjected to an axial tensile force.*

4.3 Prestressed concrete

Pre-stressing is introduced into a structure so that the designer can get an even better crack control. This is beneficial when there is a need to maintain the rigidity of the uncracked structure, when there is a risk of corrosion of reinforcement due to open cracks, to prevent fatigue of the reinforcement or when there are high demands on the tightness of the structure. The main principle behind pre-stressing is to apply compressive forces to the structure. Then, in order for a crack to occur, the tensile stresses must first rise above the applied compressive stress before the member becomes tensioned. It is important to point out that the prestressing does not noticeably influence the flexural resistance of the member, but mainly delays the upcoming of cracks (Engström, 2011).

The principal stress-strain relationship as well as an idealized stress-strain relationship for pre-stressing steel (cold worked steel) can be seen in Figure 4.3.1. It should be noted that the strength of the prestressing steel is larger than the strength of ordinary reinforcement steel, but at the same time it lacks the ability to deform very much before failure. To clarify these property differences the working curve of regular reinforcement is also included in the figure.

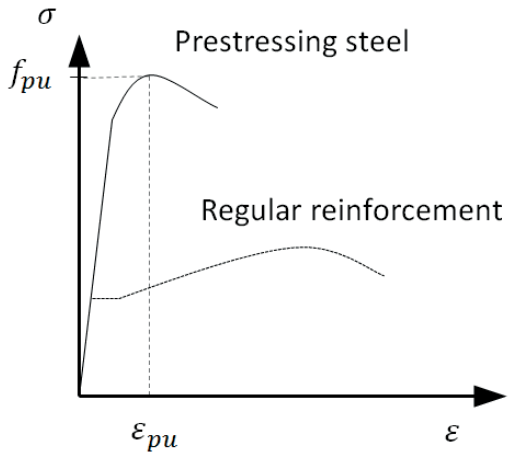

(a) *Principal stress-strain relationship for pre-stressing steel and regular reinforcement.*

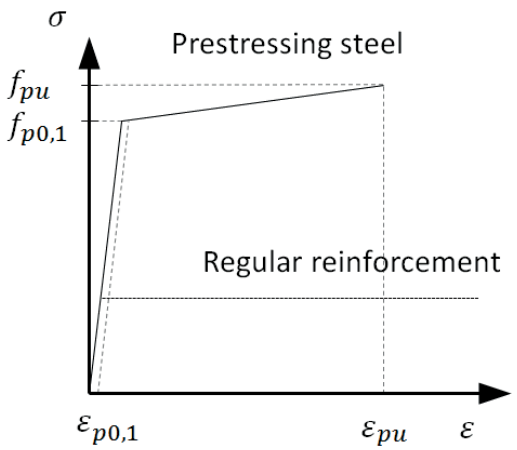

(b) *Idealized stress-strain relationship for pre-stressing steel and regular reinforcement.*

Figure 4.3.1: *Response of prestressing- and reinforcement steel.*

In Figure 4.3.2a the load-displacement curve is demonstrated for a prestressed member subjected to an axial tensile force. For comparison the same curve for the reinforced member is put into Figure 4.3.2b. As mentioned earlier the prestressing effect delays the cracking of the member but does not affect the ultimate tensile resistance.

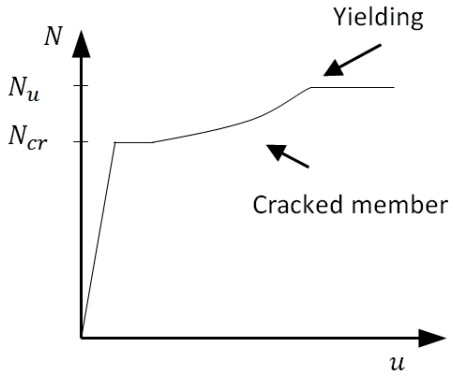

(a) *Load-displacement curve for a prestressed concrete member.*

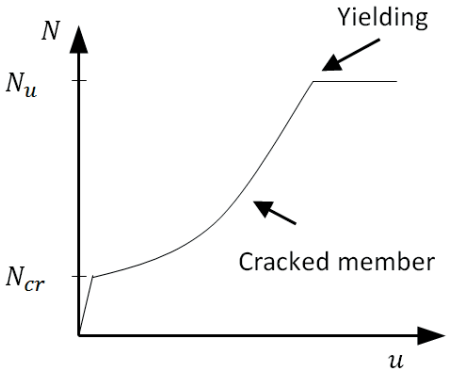

(b) *Load-displacement curve for a reinforced concrete member.*

Figure 4.3.2: *Load-displacement of prestressed- and reinforced concrete members subjected to an axial tensile force.*

Often when designing prestressed beam, the prestressing reinforcement is placed below the neutral layer, for simply supported beams, in order to get a positive moment acting upon the beam that will counteract he applied loads. The reinforcement can be placed at with a constant eccentricity, straight, or in a parabolic shape. An other results of this is a positive deflection will be present for an unloaded beam, an example of load-displacement curve for an eccentric prestressed beam can be seen in Figure 4.3.3, where u_{pre} is the initial displacement due to prestressing.

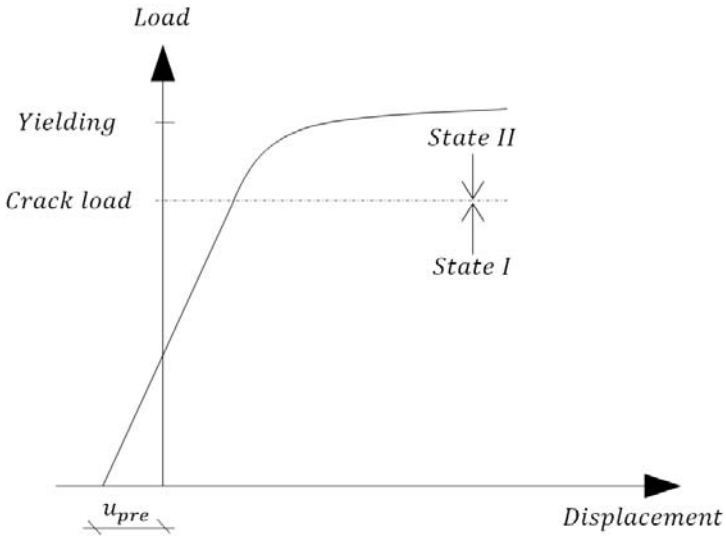

Figure 4.3.3: *Load-displacement curve for an eccentric prestressed beam.*

4.4 Concrete subjected to dynamic loading

The material response for plain concrete subjected to static loads is described in Section 4.1. However, when subjected to impact- or blast loads, concrete responds differently compared to when static loads are applied. A fast load application gives rise to strain rate effects, which in turn influences parameters such as concrete strength, Young's modulus and the concrete's ability to absorb energy, (Belaoura, 2010) and (Cusatis, 2010). In the following sections the concept of strain rate effects will be further explained.

4.4.1 Strain rate

Strain rate is defined as strain per unit of time s^{-1} and in Figure 4.4.1 the strain rate spectra is demonstrated along with different types of loads that is typical for certain strain rates. Materials

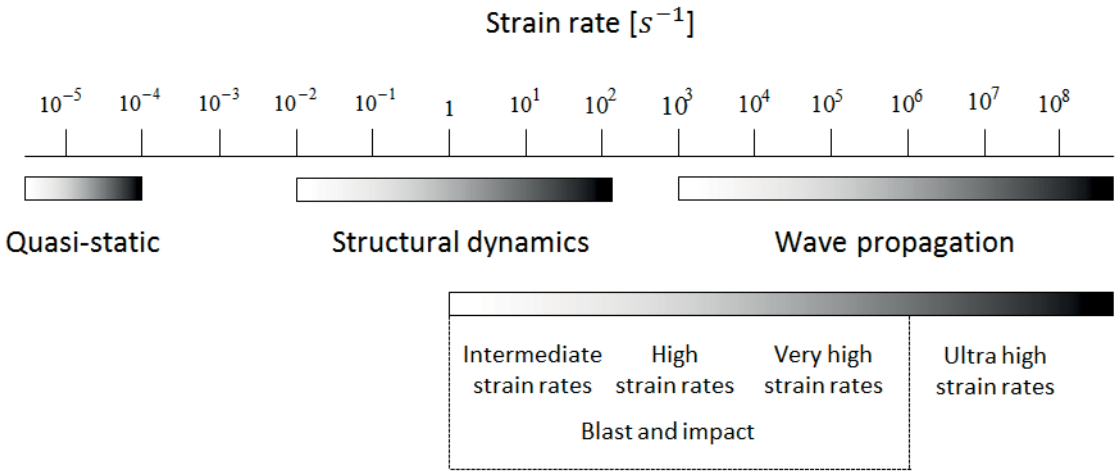

Figure 4.4.1: *Strain rates and corresponding problem areas, based on Nyström (2006).*

subjected to large strain rates most often show a change in behaviour compared to when they experience a static load case, as both the stiffness and the strength can increase significantly. The increased values of different parameters are presented with a Dynamic Increase Factor, or DIF, which is defined as the ratio between the dynamic and the static material property. DIF: s and their relations to the strain rates can be seen for the material strengths, Young's modulus and fracture energies in Figure 4.4.2, Figure 4.4.3 and Figure 4.4.4 respectively (Nyström, 2013). Although there are many factors influenced by high strain rates, only the most significant such as a forced crack path and inertia forces will be further discussed. (Räddningsverket, 2005), (Cusatis, 2010) and (Belaoura, 2010).

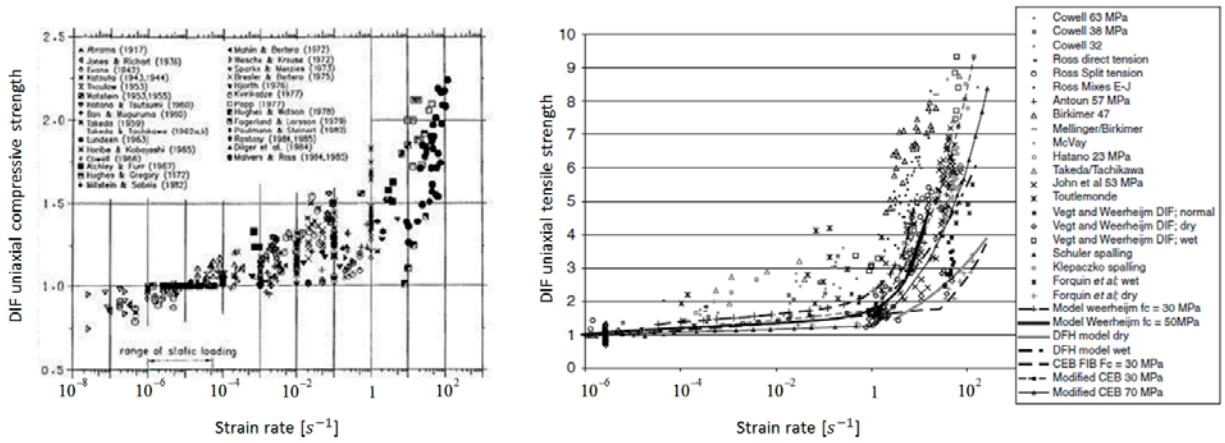

Figure 4.4.2: *Dynamic increase factors (DIF) for concrete subjected to a) uniaxial tension and b) uniaxial compression. Based on Weerheijm (2013) and Belaoura (2010).*

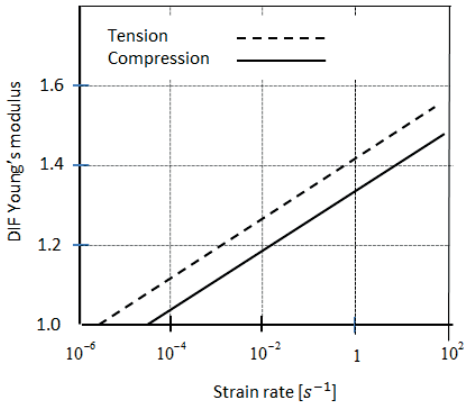

Figure 4.4.3: *Dynamic increase factor for Young's modulus, based on test data compiled by Nyström (2013).*

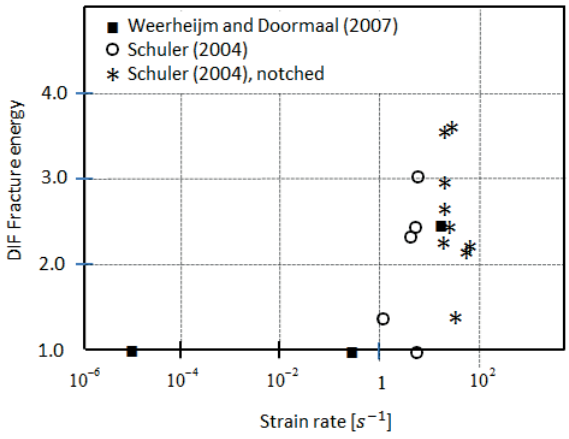

Figure 4.4.4: *Dynamic increase factor for the fracture energy, based on test data by Schuler (2004), Weerheijm and Doormaal (2007), compiled by Nyström (2013).*

4.4.2 Forced crack path due to fast loading rate

In a static case the cracks would propagate along the simplest way, through the cement paste. However, at high loading rates, the cracks must propagate fast through the concrete and hence they are forced to split through the stiffer aggregates. There is not enough time to propagate around the aggregates. Due to this effect the concrete strength as well as the stiffness of the concrete is increased (Räddningsverket, 2005). This is illustrated in Figure 4.4.5.

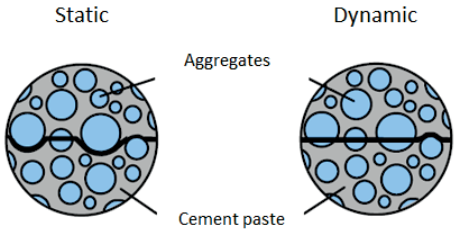

Figure 4.4.5: *Crack paths through concrete for a static load as well as for a dynamic load. (Räddningsverket, 2005)*

4.4.3 Inertia forces

When a structure is subjected to dynamic loads that give rise to high strain rates the material in the very near vicinity of the impact zone wants to expand in the direction transverse to the load direction. However, due to the high strain rates, the material is not given time to expand which results in a sort of confinement effect. The stressed concrete experiences a triaxial confinement effect similar to the static confinement described in Section 4.1, the principle is demonstrated in Figure 4.4.6. (Belaoura, 2010) and (Cusatis, 2010) . Inertia is also a main influence behind the greatly increased tensile strength that can be measured at high strain rates. In this case the material around the cracks tips is affected by inertia forces which lead to a reduced crack propagation rate within the fracture zone, see Figure 4.4.7 (Weerheijm, Van Doormaal, 2007).

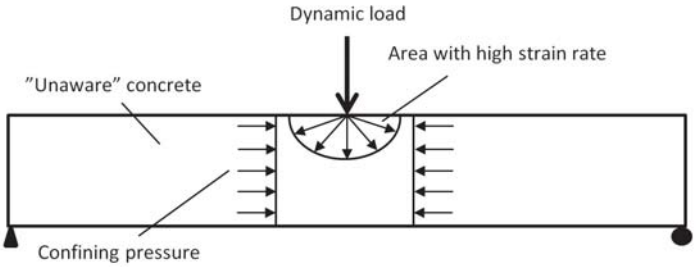

Figure 4.4.6: *Demonstration of the effect from inertia forces under compressive dynamic loading.*

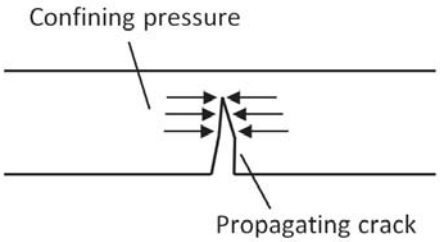

Figure 4.4.7: *Demonstration of the effect from inertia forces under tensile dynamic loading and crack propagation.*

Inertia forces have a significant impact on the concrete strength, especially when high strain rates occur (Belaoura, 2010) and (Cusatis, 2010). To demonstrate this influence a number of test performed by (Cusatis, 2010) is presented in Figure 4.4.8. The figures are slightly modified in order to remove unnecessary information. Reference is made to the strain rate spectra, presented in Figure 4.4.1, that gives an idea of the magnitudes of the strain rates used in the tests. Further, to point out the correlation between different tests made on the subject a comparison can be made between Figure 4.4.2 and the bottom figures in Figure 4.4.8. It should also be noted that the used strain rates has low- to moderate values. The influence due to inertia forces would be even greater for higher values.

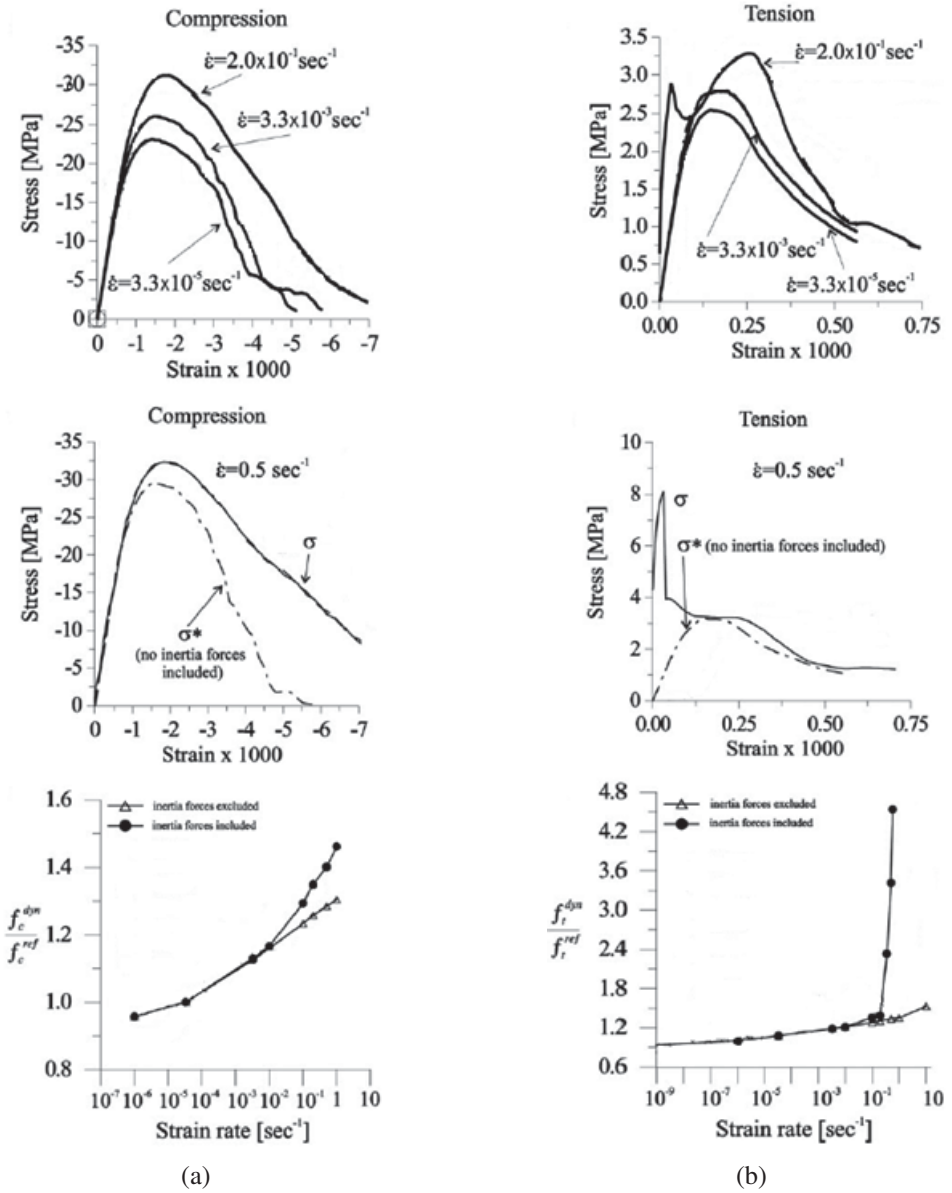

(a) (b)

Figure 4.4.8: ***Top figures:*** *Uniaxial compressive/tensile tests for different strain rates.* ***Middle figures:*** *Effect of inertia forces on compressive/tensile stress-strain curves for a certain strain rate.* ***Bottom figures:*** *Effect of inertia forces on compressive/tensile DIF.*

The top figures in Figure 4.4.8 shows the stress-strain relationship for different strain rates. Those curves indicate that higher strain rates results in an increased concrete strength. Then, to demonstrate the influence of inertia forces, tests are carried out for a certain strain both with- and without the inertia forces included. The peak stress as well as the post-peak behaviour is affected by the inertia forces, see the middle figures in Figure 4.4.8. Finally, the DIF is plotted in the bottom figures of Figure 4.4.8. As stated before higher strain rates results in higher DIF:s and again the effect of inertia forces can be seen in the figures. The figures indicate that the effect of inertia forces cannot be ignored even for relatively small strain rates. However, it should be mentioned that the literature is not entirely consistent regarding the influence of inertia forces. According to (Weerheijm and Forquin, 2013) the increased concrete strength for strain rates below $\dot{\varepsilon} = 2\frac{1}{s}$ is not due to inertia effects. The cause behind the strength increase in this low strain rate regime is assigned to the moisture content and pore structure of the concrete.

4.4.4 Fracture behaviour due to strain rate effects

This section is mainly based on observations made by (Weerheijm and Forquin, 2013) where an extensive assessment is made in order to quantify the strain rate influence on fracture behaviour. It is important to bear in mind that data and standardized models to examine the fracture behaviour are scarce, hence the presented results must be questioned further.

To describe the tensile failure response of concrete load-deformation curves are most commonly used, an example of which can be seen in Figure 4.4.9a. When the material strength f_t is reached damage will be initialized.Finally, before the strain rate effects are considered, a crucial parameter for the fracture process called fracture energy (G_f) is introduced. A small modification of the curve in Figure 4.4.9a is presented in Figure 4.4.9b. The load-deformation curve is turned into a stress-deformation curve and the fracture energy is defined as being the area under this particular curve. A high value of the fracture energy (a large area) means that the material can absorb more damage energy in the cracking phase and hence also mobilize a greater cracking resistance. The curve in Figure 4.4.9b can be further modified into a curve consisting of an elastic stress-strain part and a permanent stress-crack opening part, Figure 4.4.9c. In this case the fracture energy is defined as the area under the stress-crack opening part of the curve. Then, during the fracture process, damage energy is drawn into the fracture zone where it is absorbed in order to successively open the crack. The descending part of the curve can be divided into two parts representing different phases of the crack development; those would be microcracking and macrocracking as shown in Figure 4.4.10. At first microcracks starts to grow within a zone called the fracture process zone (FPZ). As the amount of microcracks gets larger they will start to connect to each other creating bigger macrocracks, which can also be referred to as the actual visible cracks. A distinction is made between the fracture process zone (FPZ) containing the microcracks and the fracture zone (FZ) consisting of both the FPZ and the material where the macrocrack occur, see Figure 4.4.10. This zone separation is made in order to later on be able to better explain the influence from strain rate effects on the fracture process. It should also be clarified that the concrete tensile resistance is completely depleted within the macrocracking zone (fully developed crack) whereas there is still resistance left in the microcracking zone, which is exemplified in Figure 4.4.10.

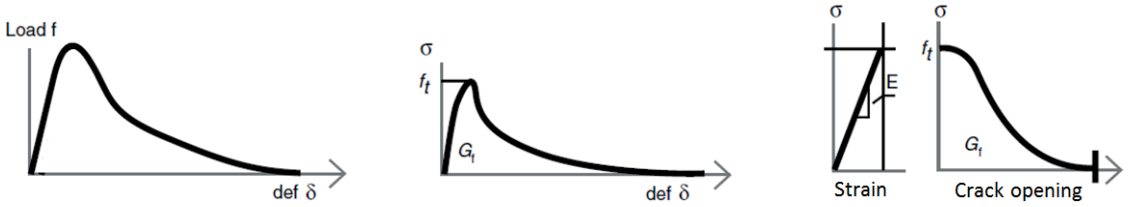

(a) *Load-deformation curve for concrete.*

(b) *Stress-deformation curve for concrete.*

(c) *Stress-crack opening curve for concrete.*

Figure 4.4.9: *Curves relating load application to deformation for concrete. Based on Weerheijm and Forquin (2013).*

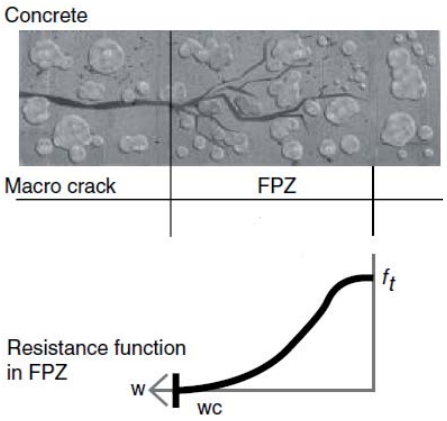

Figure 4.4.10: *Crack propagation consisting of fully developed macrocracks and partially opened microcracks. Within the FZP-zone there is still resistance against the cracks propagation. Weerheijm and Forquin (2013).*

The reasoning behind strain rate effects on the concrete fracture is again based on the curve in Figure 4.4.9a which is simplified in Figure 4.4.11. The descending part of the curve, describing softening of the concrete, is divided into two distinctive parts representing microcracking and macrocracking respectively.

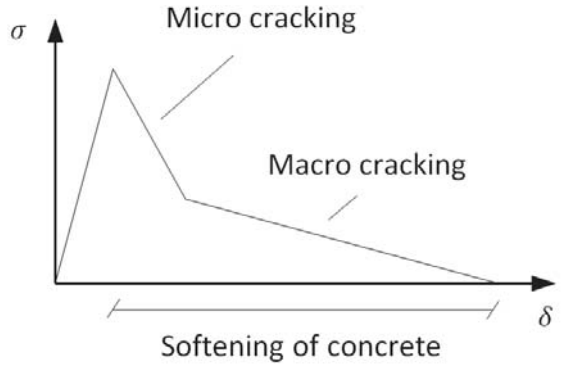

Figure 4.4.11: *Simplified stress-deformation curve for concrete. The descending part of the curve represents softening of the material and is defined by a steep branch where microcracking takes place and a flattening branch where the macrocrack is formed.*

The principle behind crack initializing and propagation is that damage starts to grow from defects within the material. When the load is increased so is the damage within a certain limited zone resulting in crack development. However, it is only the material in the very close vicinity to these initial defects that starts to develop into cracks. The material outside the affected zone is instead released from stress as the crack grows and absorbs the damage energy. This means that the crack is discretized within a relatively small FZ which is demonstrated in Figure 4.4.12a. An increased loading rate change this behaviour. If a fast load is applied the initial crack does not have time to absorb the damage energy fast enough. Zones that previously, in the static load case, experienced a stress release due to growth of the initial crack are now subjected to stresses which means that microcracks will start to grow from defects within these zones. So a dynamic load case results in more microcracking in the FZ and hence also the fracture energy is increased, see Figure 4.4.12b. An important remark to make along with this observation is that the dynamic increase factor for the fracture energy (DIF_{G_f}) cannot be directly correlated to the dynamic increase factor for the tensile strength (DIF_{ft}). This is due to the fact that higher strain rates are required to activate rate effects for the fracture energy than what is required to obtain rate effects on the tensile strength.

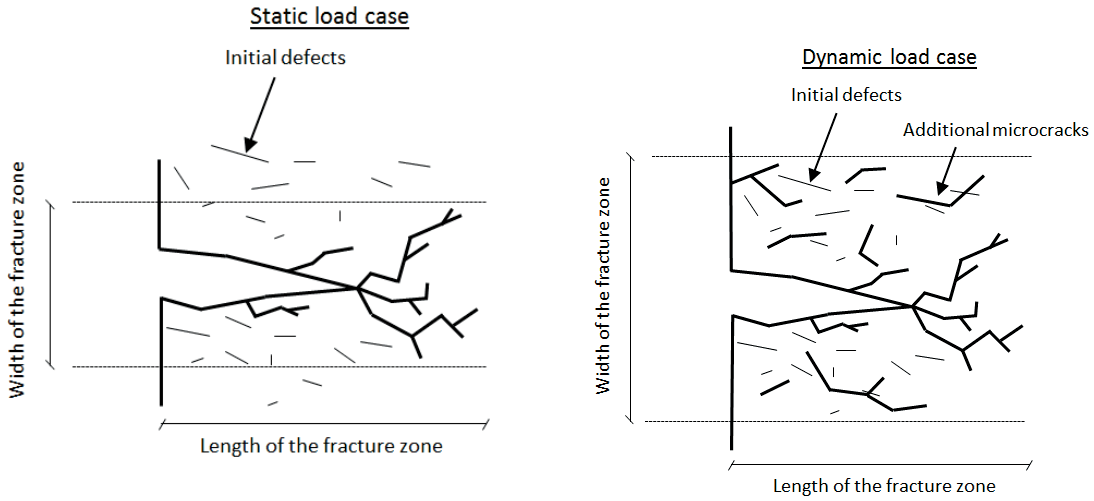

(a) *Crack response for a static load case.* (b) *Crack response for a dynamic load case.*

Figure 4.4.12: *For a static load case the crack propagation is slow, hence the material in the vicinity of the crack is given time to experience a stress release. However, for a dynamic load case, the crack cannot absorb the damage energy fast enough, which means that the surrounding material becomes stressed and cracks can be initialized.*

In order to quantify the impact from strain rate on the fracture energy some values are given in Table 4.4.1 and Table 4.4.2. Details regarding the concrete composition are left out since the purpose is to principally demonstrate the change in fracture energy.

Table 4.4.1: *Test data showing strength, fracture energy and DIF for different strain rates (Vegt et al. 2009)*

$\dot{\sigma}$ $[GPa/s]$	f_t $[MPa]$	G_f $[N/m]$	DIF_{ft} $[-]$	DIF_{G_f} $[-]$
10^{-4}	3.30	120.2	1.0	1.0
40	5.58	120.4	1.7	1.0
1700	10.47	679.0	3.2	5.6

Table 4.4.2: *Test data showing crack information for different strain rates (Vegt et al. 2009)*

$\dot{\sigma}$ $[GPa/s]$	l_{FZ} $[mm]$	l_{macro} $[mm]$	l_{micro} $[mm]$	$DIF_{l_{micro}}$ $[-]$
10^{-4}	6.1	80	141	1.0
40	8.1	86	94	0.7
1700	19.1	81	170	1.2

The parameters used in table 4.4.1 and table 4.4.2 are described below:

$\dot{\sigma}$ = Applied stress rate.

f_t = Tensile strength of concrete.

G_f = Fracture energy.

DIF_{ft} = Dynamic increase factor for the tensile strength.

$DIF_{l_{micro}}$ = Dynamic increase factor for the combined length of the microcracks. Showing the increased amount of microcracks in the FZ relative to the amount for a static load case.

l_{FZ} = Width of the fracture zone.

l_{macro} = Length of the macrocrack.

l_{micro} = Length of all the microcracks combined.

At a first view it might seem strange that the total combined length of the micro cracks for the intermediate loading rate in table 4.4.2 is lower than the corresponding value for the low loading rate. However, a reasonable explanation would be that the initialized micro cracks happens to make the macro crack grow in this particular test case. This theory is strengthened by the fact that the macro crack in fact is longer than what it is for the slow loading rate. On the contrary, for the very fast loading rate, the amount of micro cracks in the FPZ increases while the macro crack is almost unchanged compared to the slow loading rate. Figure 4.4.13 shows the stress-deformation curves for the tests presented in table 4.4.1 and table 4.4.2.

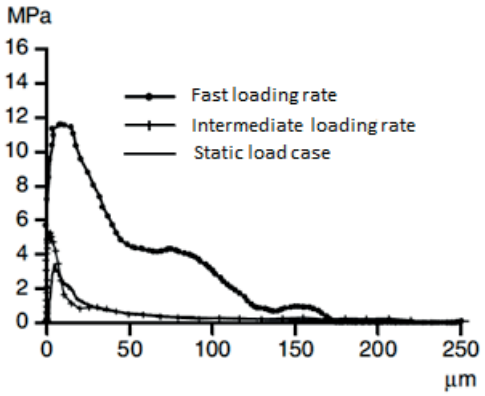

Figure 4.4.13: *Load-deformation curves for the different strain rates examined above.*

Based on the results presented in table 4.4.1 and table 4.4.2, the load-displacement curves in Figure 4.4.13 and the reasoning above regarding fracture energy. Some important conclusions can be drawn, at high strain rates the damage energy is absorbed within a larger zone resulting in increased microcracking and a wider FZ. It worth noting that the length of the macrocracks is almost unchanged while the microcracks become longer. As mentioned before it is important that the strain rate dependency of the fracture energy DIF_{G_f} (see Figure 4.4.4) is not quantified directly based on the DIF_{ft} (see Figure 4.4.2) since the parameters becomes rate dependent at different strain rates. Finally, the strain rate dependency for fracture energy in a uniaxial tensile test is visualized in Figure 4.4.14.

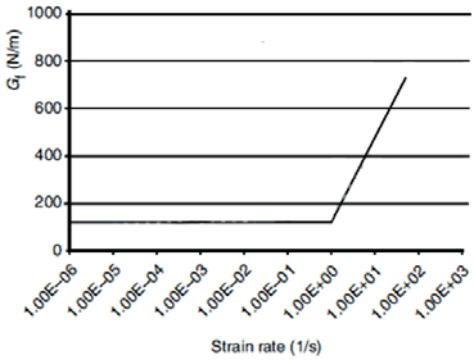

Figure 4.4.14: *Relation between strain rate and corresponding fracture energy. Based on Weerheijm and Forquin (2013.*

4.4.5 Wave propagation

As can be seen in Figure 4.4.1 the strain rate spectra cover a wide array of strain rates. The lowest rates is considered in long term material responses while the highest rates arises during impact loading where extreme impact velocities has to be considered. One of the most characteristic features related to dynamic loading is the increased material strength due to inertia forces, see Section 4.4.3. This feature becomes notable at intermediate strain rates and is then increasingly important as the strain rates become higher. At very high strain rates, such as for an extreme velocity impact, waves in combination with high triaxial pressure (inertia forces) triggers failure mechanisms such as “cratering” and “spalling” with radial cracking around the projectile tunnel, see Figure 4.4.15a (Riedel and Forquin, 2013). Figure 4.4.15b indicates the presence of a "ring" of concrete that is in tensions. This is called hoop stresses and these become more distinctive as the loading rates increases. The principle behind them is shown in Figure 4.4.16

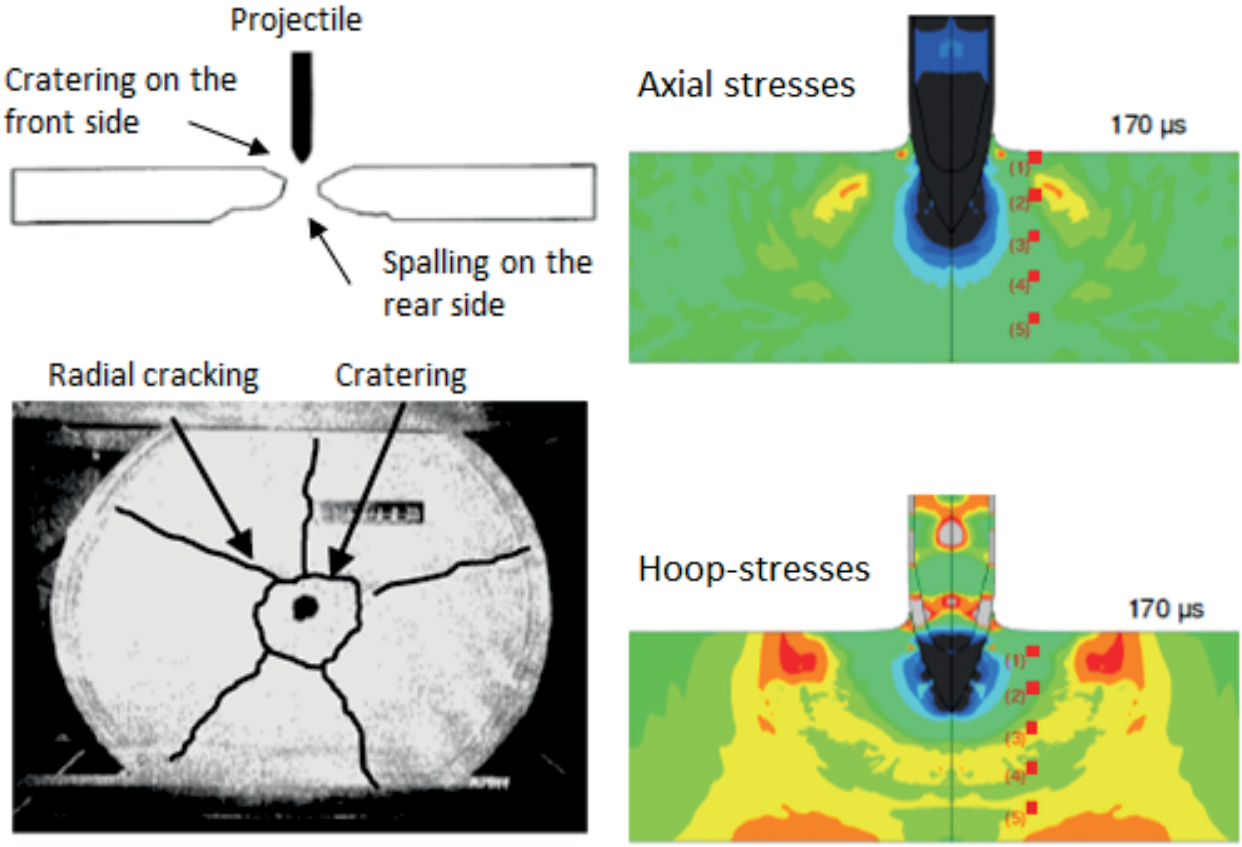

(a) *A high velocity projectile hitting a concrete wall.*

(b) *FEM-visualization of a high velocity projectile hitting a concrete wall.*

Figure 4.4.15: *a) Possible damage modes when a concrete wall is hit by a high velocity projectile. b) A FEM-visualization of a high velocity projectile hitting a concrete wall. In the bottom figure a ring of concrete in tension is visible. Both figures from Riedel and Forquin (2013).*

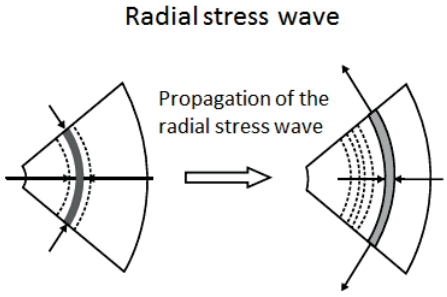

Figure 4.4.16: *Left figure: Directly after impact a radial stress wave is formed consisting of triaxial compressive stresses. Right figure: The stress wave propagates and the triaxial compressive state changes into compressive radial stresses and tensile tangential stresses. Riedel and Forquin (2013).*

The wave propagation effect is described in (Nyström, 2013). When a structure is subjected to a load there are always waves that propagate through the material in order to carry the "load information" to all parts of the structure. Those waves are carried through the material at a speed of about 3500 m/s which means, that for a quasi-static load case, the load information will reach all the parts of the structure basically at the same time as the load is applied so that the entire structure will react to the load and deform uniformly. See Figure 4.4.17a. For dynamic loads it becomes successively more important to consider the wave propagations within the material as the strain rates increases. The reason behind this is that the waves may not be able to reach all parts of the structure before areas close to the load application starts to deform, hence giving a structural response that differs from the quasi-static response. For strain rates approximately above $10^4 \frac{1}{s}$ the impact may be so violent that almost all deformation takes place in the very close vicinity to the load application area before any waves have reached other parts of the structure. Those high velocity impacts causes very localized damage and the analysis is now mainly concerning wave propagation rather than structural behaviour. See Figure 4.4.17b. Notice that the beam does not deform globally, but all deformation is concentrated to the area close to where the impact occurs.

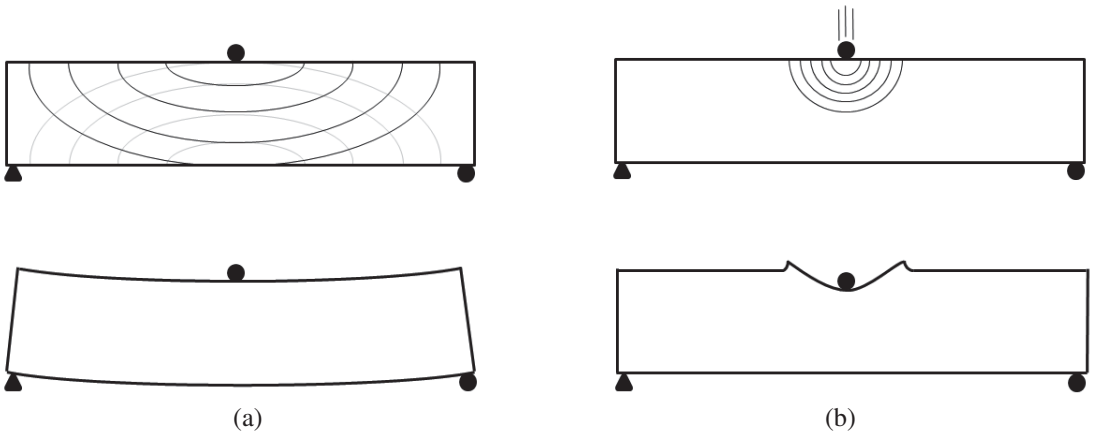

Figure 4.4.17: *Wave propagation and corresponding structural response for a) quasi-static loading case and b) high velocity loading case (causing high strain rates). Based on Nyström (2013).*

5 Beam tranformation SDOF

A deformable beam has an infinite amount of degrees of freedom, which can lead to heavy calculations. In practice when designing concrete beams it is common to only investigate the motions in one direction. Because of this and to reduce the amount of calculations needed it is advantageous to transform the beam into an equivalent mass-spring system as seen in Figure 5.1 where this single degree of freedom describes the displacements in a so called system point. This point can be placed anywhere on the beam according to Johansson and Laine (2012), however in this report it will be placed where the maximum displacement occurs.

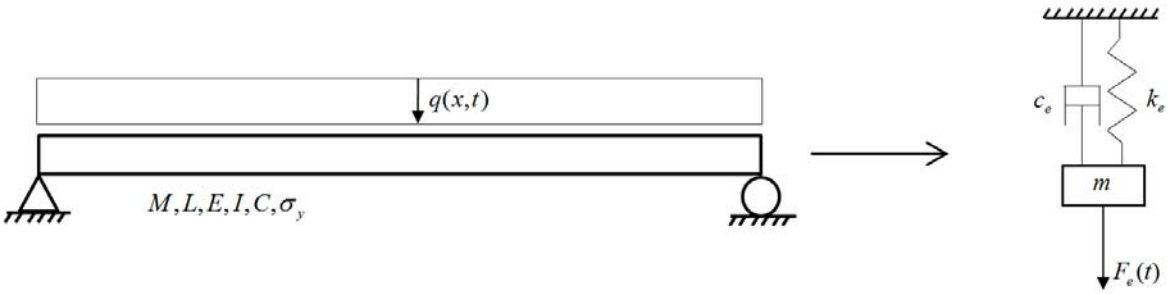

Figure 5.1: *A beam transformed into a single degree of freedom system.*

This is a simplification and therefore not entirely representative of the reality. Since only the displacement in one point is calculated, the rest of the beam is assumed to have a deflection shape that is defined by the user. In this report the deflection corresponding to the first mode shape is used see Figure 5.2, which depends on the boundary conditions and location of loading.

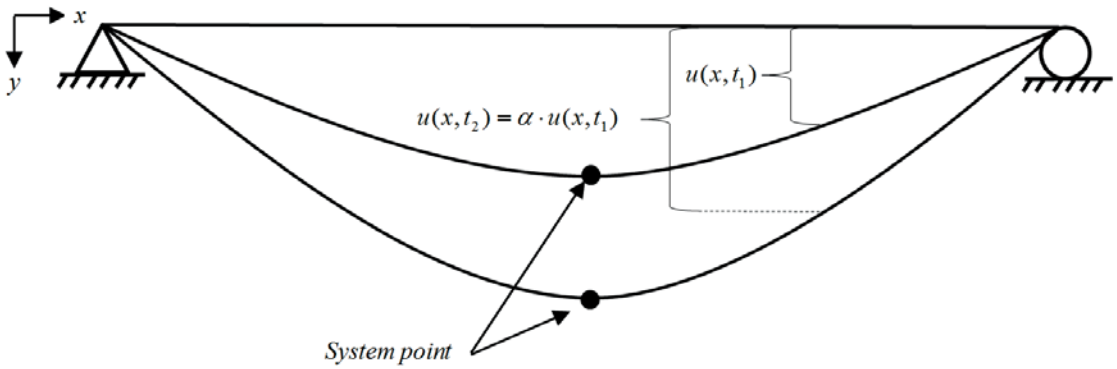

Figure 5.2: *The deformation shape at t_1 and t_2*

For the SDOF-system to be a representation of the beam, the mass, stiffness and damping has to give the same response in the system point as the whole beam. To make sure it is equivalent the energy in the system needs to be conserved. As only heavy impact loads will be investigated, damping can be neglected since load durations are so short that the damping will be of little importance to the maximum deflection according to Johansson and Laine (2012).

The equation of motion of the equivalent SDOF system can be seen in Equation (5.1.2). Here the transformation factors,κ, are also introduced.

$$m_e\ddot{u} + k_e u = F_e(t) \tag{5.0.1}$$
$$m_e = \kappa_m m_b \tag{5.0.2}$$
$$k_e = \kappa_k k_b \tag{5.0.3}$$
$$F_e(t) = \kappa_F F(t) \tag{5.0.4}$$

The transformation factors will be further explained in the following sections

5.1 Transformation factor for the mass

Obtain the equivalent mass, m_e, of the system a transformation factor that is based on the fact that the response of the system point in both systems should generate the same kinetic energy. For the SDOF-system the kinetic energy is defined as:

$$E_k^{SDOF} = \frac{m_e \dot{u_s}^2}{2} \tag{5.1.1}$$

Where $\dot{x_s} = \frac{\Delta u_s}{\Delta t}$ is the velocity at the system point in vertical direction. The kinetic energy of the beam is calculated in every position as:

$$E_k^{Beam} = \int_{x=0}^{x=L} \frac{m_b'(x)\dot{u}(x)^2}{2} dx \tag{5.1.2}$$

Here $\dot{u}(x) = \frac{\Delta u(x)}{\Delta t}$ and as mentioned before the energy is the same in the systems which leads to:

$$E_k^{SDOF} = E_k^{Beam} \tag{5.1.3}$$

$$\frac{m_e \dot{u_s}^2}{2} = \int_{x=0}^{x=L} \frac{m_b'(x)\dot{u}(x)^2}{2} dx \tag{5.1.4}$$

$$m_e u_s^2 = \int_{x=0}^{x=L} m_b'(x) u(x)^2 dx \tag{5.1.5}$$

By combining the last step with Equation (5.0.2) the following is found:

$$\kappa_m = \int_{x=0}^{x=L} \frac{m_b'(x)u(x)^2}{m_b u_s^2} dx \tag{5.1.6}$$

By assuming that mass is constant over the length of the beam,$m_b'(x) = m_b'$, the total mass of the beam can then be written as:

$$m_b = m_b' L \tag{5.1.7}$$

Then combining Equation (5.1.6) and Equation (5.1.7) the following expression for κ_m is found:

$$\kappa_m = \frac{1}{L} \int_{x=0}^{x=L} \frac{u(x)^2}{u_s^2} dx \tag{5.1.8}$$

So as can be seen the transformation factor for mass is dependant assumed shape of deflection.

5.2 Transformation factor for the force

The equivalent external force, F_e, needs to conserve the external work performed by the actual forces acting upon the beam.

$$W_e^{SDOF} = F_e u_s \tag{5.2.1}$$

$$W_e^{Beam} = \int_{x=0}^{x=L} q(x)u(x)dx \tag{5.2.2}$$

As before the work performed needs to be equal, and combining the work with Equation (5.0.4) the following is obtained:

$$\kappa_F = \int_{x=0}^{x=L} \frac{q(x)u(x)}{F(t)^{Beam}u_s}dx \tag{5.2.3}$$

Where:

$$F(t)^{Beam} = \int_{x=0}^{x=L} q(x)dx \tag{5.2.4}$$

For cases when where the load is constant over the length of the beam, $q(x) = q$ it is found that:

$$F(t)^{Beam} = qL \tag{5.2.5}$$

Which by combining with Equation (5.2.3) the expression can be simplified as:

$$\kappa_F = \frac{1}{L}\int_{x=0}^{x=L} \frac{u(x)}{u_s}dx \tag{5.2.6}$$

As well as for the mass the force is dependant on the assumed deflection shape.

5.3 Transformation factor for the stiffness

For the stiffness of the system the internal force needs to be equivalent in both systems. The internal force is different depending on the behaviour of the material used. The variation between the different behaviours can be seen in Figure 5.3.1. Where the area under the graphs represents the internal work.

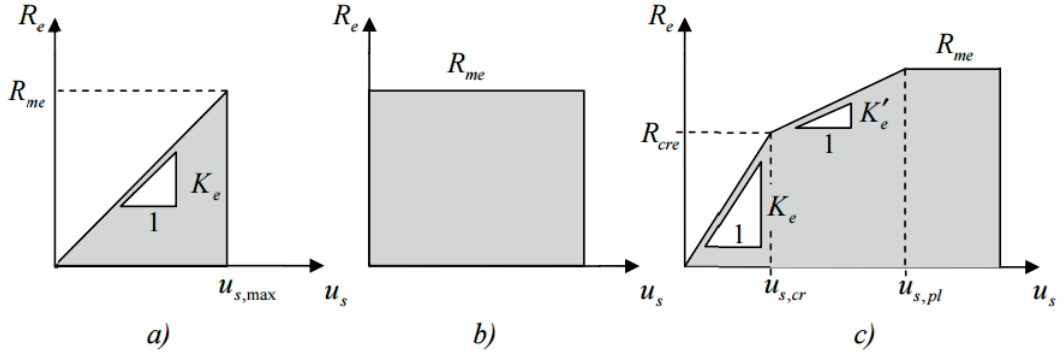

Figure 5.3.1: *I for different material behaviours a) Linear elastic b) Ideal plastic c) Trilinear material. The area underneath the graph is the internal work (Johansson and Laine, 2012)*

For the different behaviours the internal for is expressed as follows.

Linear elastic behaviour:

$$R_e = k_e u_s \tag{5.3.1}$$

Ideal plastic behaviour:

$$R_e = R_{me} \quad \text{for} \quad u_s(t) \neq 0 \tag{5.3.2}$$

Trilinear behaviour:

$$R_e = \begin{cases} k_e u_s & \text{for } u_s \leq u_{s,cr} \\ k_e u_{s,cr} + k'_e(u_s - u_{s,cr}) & \text{for } u_{s,cr} \leq u_s \leq u_{s_{pl}} \\ R_{me} & \text{for } u_{s,pl} < u_s \end{cases} \tag{5.3.3}$$

5.3.1 κ_k for a linear elastic material

The work performed by the deformations in a beam can be found by looking at a infinitesimal segment of the beam, the forces acting upon it and the corresponding deformations, see figure Figure 5.3.2

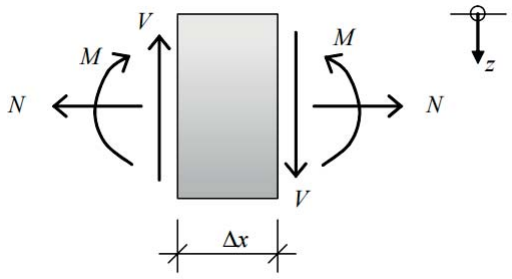

Figure 5.3.2: *An infinitesimal segment of a beam, and forces.*

Looking at the constitutive relationship between the forces, **N** and corresponding deformations $\Delta\mathbf{n}$ are:

$$\mathbf{N} = \frac{1}{\Delta x}\begin{bmatrix} EA & 0 & 0 \\ 0 & \frac{GA}{\beta} & 0 \\ 0 & 0 & EI \end{bmatrix} \Delta\mathbf{n}, \mathbf{N} = \begin{bmatrix} N \\ V \\ M \end{bmatrix}, \Delta\mathbf{n} = \begin{bmatrix} \Delta n \\ \Delta t \\ \Delta m \end{bmatrix} \tag{5.3.4}$$

Where:

$$\begin{aligned} E &- \text{Young's modulus} \\ A &- \text{Area of cross section} \\ G = \frac{E}{2(1+\nu)} &- \text{Shear modulus} \\ \nu &- \text{Poisson's Ratio} \\ \beta &- \text{Shape factor, constant} \\ I &- \text{Moment of intertia} \end{aligned}$$

The deformations, $\Delta\mathbf{n}$, are defined as can be seen in Figure 5.3.3

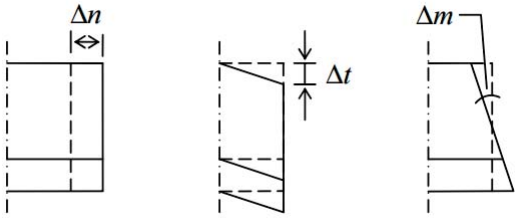

Figure 5.3.3: *Deformations of the beam segment.*

The work performed by the deformations in the beam due to shear force should be equal to the work performed by the deformations due to shear stress which is the basis of the derivation for the shape factor, β.

$$V\overline{\gamma} = V\frac{V\beta}{GA} = \int_{z=0}^{z=h} \tau(z)\gamma(z)b(z)dz \tag{5.3.5}$$

Where:

$$\overline{\gamma} = \frac{V\beta}{GA} \quad - \quad \text{average value of shear angle}$$
$$\tau \quad - \quad \text{Shear stress}$$
$$b \quad - \quad \text{Width}$$
$$h \quad - \quad \text{Height}$$
$$\gamma = \frac{\tau}{G} \quad - \quad \text{Shear angle}$$

After a small amount of time and loading the sectional forces will have changed from $\mathbf{N}$ to $\mathbf{N}+d\mathbf{N}$ and thereby the deformations will have changed by $\Delta\mathbf{n}+d\Delta\mathbf{n}$. The change of the work is then defined as the change of the work performed by the change of deformation.

$$dW_i^s = Nd\Delta n + Vd\Delta t + Md\Delta m \tag{5.3.6}$$

Where s is the index of the segment, by applying Hooke's Law to Equation (5.4.1) the following is found:

$$dW_i^s = \frac{EA}{\Delta x}\Delta n d\Delta n + \frac{GA}{\beta\Delta x}\Delta t d\Delta t + \frac{EI}{\Delta x}\Delta m d\Delta m = \mathbf{N}^t d\Delta\mathbf{n} \tag{5.3.7}$$

To get the total work of deformation it needs to be integrated over the total deformation of the segment, $\Delta\mathbf{n}$.

$$W_i^s = \int_{\Delta n=0}^{\Delta n} \frac{EA}{\Delta x}\Delta n d\Delta n + \int_{\Delta t=0}^{\Delta t} \frac{GA}{\beta\Delta x}\Delta t d\Delta t + \int_{\Delta m=0}^{\Delta m} \frac{EI}{\Delta x}\Delta m d\Delta m = \tag{5.3.8}$$

$$= (EA(\Delta n)^2 + \frac{GA}{\beta}(\Delta t)^2 + EI(\Delta m)^2)\frac{1}{2\Delta x} \tag{5.3.9}$$

Again to find the total work performed by the deformations in the beam the Hooke's law is used and integrating the work performed by the segment over the total length of the beam, L, the total work is expressed as:

$$W_i^{beam} = \int_{x=0}^{x=L} \frac{W_i^s}{\Delta x} dx = \int_{x=0}^{x=L} (\frac{N^2}{EA} + \frac{\beta V^2}{GA} + M(x))u''(x))\frac{1}{2} dx \tag{5.3.10}$$

Where $u''(x)$ is the curvature of the beam. Now that the work performed by the beam has been defined the SDOF system needs to be investigated. A SDOF system subjected to a load, F_e, and a corresponding displacement, ξ, that results in an internal work which with the help of equation Equation (5.3.1) can be expressed as:

$$W_i^{SDOF} = \int_{\xi=0}^{\xi=u} R_e d\xi = \int_{\xi=0}^{\xi=u} k_e \xi d\xi = \frac{k_e u_s^2}{2} = \kappa_k \frac{k_b u_s^2}{2} \tag{5.3.11}$$

As stated before the internal work for the two systems needs to be equal, $W_i^{SDOF} = W_i^{Beam}$, and therefore the following expression is found:

$$\kappa_k \frac{k_b u_s^2}{2} = \frac{1}{2} \int_{x=0}^{x=L} (\frac{N^2}{EA} + \frac{\beta V^2}{GA} + M(x)u''(x))dx \tag{5.3.12}$$

The stiffness of the beam, k_b, depends on the spacial shape of the beam and is determined by:

$$\int_{x=0}^{x=L} q(x,t)dx = k_b u_s \tag{5.3.13}$$

By combining Equation (5.3.13) and Equation (5.3.12) the expression for the transformation factor is found to be:

$$\kappa_k = \frac{1}{u_s} \frac{\int_{x=0}^{x=L} (\frac{N^2}{EA} + \frac{\beta V^2}{GA} + M(x)u''(x))dx}{\int_{x=0}^{x=L} q(x,t)dx} \tag{5.3.14}$$

In the case of beams where the length is more than ten times the height of the beam($L = 10h$) the effects of shear can be neglected, i.e for high beam it needs to be considered (Nyström, 2006). The normal force is needed when analysing a prestressed beam but for reinforced beam without a normal force it can be neglected.

5.3.2 κ_k for a ideal plastic material

Again taking a segment of the beam as in Figure 5.3.2 and again applying a load and use the change in deformation to obtain the work performed by this change. The transformation factor is then found analogously as with the linear elastic beam to be:

$$W_i^{beam} = \int_{x=0}^{x=L} (\frac{N^2}{EA} + \frac{\beta V^2}{GA} + M(x)u''(x))\frac{1}{2}dx \tag{5.3.15}$$

The internal work for the SDOF can also be derived in a similar fashion to the linear elastic case, with a displacement ξ, but in the case of a ideal plastic material the reaction force is constant.

$$W_i^{SDOF} = \int_{\xi=0}^{\xi=u} R_e d\xi = R_{me} u_s = \kappa_k R_m u_s \tag{5.3.16}$$

As mentioned in Section 5.3 the total internal work for both the beam and SDOF should be the same, Which leads to the following equation:

$$\kappa_k R_m u_s = \int_{x=0}^{x=L} (\frac{N^2}{EA} + \frac{\beta V^2}{GA} + M(x)u''(x))\frac{1}{2}dx \tag{5.3.17}$$

$$\kappa_k = \frac{1}{R_m u} \int_{x=0}^{x=L} (\frac{N^2}{EA} + \frac{\beta V^2}{GA} + M(x)u''(x))\frac{1}{2}dx \tag{5.3.18}$$

The external force is equal to the maximum value of the reaction force:

$$R_m = \int_{x=0}^{x=L} q(x,t)dx \tag{5.3.19}$$

From this the final expression for the transformation factor can be found, here once again the shear can be neglected for beams shorter than($L = 10h$) and the normal force is not necessary in reinforced beams without a normal force, but needs to be taken into consideration for pre-stressed beams.

$$\kappa_k = \frac{1}{u_s} \frac{\int_{x=0}^{x=L} (\frac{N^2}{EA} + \frac{\beta V^2}{GA} + M(x)u''(x)) \frac{1}{2} dx}{\int_{x=0}^{x=L} q(x,t)dx} \tag{5.3.20}$$

5.3.3 κ^{elpl} for trilinear material

To a trilinear material the previous two transformation factors can be used for their respective region. For the elasoplastic region however the derivation for the factors can become rather complex (Nyström, 2006) and therefore in this report it is assumed that the elastoplatic transformation factors are and average between the linear elastic and ideal plastic factor.

$$\kappa^{elpl} = \frac{\kappa^{el} + \kappa^{pl}}{2} \tag{5.3.21}$$

5.4 SDOF of a prestressed beam

For a prestressed beam the transformations factors κ_m and κ_F but for the stiffness, κ_k , will be influenced by the presence of the normal force that is an effect of the prestressing. It was found that the expression for κ_k when taking into account the normal force became very complex and difficult to work with and therefore it was not used. Bellow the derivation of the expression can be found.
The total work of the beam can be written as:

$$W_i^{beam} = \int_{x=0}^{x=L} \frac{W_i^s}{\Delta x} dx = \int_{x=0}^{x=L} (\frac{N^2}{EA} + \frac{\beta V^2}{GA} + M(x)u''(x)) \frac{1}{2} dx \tag{5.4.1}$$

The shear force, V in Equation (5.4.1) is neglected and therefore can be simplified as:

$$W_i^{beam} = \int_{x=0}^{x=L} (\frac{N^2}{EA} + M(x)u''(x)) \frac{1}{2} dx \tag{5.4.2}$$

The internal work of the SDOF-system can be expressed as:

$$W_i^{SDOF} = \int_{\xi=0}^{\xi=u} R_e d\xi = \int_{\xi=0}^{\xi=u} k_e \xi d\xi = \frac{k_e u_s^2}{2} = \kappa_k \frac{k_b u_s^2}{2} \tag{5.4.3}$$

Equation (5.4.1) and Equation (5.4.3) needs to be equal, from that the following is found:

$$\kappa_k \frac{k_b u^2}{2} = \frac{1}{2} \int_{x=0}^{x=L} (\frac{N^2}{EA} + M(x)u''(x)) dx \tag{5.4.4}$$

The expression can be simplified further by:

$$k_b u = \int_{x=0}^{x=L} q(x,t)dx \tag{5.4.5}$$

By substituting Equation (5.4.5) into Equation (5.4.4) κ_k can be expressed in the following manner::

$$\kappa_k = \frac{1}{u}\frac{\int_{x=0}^{x=L}(\frac{N^2}{EA} + M(x)u''(x))dx}{\int_{x=0}^{x=L} q(x,t)dx} \tag{5.4.6}$$

Below a simplification of Equation (5.4.6) for a simply supported beam subjected to a point load in the midspan can be found. Firstly:

$$P = \int_{x=0}^{x=L} q(x,t)dx \tag{5.4.7}$$

$$u = u(x = \frac{L}{2}) = \frac{PL^3}{48EI} \tag{5.4.8}$$

From Equation (5.4.8) the pointload P can be expressed as:

$$P = \frac{48EI}{L^3}u \tag{5.4.9}$$

Equation (5.4.7) substituted into Equation (5.4.6) yields the following::

$$\kappa_k = \frac{1}{uP}\int_{x=0}^{x=L}(\frac{N^2}{EA} + M(x)u''(x))dx \tag{5.4.10}$$

In an additional step Equation (5.4.7) can be substituted into Equation (5.4.10) and the integral is multiplied with the two terms inside the brackets:

$$\kappa_k = \frac{L^3}{u^2 48EI}(\int_{x=0}^{x=L}(\frac{N^2}{EA})dx + \int_{x=0}^{x=L} M(x)u''(x)dx) \tag{5.4.11}$$

The outermost expression in Equation (5.4.11) is multiplied into the brackets in order to completely separate the integrals from each other. The integration point are now changed to only include half the length of the beam. Because of this in the following expression the curvature, u'', and moment, $M(x)$, at midspan can be substituted into the expression. If the equation is still to be valid after the change in integration points it needs to be multiplied with a factor 2.

$$\kappa_k = \frac{2L^3}{u^2 48EI}\int_{x=0}^{x=\frac{L}{2}}(\frac{N^2}{EA})dx + \frac{2L^3}{u^2 48EI}\int_{x=0}^{x=\frac{L}{2}} M(x)u''(x)dx \tag{5.4.12}$$

Curvature, u'', can be expressed as:

$$u''(x) = \frac{M(x)}{EI} \tag{5.4.13}$$

And the variation in moment along half the length of the beam:

$$M(x) = \frac{Px}{2} \tag{5.4.14}$$

Equation (5.4.14) is substituted into Equation (5.4.13) which in turn is substituted into Equation (5.4.15). From this the following is found:

$$\kappa_k = \frac{2L^3}{u^2 48EI}\int_{x=0}^{x=\frac{L}{2}}(\frac{N^2}{EA})dx + \frac{2L^3}{u^2 48EI^2}\int_{x=0}^{x=\frac{L}{2}}(\frac{Px}{2})^2 dx \tag{5.4.15}$$

If P in the second part of the equation is substituted according to Equation (5.4.7) and the integration is calculated, that part will be equal to 1 further seen in Nyström2006 equation A.15. Integration of the part that includes the normal force yields:

$$\frac{2L^3N^2}{48EIu^2EA}\int_{x=0}^{x=\frac{L}{2}} 1dx = \frac{L^3N^2}{24EIu^2EA}[x]_0^{\frac{L}{2}} \tag{5.4.16}$$

Finishing the calculation yields:

$$\frac{L^4N^2}{48EIu^2EA} \tag{5.4.17}$$

The transformation factor, κ_k for stiffness of a simply supported prestressed beam subjected to a point load in the midspan therefore is:

$$\kappa_k = 1 + \frac{L^4N^2}{48EIu^2EA} \tag{5.4.18}$$

As can be seen from Equation (5.4.18), κ_k when a normal force is present becomes dependant on the deflection squared u^2. This becomes impossible to work with since at the start when $u = 0$ the expression becomes invalid, and if it the deflection is close to 0 the stiffness will approach infinity. Because of this the transformations factors for a reinforced beam were used in the prestressed case.

6 FE-Modeling techniques

The numerical analyses were performed using the finite element software LS-DYNA. In the following chapter different concrete material models in LS-DYNA will be explained together with two different ways to model reinforcement and a general explanation of modelling in LS-DYNA.

6.1 Material Models

Three different concrete material models were used in the report CDPM2,CSCM and Winfrith. In the following section there will be a short introduction to each.To validate that the concrete models where behaving as expected, cube tests were simulated in LS-DYNA. The cube tests were performed because of their simplicity and the possibility to use one solid element.

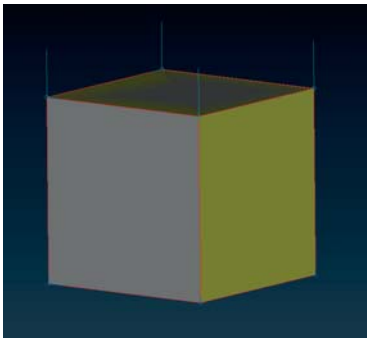

Figure 6.1.1: *Cube model in ANSA*

Figure 6.1.1 show the cube model used, the sides where 15 cm long and concrete properties was added through the different material models. It consisted of one solid element with one gauss-point that was stabilized by constraints added in x, y and z direction on three sides and the load was applied through forced displacement of the top four nodes. To be certain the models behaved as expected the cube in tension was loaded and then unloaded two times to visualize the change in stiffness and permanent displacement that occurs, also triaxial compression was investigated.

6.1.1 Concrete damage plasticity model 2

The concrete material CDPM2 is an modified version of CDPM which was proposed by Grassl and Jirásek (2006) taking into account the effects of strain rate. In CDPM there was only one damage parameter for both compression and tension which was expanded upon in CDPM2 to separate the accumulation of damage in the two states (Nyström, 2013). As the name suggest the model expresses damage in a combined damage-plasticity model. The damage model and plasticity models are explained separately in Section 3.4. Since it is a combined behaviour both the permanent plastic strain and reduction of Young's modulus is present in CDPM2.

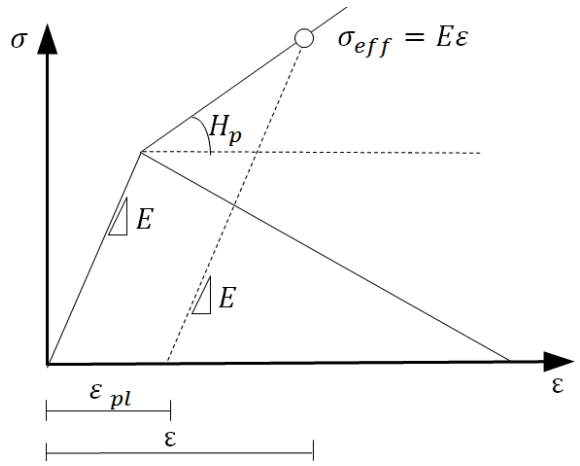

(a) *Effective stress and plastic deformation.*

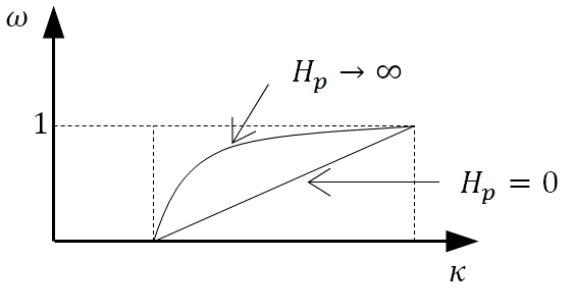

(b) *Influence from hardening on the damage parameter.*

Figure 6.1.2: *Plasticity part and hardening of CDPM2.*

As visualised in Figure 6.1.2a the deformations first follow the plasticity model and calculates the effective elastic stress at ε and the corresponding plastic strain ε_{pl}. In the same figure the hardening variable H_p is diplayed. If $H_p = 0$ the model becomes a pure plasticity model and if $H_p \to \infty$ it becomes a pure damage model. The hardening is another addition to CDPM in which the post-peak regime was formulated as having a perfect plastic behaviour. The influence of the hardening variable on ω can be seen in Figure 6.1.2b. There are two ways of describing the damage accumulation in tension, one being linear and the other being bilinear both are evaluated in this report.

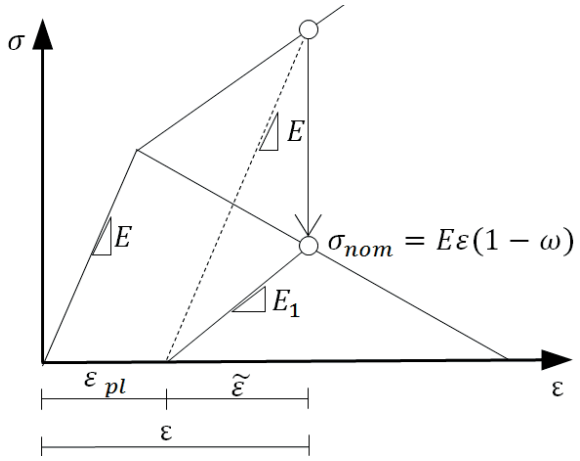

(a) *Nominal stress and new Youngs modulus.*

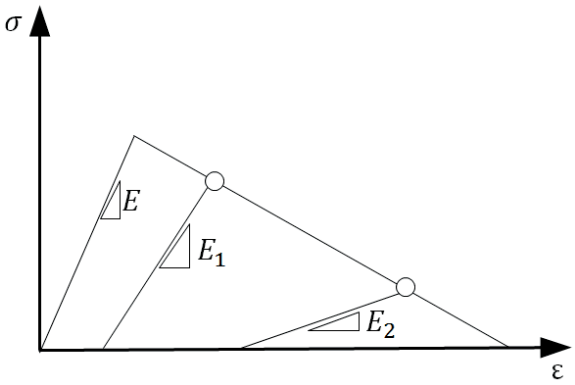

(b) *A CDPM2 material that has been loaded twice.*

Figure 6.1.3: *Combined behvaiour of CDPM2*

The plastic deformation obtained in the plasticity model in Figure 6.1.2a then becomes the new point of equilibrium for the material. The damage model that normally would return to origin will now instead oscillate around ε_{pl} with a new Young's modulus E_1. The nominal stress can be seen in Figure 6.1.3a and is calculated based upon the damage accumulation in ω. The combination of the two models yields the combined behaviour of both with a plastic deformation and a reduced Young's modulus, an example of a specimen that has been loaded and unloaded twice is visualized in Figure 6.1.3b.

Cube test on CDPM2

Cube tests for the CDPM2 model were simulated in LS-DYNA in the same manner as explained in Section 6.1 in order to validate that the model was behaving as expected. The stress - strain relationship for a cube with a compressive strength of $f_c = 42$ MPa, the tensile strength was set to $f_t = 2.78$ MPa and can be seen in Figure 6.1.4. In the same figures the softening of the material in both tension and compression can be seen.

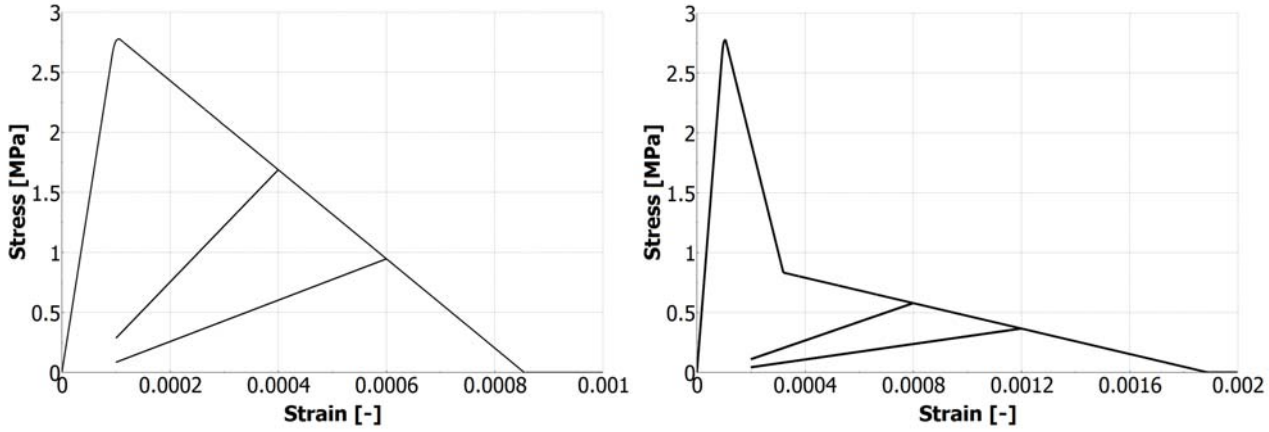

(a) *Stress - Linear strain relationship in tension* (b) *Stress - Bilinear strain relationship in tension*

Figure 6.1.4: *Tensile cube test on CDPM2*

As can be seen in Figure 6.1.4 in both compression and tension the ultimate capacity of the concrete was reached and then started to decrease as expected. In tension both the linear and bilinear behaviour of the model can be seen.

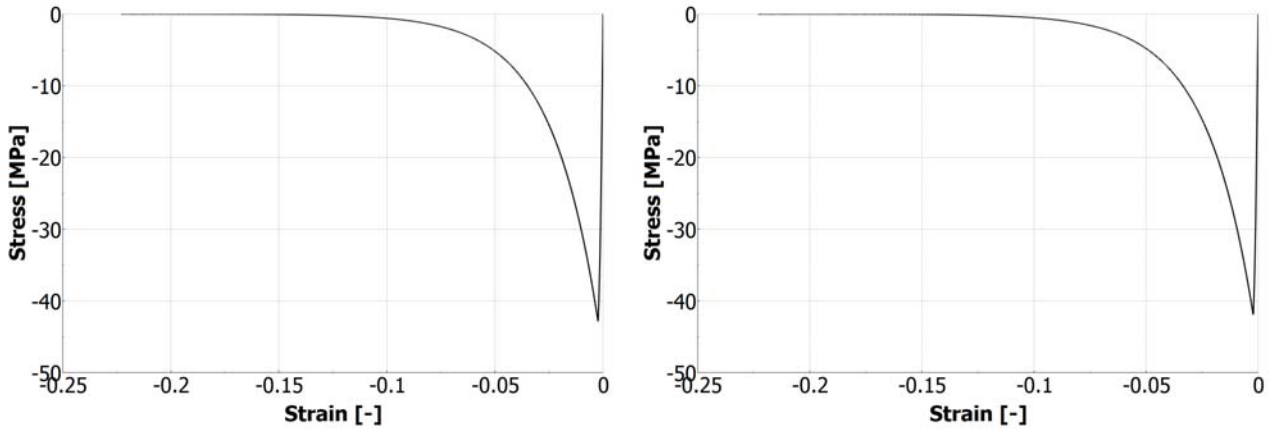

(a) *Stress - Linear strain relationship in compression* (b) *Stress - Bilinear strain relationship in compression*

Figure 6.1.5: *Compression cube test for CDPM2*

In Figure 6.1.6a the change in stiffness when the cube is reloaded is visible as well as the permanent deformation from the plasticity part of the model. The increase in capacity when the concrete is subjected to a tri-axial pressure can seen in Figure 6.1.6b. The main aspects of the material model were therefore deemed to be behaving as expected.

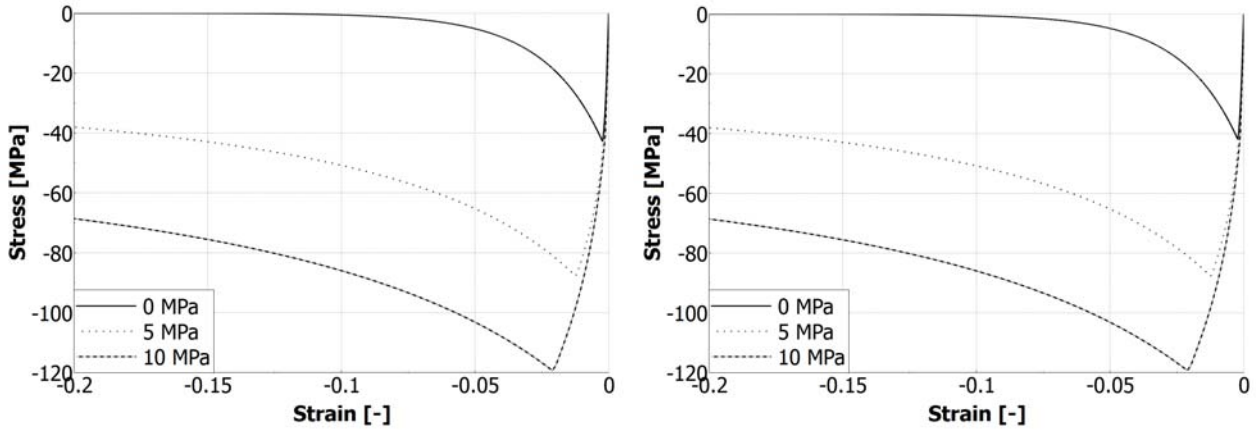

(a) *Stress - Linear strain relationship in triaxial compression*(b) *Stress - Bilinear strain relationship in triaxial compression*

Figure 6.1.6: *Triaxial cube test on CDPM2*

6.1.2 Continuous surface cap model

The continuous surface cap model, CSCM, was developed especially to handle dynamic loads when modeling roadside safety structures (Murray, Y. Abu-Odeh, A and Bligh, R. (2007)). The main feature of the model is that the shear failure and compaction surface are "mixed" together to form a smooth or continuous surface(Schwer, L. Murray, Y. 2002). Compared to traditional two-surface cap models where the two are separate.The smooth stress space of CSCM is visualized in Figure 6.1.7.

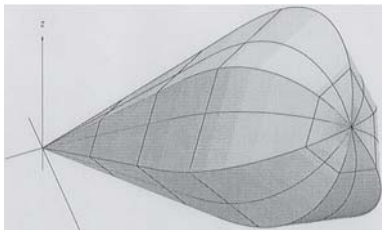

Figure 6.1.7: *Stress space visualization for CSCM (Schwer, L. Murray, Y. 2002)*

There are two variants of the model MAT-CSCM and MAT-CSCM-CONCRETE. In the first one every parameter such as concrete strength, Young's modulus, hardening, rate-effects have to be defined. As for the second one the number of parameters that needs to be defined by the user are reduced to only unconfined compressive strength, aggregate size and units. The additional parameters are then automatically generated based upon a set of default values that corresponds to compressive strengths ranging from 32 MPa up to 58 MPa and an aggregate size between 8 and 32 mm. Both versions of the model has the option to take strain rate into account. The model has a softening behaviour where damage accumulates in two variables, one for tension and one for compression.

The softening in both stress states follow the same relationship where the stress is multiplied with a scalar, d, to obtain the nominal stress which is expressed in the following manner:

$$\overline{\sigma_{ij}} = (1-d)\sigma_{ij} \tag{6.1.1}$$

Where:

$d =$ Damage variable
$\sigma_{ij} =$ Stress
$\overline{\sigma_{ij}} =$ Nominal Stress

The damage parameter will start accumulating as soon as the ultimate stress is reached and will then continue accumulating until it reaches $d = 1$ and at this point the nominal stress is equal to zero.

Cube test on CSCM

Cube tests for the CSCM model where simulated in LS-DYNA in the same manner as explained in Section 6.1 in order to validate that the model was behaving as expected. The stress - strain relationship for a cube with a compressive strength of $f_c = 36.4$ MPa, the tensile strength was automatically calculated by LS-DYNA to be $f_t = 2.813$ MPa and can be seen in Figure 6.1.8. In the same figures the softening of the material in both tension and compression can be seen. In

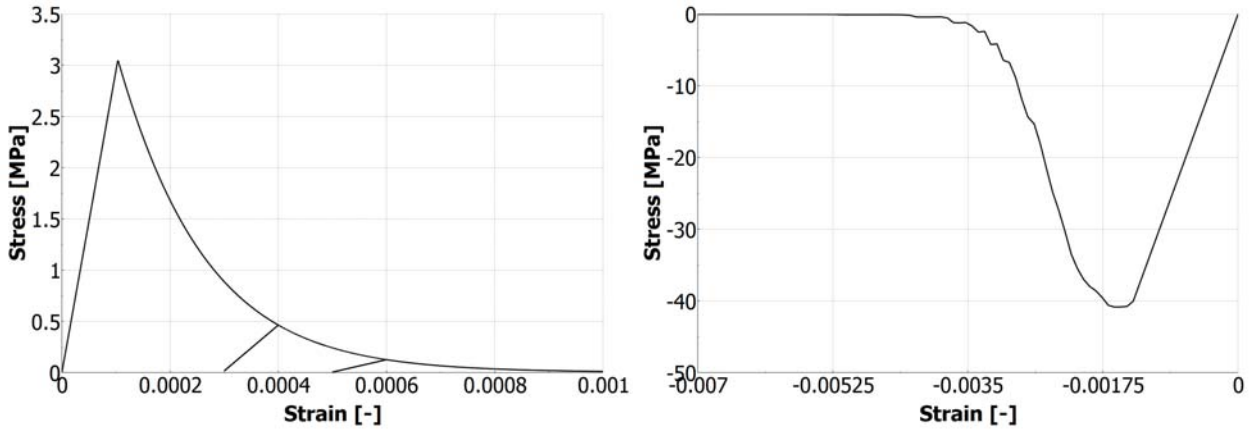

(a) *Stress - Strain relationship in tension* (b) *Stress - Strain relationship in Compression*

Figure 6.1.8: *Cube test on CSCM*

Figure 6.1.8a the material was loaded and unloaded twice in tension, to visualize the reduction in Young's modulus and constant deformations that are obtained after the ultimate capacity has been reached. The cube was also subjected to confining pressure to see the effect of triaxial stress state. In Figure 6.1.9 the increase in ultimate strength can be observed, it can also be seen that the model is unstable, this behaviour was also observed by Wu, Y. Crawford, J.E. and Magallanes J.M. (2012)

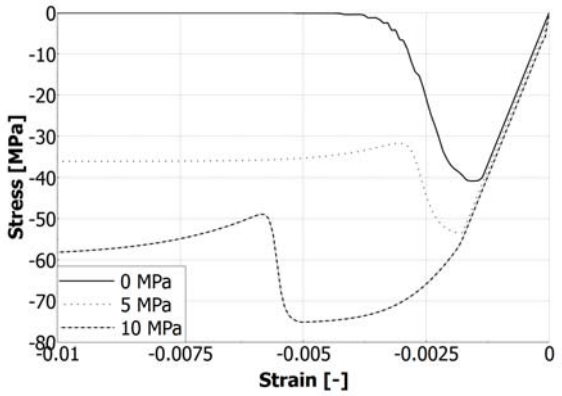

Figure 6.1.9: *Triaxial compression on CSCM*

6.1.3 Winfrith

The Winfrith model in LS-DYNA is a basic plasticity model with a Mohr-Coulomb behaviour with a third stress invariant to treat the triaxial extension in both tension and compression. The damage in tension has a strain softening behaviour to make the material more regular via crack width, fracture energy and aggregate size. There are three orthogonal crack planes in each solid Winfrith element (Schwer, L. 2011). There are two different versions of the model, one which is plain concrete and an other which has the option to add smeared reinforcement to the material by increasing the stiffness. Only the version without smeared concrete has the option to account for strain rate. The Winfrith model accounts for damage in both tension and compression by two separate variables, in tension the damage variable , d, can take on the value of either $0, 1, 2$ or 3 where 0 is no damage. When the ultimate tensile strength has been reached the damage is 1 if the element then is unloaded or subjected to compression, crack closing, the damage will be 2. When the all of the capacity has been depleted in the element the damage is set to 3 this accumulation is seen in Figure 6.1.10.

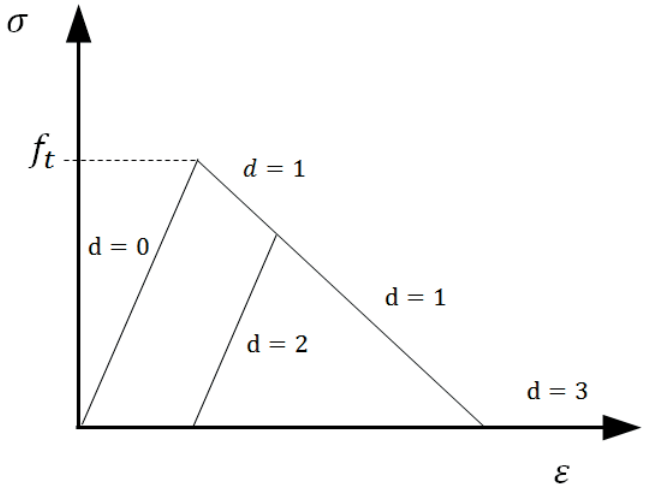

Figure 6.1.10: *Damage accumulation in Winfrith*

Cube test on Winfrith

Cube tests for the Winfrith model where simulated following the same cube set-up as explained in Section 6.1 in order to validate that the model was behaving as expected. The compressive strength of the concrete was set to $f_c = 36.4$ MPa as previously and the tensile strength was $f_t = 2.78$ MPa as the cube test show in Figure 6.1.11 these ultimate values where reached.

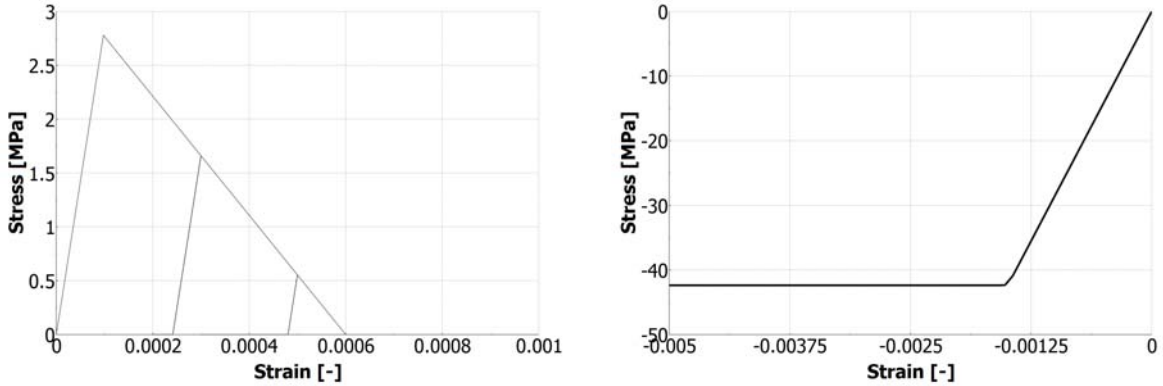

(a) *Stress - Strain relationship in tension* (b) *Stress - Strain relationship in Compression*

Figure 6.1.11: *Cube test on Winfrith*

In in both figures the plastic behaviour of the model is visible and the softening behaviour and damage accumulation in tension. When subjected to triaxial compression it can be observed in Figure 6.1.12 that Winfrith is unable to predict the behaviour, this is because it lacks the ability to model shear dilation effects. When subjected to uniaxial compression it can again be seen to not behave in a satisfactory way with no softening behaviour. It can however be seen that the ultimate compression strength is increased, but this is due to the way the confining pressure is applied. This phenomena was also observed by Schwer, L. (2011).

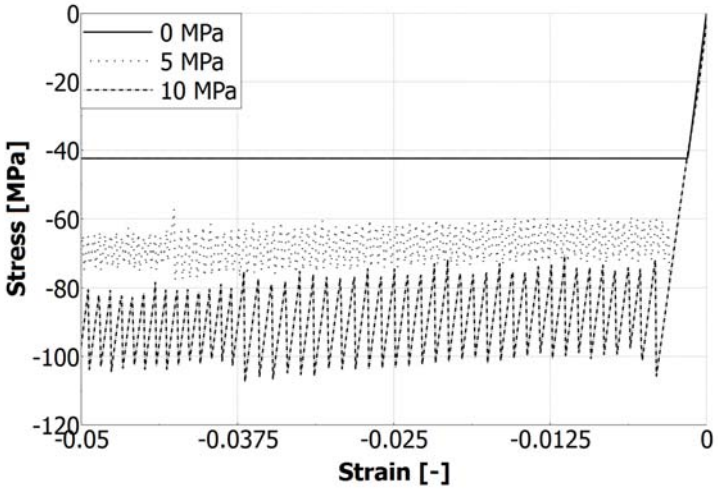

Figure 6.1.12: *Triaxial compression on Winfrith*

6.2 Reinforcement modelling

The reinforcement was modelled using the the material MAT-PLASTIC-KINEMATIC which is a cost effective material that has an elastic plastic behaviour (LS-DYNA MANUAL II. (2012)). It is available for use on beam, solid and shell elements. It also has the ability to model hardening by defining a tangent modulus. The stress strain behaviour with hardening is seen in Figure 6.2.1.

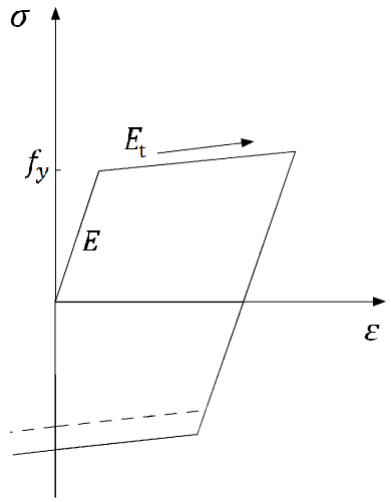

Figure 6.2.1: *Elastic-plastic behaviour of MAT PLASTIC KINEMATIC (LS-DYNA MANUAL II. 2012)*

The bending reinforcement was modelled using one dimensional beam elements that provide both axial and bending stiffness to the beam. While the shear reinforcement was modelled using truss elements that only provide axial stiffness,truss elements also reduce simulation time. Shear reinforcement is only mainly subjected to axial stresses and therefore beam elements are redundant, for both element types cross-sectional area, yield stress and Young's modulus is defined. To get interaction between the reinforcement and concrete two different methods were examined which will be explained further in the following sections.

6.2.1 Reinforcement concrete share nodes

One way of modelling the interaction between concrete and reinforcement is to let the beam elements and solid concrete elements share nodes. In this case the reinforcement is considered to be fully bonded to the concrete (Sangi, A.J 2011).The beam elements has to be placed in between the solid elements as can be seen in Figure 6.2.2.

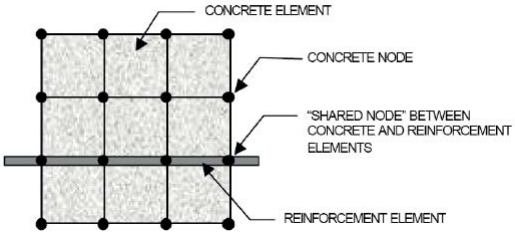

Figure 6.2.2: *Shared nodes between concrete and reinforcement (Sangi, A.J 2011)*

The problem with this method is that mesh size for the solid elements becomes dependent on the reinforcement placement and vice versa.

6.2.2 Constrained Lagrange in solids, CLIS

When simulating reinforced concrete it is not always possible to place all the reinforcement on shared nodes with the solid concrete. Then an arbitrary Lagragian-Eulerian constraint can be applied. It allows the mesh of beams and solids to be defined individually and then superimposed (Schwer, L. 2014) an example can be seen in Figure 6.2.3. It functions by coupling the beam elements to the solids and making the motions of both uniform. There are many inputs that can be defined for CLIS in LS-DYNA but when modelling reinforcement only a few are necessary. The master nodes belong to the concrete while the beam elements are defined as slave nodes (LS-DYNA MANUAL I. 2012), for all the variables example can be seen in AppendixB.

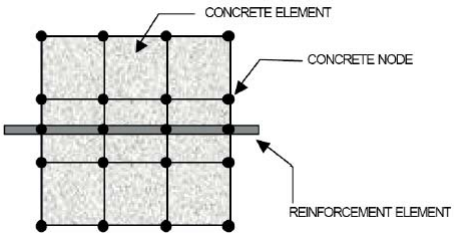

Figure 6.2.3: *Arbitrary beam placement in solid elements*

Reinforcement methods comparison

To investigate the behaviour of the two ways of modelling reinforcement interaction a weight falling from $0.3m$ hitting a beam was modelled with reinforcement on nodes and CLIS. This was performed with all material models and all of them displayed the same behaviour.Figure 6.2.4 shows the displacement history for CSCM with both reinforcement methods.

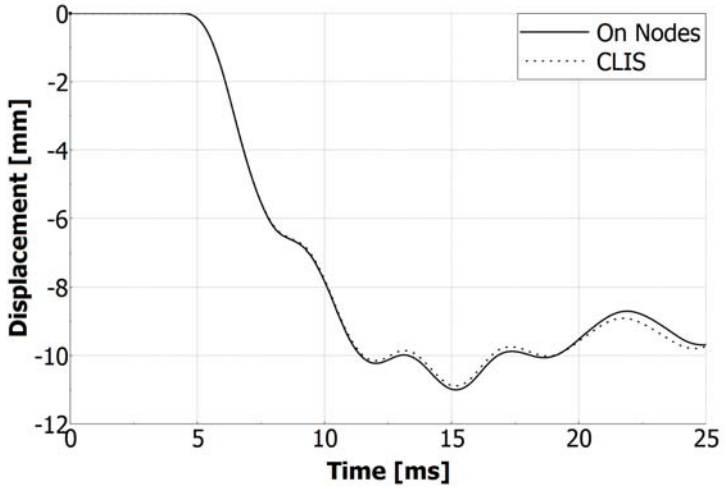

Figure 6.2.4: *Displacements of Case 1 with material model CSCM and reinforcement on nodes and with CLIS*

In Appendix D the results from the other materials can be seen. In CDPM2-Bilinear, CDPM2-Linear and CSCM the difference in maximum displacement was insignificant though with Winfrith the difference was slightly larger. Even though minor differences were observed CLIS will be used in all further simulations because of the possibility of place reinforcement at arbitrary positions and the fact that it is more convenient to work with.

6.3 Solid Elements

The concrete is modelled using cubic eight-node hexahedron elements, each element is assigned "ELFORM-1" which is an underintegrated element formulation using only one integration point in the middle of the element as can be seen in Figure 6.3.1.

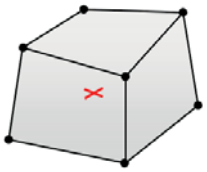

Figure 6.3.1: *Eight-node hexahedron with integration point in the middle.*

This element formulation is efficient, accurate and works even for severe deformations. However, hourglass stabilization is required and will affect the solution significantly (Erhart, T. 2011).

6.4 Hourglassing

Hourglassing are nonphysical deformations that produce no stress and can occur in all underintegrated elements (Livermore Software Technology Corporation, 2015).Fully integrated elements experience no hourglassing but are more expensive. Figure 6.4.1 show an example of hourglassing deformation in an underintegrated shell element, here neither of the dotted lines or the angle between them has changed. Since integration points only has stress components in x, y and z direction it has no stiffness in this mode. In a coarse mesh this mode can propagate and produce meaningless results.

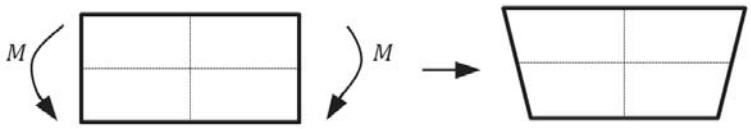

Figure 6.4.1: *Shell element subjected to a moment and corresponding deformations with the integration point in the middle.*

To resist these deformations internal hourglass forces are applied, there are several different formulations available in LS-DYNA for computing these forces. The default in LS-DYNA is a viscous formulation, TYPE 1, that generate hourglass forces proportional to the nodal velocities. It is best suited for high rate scenarios for example explosions. Moreover it can not recover from previously accumulated deformations. TYPE 6 is an assumed strain, co-rotational stiffness formulation that is recommended by the LS-DYNA support to be used for underintegrated elements (LS-DYNA Support, 2015). It assumes a strain field and uses the elastic properties to calculate an assumed stress field. This field is then integrated over the element domain and thereby developing hourglass forces making the element behave like a fully integrated element. The level of hourglass energy should not exceed 10% of the internal energy.

6.5 Contact surfaces

Contact surfaces must be defined to capture the interaction between different parts of the model. In this particular model interaction occurs between the beam and the supports, between the beam and the drop-weight. All contacts between the beam and external objects is captured using the AUTOMATIC-SURFACE-TO-SURFACE contact which is a little bit more expensive than other contacts. However this contact is simple to use and can, among other things, log the forces that occur during loading which is of interest in this analysis.

7 Beam Case I - Drop-weight experiment on a reinforced concrete beam

A good way to verify a FE-model and its capability to capture the desired physical phenomenon is by comparison to real life experiments. In this section a "drop-weight experiment" on a reinforced concrete beam is presented and analyzed with the purpose to recreate the experiment using FEM. The results obtained from the FE-model are then compared to the experimental results in order to verify that the modelling techniques used to model reinforced concrete beams are correct. The validation of the relatively simple FE-model serves as an approval to continue with the model and to step-wise make it more complex.

7.1 Experimental test set-up for Beam Case I

A reference is made to Fujikake, K. Li, B. and Soeun, S. (2009) for a thorough explanation of the entire experimental study as only parts of it is presented below.

The drop-weight machine used in the test can be seen in Figure 7.1.1. A beam is resting on supports that prevents vertical movement of the beam at the supports but still allows the beam ends to rotate freely. This support arrangement will hold the beam in place during dynamic vibration, and at the same time no support moments will occur due to partial fixation at the beam ends. A drop-weight with the mass of 400 kg is dropped in the middle of the span from the heights 0.3 m and 1.2 m. The drop-weight has a hemispherical impact surface with a radius of 90 mm.

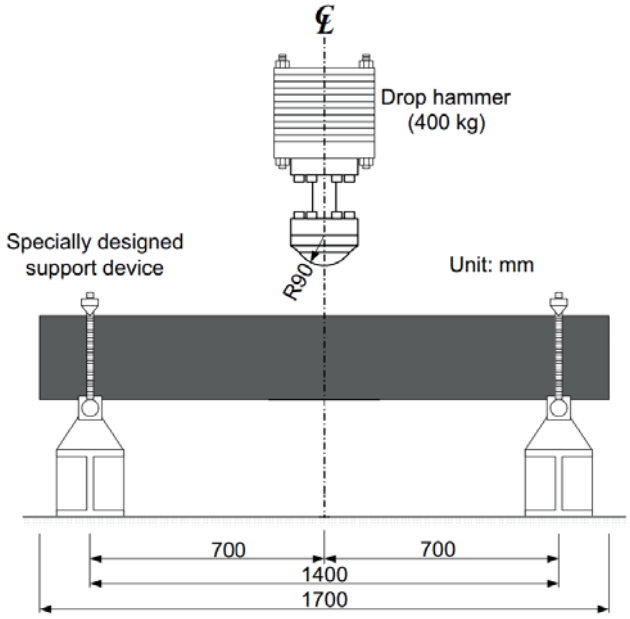

Figure 7.1.1: *Experimental test set-up for Beam Case I (Fujikake, K. Li, B. Soeun, S. 2009).*

As illustrated in Figure 7.1.2 the test beam has a length of 1700 mm, a height of 250 mm and a width of 150 mm. The longitudinal reinforcement consists of symmetrical top- and bottom reinforcement, $\phi 16$, with a yield capacity of 426 MPa. Stirrups are placed along the beam with a spacing of 75 mm and a yield capacity of 295 MPa.

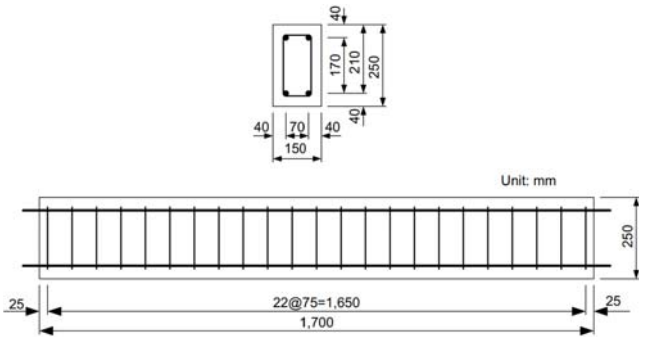

Figure 7.1.2: *Beam geometry and reinforcement arrangement for Beam Case I (Fujikake, K. Li, B. Soeun, S. 2009).*

The beam geometry as well as the drop-weight data presented in Figure 7.1.1 and Figure 7.1.2 are summarized in Table 7.1.1 and Table 7.1.2 respectively.

Table 7.1.1: *Summarization of the beam geometry and reinforcement arrangement.*

$Concretebeam$	$length_{span}$ [mm]	$height$ [mm]	$width$ [mm]
	1400	250	150
	$effectiveheight_{top}$ [mm]	$effectiveheight_{bottom}$ [mm]	$stirrups_{spacing}$ [mm]
	40	210	75

Table 7.1.2: *Summarization of the drop-weight data.*

$Drop-weight$	$R_{cylinder}$ [mm]	$h_{cylinder}$ [mm]	$R_{hemisphere}$ [mm]
	150	210	90
	$mass$ [kg]	$drop-height_1$ [mm]	$drop-height_2$ [mm]
	400	300	1200

7.1.1 Experimental results for Beam Case I

The experimental results can be seen in Figure 7.1.3 and Figure 7.1.4. Figure 7.1.3 displays the crack patterns obtained when the drop-weight fell from 0.3 m and 1.2 m. Figure 7.1.4 shows the corresponding displacements.

(a) *1.2 m drop-height.* (b) *1.2 m drop-height.*

Figure 7.1.3: *Crack patterns from the experimental results for Beam Case I (Fujikake, K. Li, B. Soeun, S. 2009).*

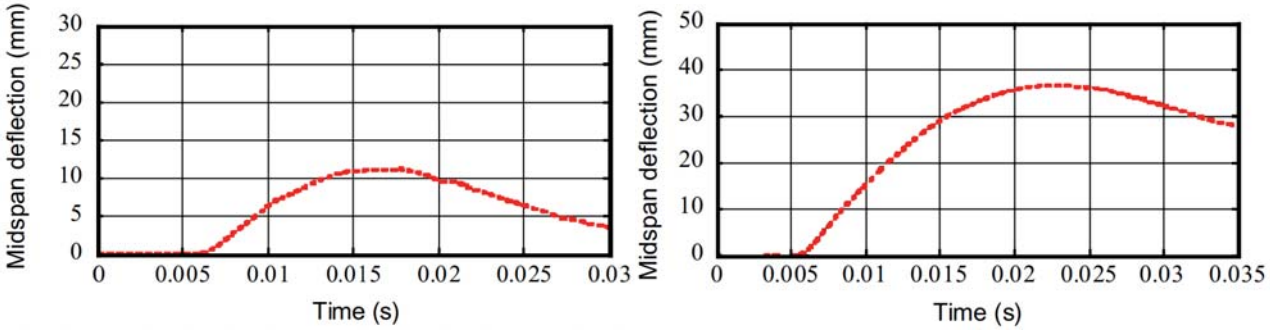

(a) *1.2 m drop-height.* (b) *1.2 m drop-height.*

Figure 7.1.4: *Maximum midspan deflections from the experimental results for Beam Case I (Fujikake, K. Li, B. Soeun, S. 2009).*

7.2 Creation of the FE-model - Beam Case I

In this section the drop-weight experiment is recreated in the FE-software LS-DYNA. The modeling procedure is explained with regard to choice of element types and contact surfaces between interacting parts in the model. In Chapter 8 the established FE-model will be compared to the experimental test results presented in Section 7.1.1 using all the concrete material models introduced in Chapter 6. This is done in order to evaluate which concrete model that best captures the dynamic response of the beam.

The entire FE-model is described in Appendix B as a text input file. This is the file that is read by the LS-DYNA solver in order to execute the FE-calculation. Detailed numerical information about materials, elements, loads, contacts, hourglass options, control cards etc. can be found there. Material and element properties are described in Chapter 6.

To capture the boundary conditions stated in the experiment set-up, i.e. clamped beam ends with full rotational freedom, the FE-model is provided with four cylindrical supports providing a span length of 1.4 m. This can be seen in Figure 7.2.1. The cylindrical supports are modeled as rigid bodies that are not allowed to move or rotate.

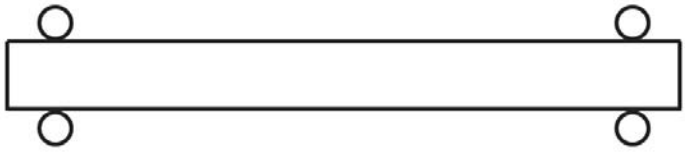

Figure 7.2.1: *Cylindrical supports providing clamped ends with full rotational freedom.*

The drop-weight is modelled as a rigid body that is allowed to move only in the vertical direction. It consists of a 210 mm tall cylinder with a radius of 150 mm the bottom is a hemisphere with radius 90 mm, making the whole part 300 mm tall. The volume was then calculated and the density of the rigid material was then set so that the total weight was 400 kg. Initial velocities were applied to it, by using the LS-DYNA function *INITIAL-VELOCITY-RIGID-BODY. The two velocities were calculated to be $v_1 = 2.42$ m/s and $v_2 = 4.85$ m/s. The concrete was modeled with underintegrated, ELFORM1, solid elements and because of this the hourglass energies had to be controlled. Two hourglass formulations, $HG-type1$ and $HG-type6$, were examined in this case.

The bending reinforcement is modeled using beam elements while the shear reinforcement consists of truss elements. Both of them will use the material model *MAT-PLASTIC-KINEMATIC, which is a cheap and efficient model that despite its name has an elastoplastic behaviour. Both the bending and shear reinforcement was then coupled to the concrete by using the CLIS constraint. To capture the interaction between the individual parts of the model, *AUTOMATIC-SURFACE-TO-SURFACE contact was used between the supports/beam and drop-weight/beam.

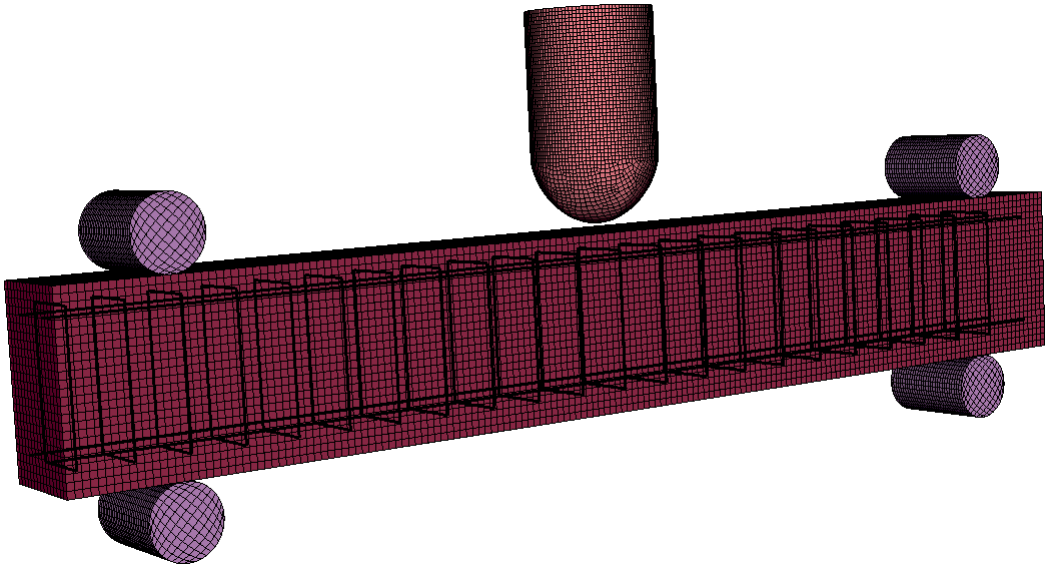

Figure 7.2.2: *FE-model of Beam Case I.*

This configuration which can be seen in Figure 7.2.2 will be used in the evaluation of the concrete material models described in Chapter 8.

7.3 Verification of the FE-model - Beam Case I

The created FE-model must be verified to ensure that it can represent the real life beam behaviour in a good way. A successful verification of the modelling technique for this relatively simple FE-model implies that it can be used as a good basis for more complex models. The verification process involves both a static load case and a dynamic load case. Means of verification for each load case is first introduced followed by the actual verification results.

7.3.1 Static load case - Means of verification and verification results

A rough indication of the models ability to perform well is given by the contour plots. By applying a well-defined load, in this case a point load in the middle of the span, the beam response can be predicted and sought after in the contour plots. Figure 7.3.1 shows contour plots representing von Mises stress distribution in state I, a crack pattern in state II ($P = 40$ kN) and the crack pattern in the ultimate limit state ($P = 100$ kN). All images correspond to the expected behaviour of a simply supported beam subjected to a static point load in the middle of the span.

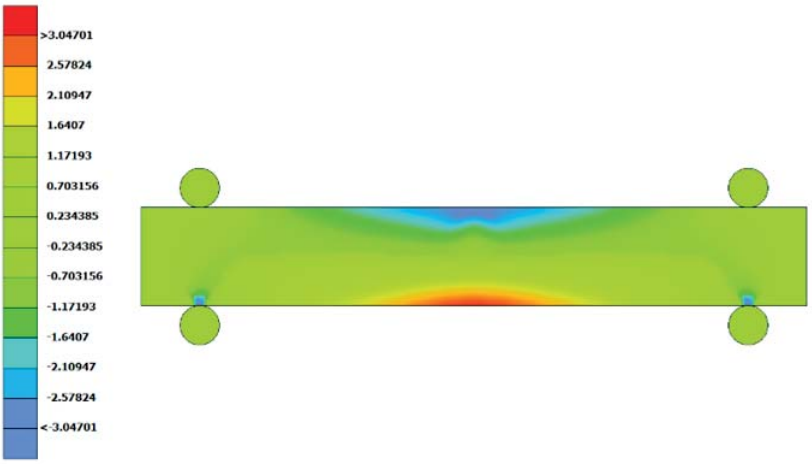

(a) *Von Mises stress distribution just before cracking of the beam.*

(b) *Crack pattern for an applied load of 40 kN.*

(c) *Crack pattern just before failure of the beam.*

Figure 7.3.1: *Contour plots used for a rough verification of the FE-model.*

To ensure that the model provides reasonable numerical results a verification towards Eurocode has been made. The compared parameters is cracking load, deflection just before cracking, deflection somewhere in state II, ULS-capacity and deflection just before failure. Figure 7.3.2 shows a load-displacement curve where the beam is loaded until failure. Points 1) and 3) mark points of interest for the structural behaviour of the beam as well as for the verification, while point 2) only serves as a mean of verification. The structural behaviour of the beam is according to expectations. The beam has a very stiff response up until the cracking load, P_{cr}. After this point, while in state II, the beam response is less stiff due to successive cracking of the beam. Finally, at the load P_{ult}, the reinforcement starts to yield and the beam collapses.

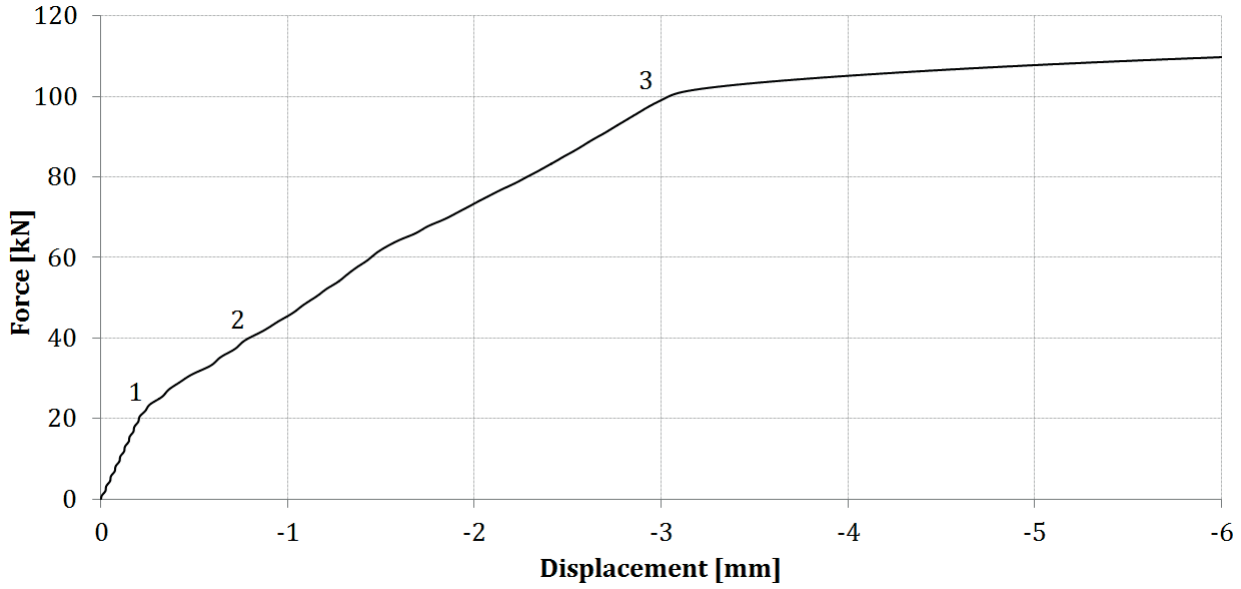

Figure 7.3.2: *Load-deflection curve for the FE-model of Beam Case I when loaded until failure.*

In Table 7.3.1 numerical values for the verification parameters have been extracted from the FE-model and are compared to hand calculations according to Eurocode, which can be found in Appendix E.1. It should be mentioned that the extracted numerical values are somewhat lower than the values that indicates e.g. cracking in Figure 7.3.2. The reason behind this is that the numerical values used in the comparison with the hand calculations is taken at the moment where the very first cracked elements occur in the FE-model. This is in order to get a more fair comparison since the hand calculations are based on the first crack initiation in the section. For a slightly higher load an entire row of elements across the beam width is cracked in the FE-model which better corresponds to the cracking load at the first bend of the curve in Figure 7.3.2.

Table 7.3.1: *Comparison between FE-results and hand calculations according to Eurocode.*

Compared parameter	*FE − model*	*Eurocode*	*Ratio*
P_{cr} [kN]	17.31	16.62	0.96
u_{cr} [mm]	0.178	0.142	0.795
P_{40} [kN]	40	40	1.0
u_{40} [mm]	0.81	1.02	1.258
P_{ult} [kN]	100.4	96.53	0.961
u_{ult} [mm]	3.06	2.585	0.845

The ratios comparing the deflections indicate large differences between the FE-results and the hand calculations. However, since the deflections are very small, even an almost negligible difference gives a major impact on the ratios. Notable in the comparison is that the cracking load as well as the ultimate load corresponds relatively well between the FE-results and the hand calculations.

7.3.2 Dynamic load case - Means of verification and verification results

The dynamic beam response for the FE-model was verified by comparison with the experimental results for Beam Case I presented in Section 7.1.1. A comparison was made for two dynamic load cases where the drop-weight was dropped from 0.3 m and 1.2 m. The experimental results as well as the FE-model results is displayed in Figure 7.3.3 to Figure 7.3.6, showing maximum deflections at midspan and overall crack patterns. A good correlation between the FE-model and the real life experiment was obtained regarding mid span deflections. Identical crack patterns are not possible to get due to the randomness of crack initiations in real life beams. The FE-model displays a smeared crack band along the bottom of the beam for the drop-height 0.3 m while for the 1.2 m drop-height some more distinct cracks have appeared.

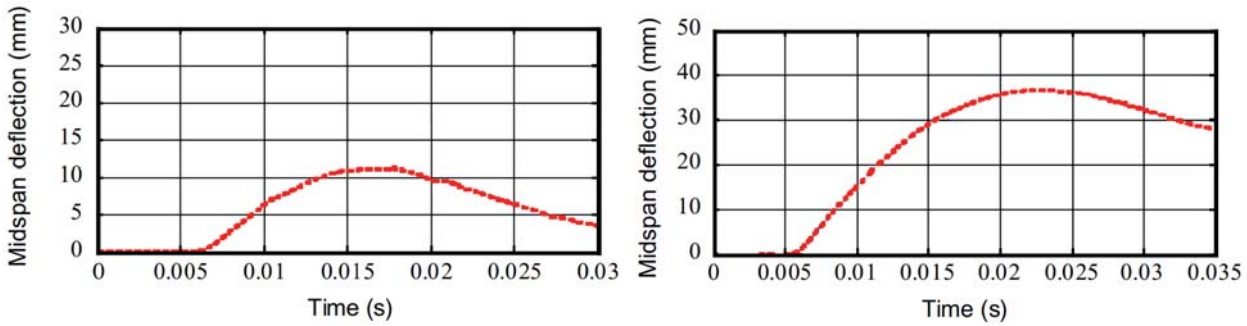

(a) *Displacement history for the drop-height 0.3 m.* (b) *Displacement history for the drop-height 1.2 m.*

Figure 7.3.3: *Experimental results showing the midspan displacement history for Beam Case I.*

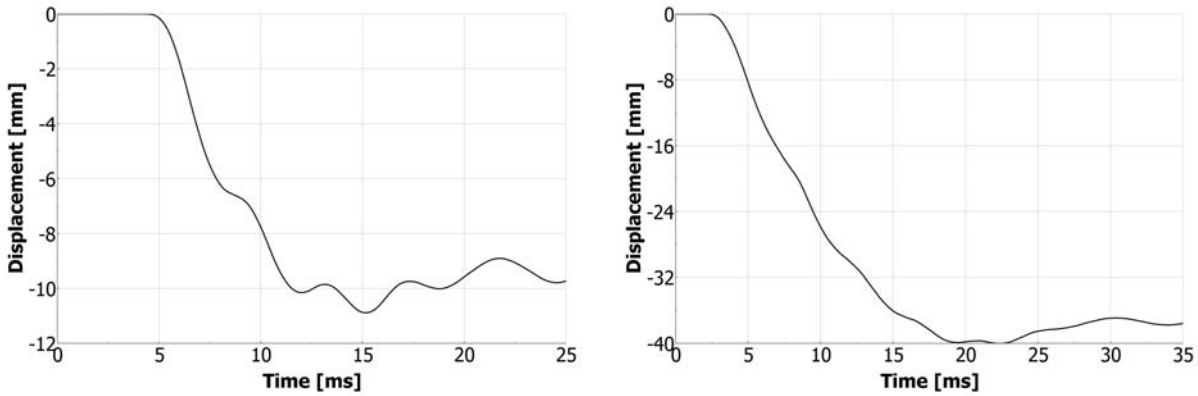

(a) *Displacement history for the drop-height 0.3 m.* (b) *Displacement history for the drop-height 1.2 m.*

Figure 7.3.4: *FE-results showing the midspan displacement history for Beam Case I.*

(a) *Crack pattern for the drop-height 0.3 m.* (b) *Crack pattern for the drop-height 1.2 m.*

Figure 7.3.5: *Experimental results showing the crack patterns for Beam Case I.*

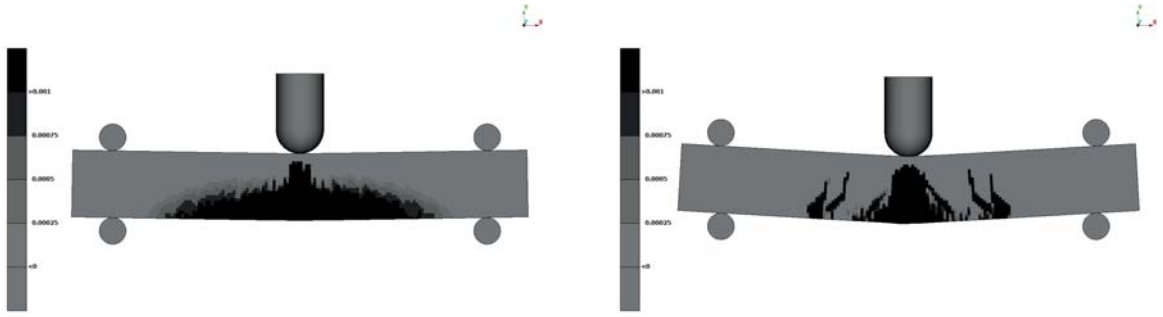

(a) *Crack pattern for the drop-height 0.3 m.* (b) *Crack pattern for the drop-height 1.2 m.*

Figure 7.3.6: *FE-results showing the crack patterns for Beam Case I.*

To further verify the FE-model a Single Degree of Freedom-system (SDOF) representing Beam Case I was established using Matlab. The transformation of dynamically loaded beams into SDOF-systems is thoroughly described in Chapter 5 and the actual Matlab code describing the calculations can be found in Appendix C. Interesting results to compare from the SDOF-calculations is the maximum midspan deflection of the beam which can be seen in Figure 7.3.10 and Figure 7.3.11. The correlations to both the FE-model and the real life experiment are good. It should however be mentioned that the post-impact amplitude of the deflection as well as the periodical wavelength of the vibration is constant due to the absence of damping and the use of a basic plasticity model in the SDOF-system. To make sure that the SDOF, experiment and FE-model was as similar as possible the impulse was calculated from the weight and velocity of the drop weight, $I = mv$.

When the weight falls from 0.3 m the impact velocity is 2.42 m/s which corresponds to an impulse of $I = 968$ Ns. For a fall height of 1.2 m the impact velocity is 4.85 m/s which yields an impulse of $I = 1940$ Ns. The impact forces between the drop-weight and the beam where plotted in LS-DYNA. A similar pattern was then calibrated in MATLAB by changing the time and percent of the total impulse that each impact corresponds to. For a fall height of 0.3 m the impact forces can be seen in Figure 7.3.7.

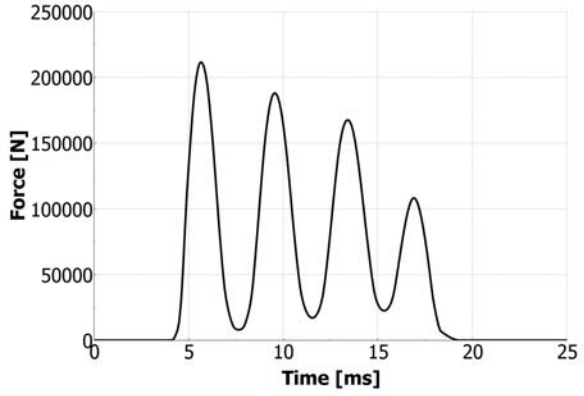

(a) *Impact force between the drop-weight and the concrete beam in LS-DYNA.*

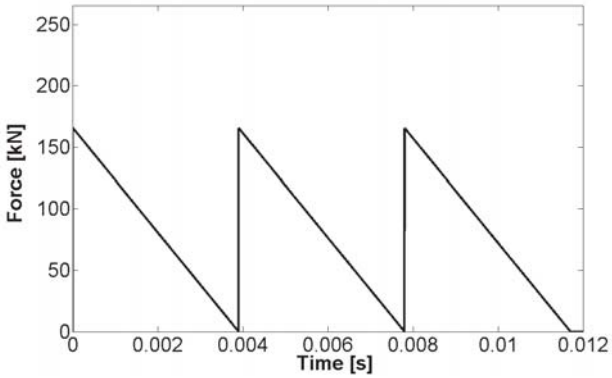

(b) *Calibrated impact force in the SDOF.*

Figure 7.3.7: *Impact force for a drop-height of 0.3 m.*

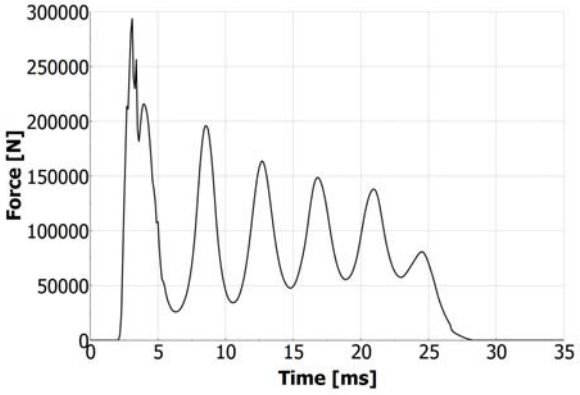

(a) *Impact force between the drop-weight and the concrete beam in LS-DYNA.*

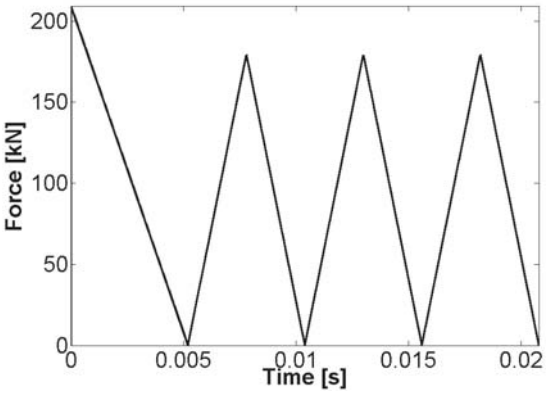

(b) *Calibrated impact force in the SDOF.*

Figure 7.3.8: *Impact force for a drop-height of 1.2 m.*

In Figure 7.3.7a four clear peaks can be seen while in Figure 7.3.7b there are only three. This is because the last peak in LS-DYNA is from the beam hitting the drop-weight pushing it away from the beam. This can be seen by plotting the kinetic energy which is visualized in Figure 7.3.9. After approximately 14 ms the kinectic energy reches zero and afterwards it starts gaining energy once again, from the beam pushing it away.

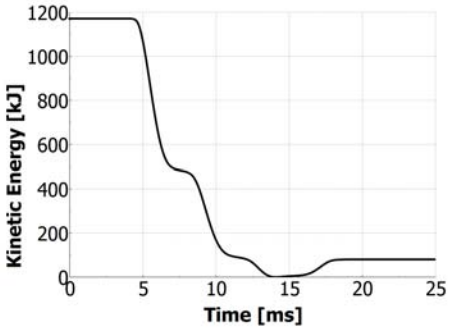

Figure 7.3.9: *Kinetic energy of the drop weight falling from 0.3 m.*

Therefore the final peak is omitted in the SDOF analysis. The same is true for Figure 7.3.8a where there are six peaks and the last two are the beam hitting the weight and therefore only four peaks in the SDOF analysis. The length and top impact force differ between the LS-Dyna impacts and the SDOF impacts, this is because the SDOF system was very sensitive to the time of the peaks and therefore the impulse had to be divided a little bit differently between the peaks to get a good correlation between the deformations of both analyses. The deformations of 0.3 m can be seen in Figure 7.3.10 and 1.2 m in Figure 7.3.11.

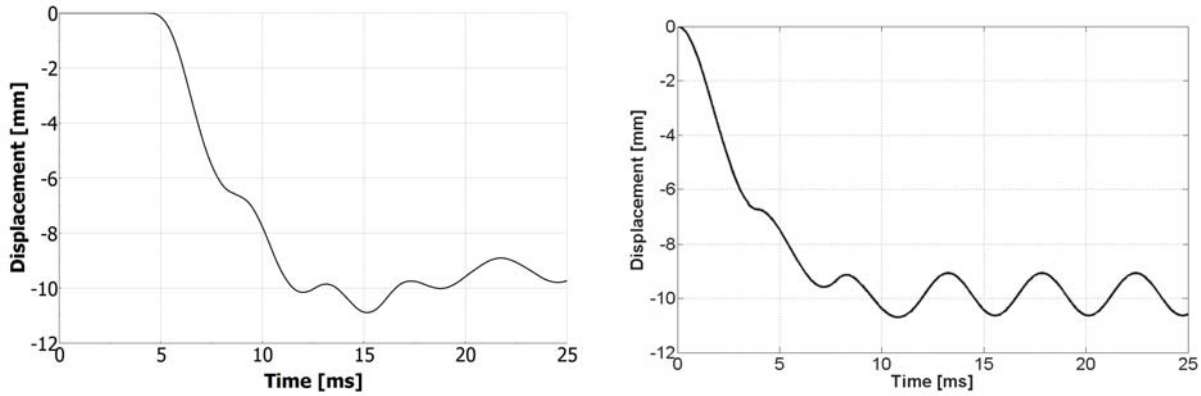

(a) *Midspan deflection in LS-DYNA.* (b) *Midspan deflection in the SDOF.*

Figure 7.3.10: *Midspan deflections for a drop-height of 0.3 m.*

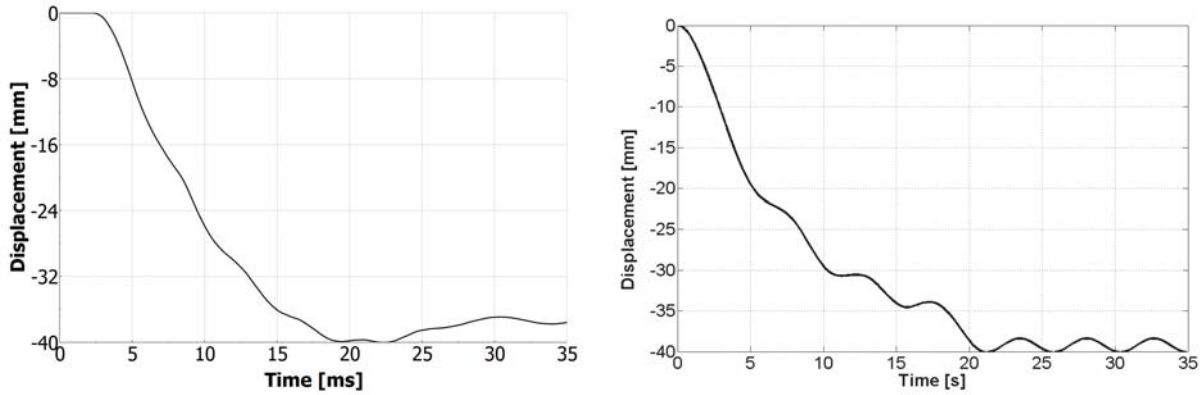

(a) *Midspan deflection in LS-DYNA.* (b) *Midspan deflection in the SDOF.*

Figure 7.3.11: *Midspan deflections for a drop-height of 1.2 m.*

Figure 7.3.10 and Figure 7.3.11 show that the correlation between peak displacement is good between the two. The behaviour after peak displacement differs because of the difference in model behaviour, CSCM having combined damage and plasticity behaviour while the SDOF has a basic plasticity behaviour.

8 Evaluation of the material models with regard to performance during impact loading

In this chapter the concrete material models CDPM2-bilinear, CDPM2-linear, CSCM and Winfrith will be evaluated regarding their performance during impact loading. The evaluation is based on Beam Case I, presented in Chapter 7, where the verified FE-model runs with each material model and the results are compared to the experimental results. Parameters such as mesh convergence ability, efficiency and hourglass sensitivity will also be parts of the evaluation. At the end of this chapter the performance of each material model is discussed and the most appropriate model according to some selection criterions will be chosen to be used in all further analyses.

8.1 Static performance

The material models are compared to each other during a static load case of 40 kN applied at midspan. In Figure 8.1.1 combined load-displacement curves are shown where all material models are represented.

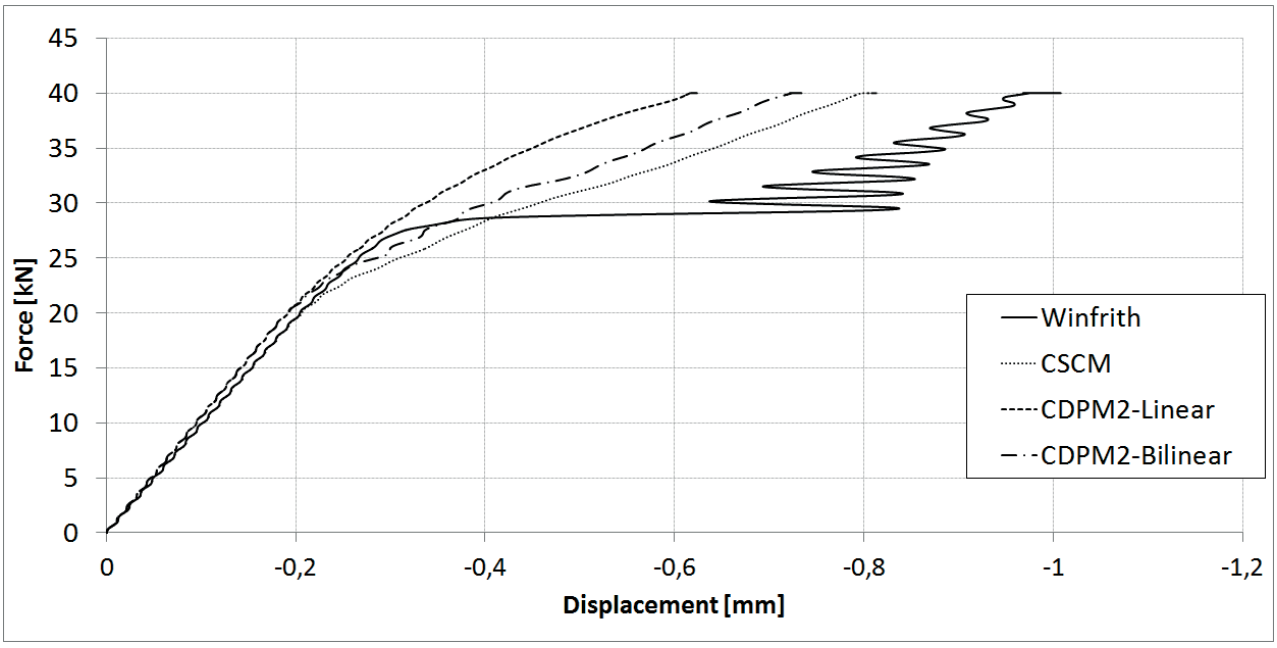

Figure 8.1.1: *Force-displacement curves for the material models up until a static load of 40kN.*

The CDPM2-models as well as CSCM indicates cracking of the beam for a load of about 20 kN, followed by a less stiff beam response up until the static load of 40 kN. Winfrith however displays a significantly higher cracking load followed by an abruptly increased deflection.

In Figure 8.1.2 all material models are loaded until failure. It is notable how Winfrith seem to recover from the sudden increase in deflection after cracking, to line up with the same behaviour as the other material models at a load of about 60 kN.

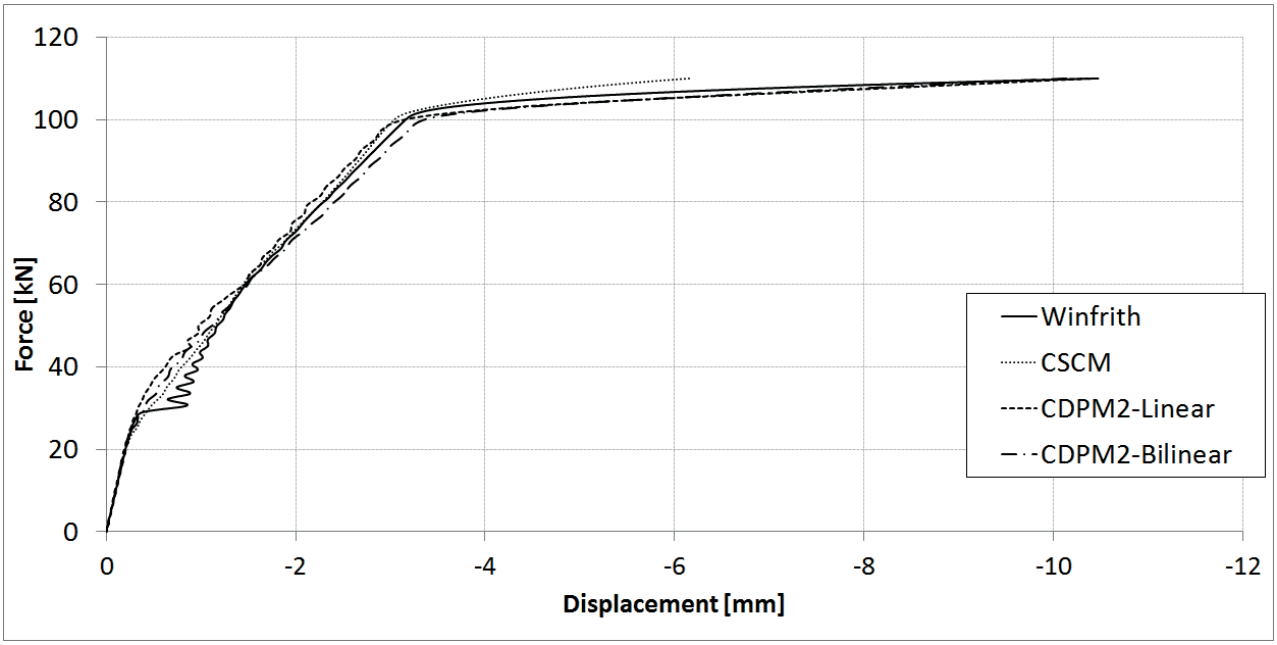

Figure 8.1.2: *Force-displacement curves for the material models up until failure.*

The results from the static analyses are summarized in table 8.1.1 where also the hand calculated results according to Eurocode can be seen.

Table 8.1.1: *Results from static analysis of the different material models and Eurocode. Showing the load at which cracks occur and the displacement at the same moment. Load at which the reinforcement starts to yield and the corre sponding displacement.*

	Crack load [kN]	Disp. at crack [mm]	Load at yield [kN]	Disp. at yield [mm]
Eurocode	16.617	−0.142	96.533	−2.585
CDPM2 − Bilinear	18.06	−0.1742	99.28	−3.28
CDPM2 − Linear	18.06	−0.1742	98.16	−2.946
CSCM	17.4	−0.177	100.4	−3.06
Winfrith	17.4	−0.1758	100.08	−3.166

The crack patterns are compiled for all the materials in Figure 8.1.3 to Figure 8.1.6. They are all plotted using infinitesimal strains because of issues with obtaining a distinct crack pattern with CSCM and Winfrith using the damage parameters. It can however be seen that both CDPM2 models and CSCM exhibit a good behaviour while Winfrith has a more sudden localized crack at midspan.

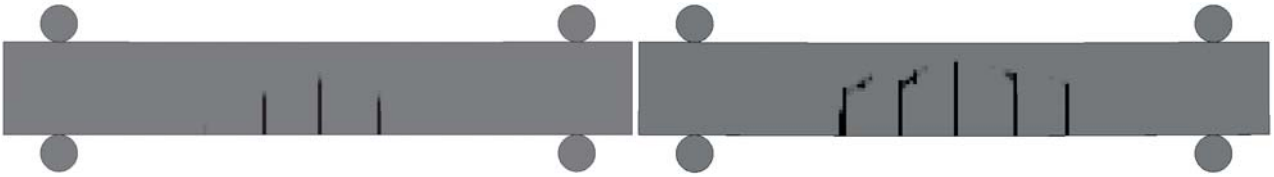

(a) *Crack pattern at 40kN.* (b) *Crack pattern at yeilding of reinforcement.*

Figure 8.1.3: *Static crack pattern for CDPM2-Bilinear.*

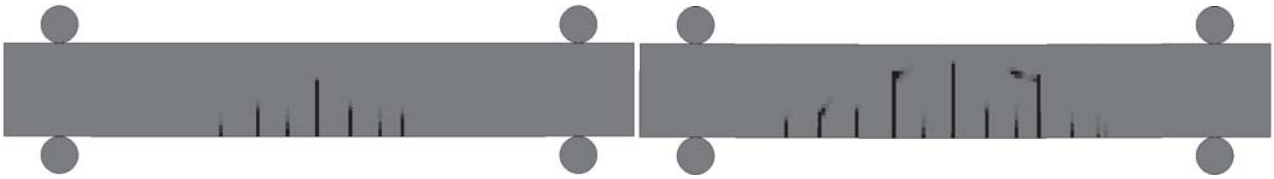

(a) *Crack pattern at 40kN.* (b) *Crack pattern at yeilding of reinforcement.*

Figure 8.1.4: *Static crack pattern for CDPM2-Linear.*

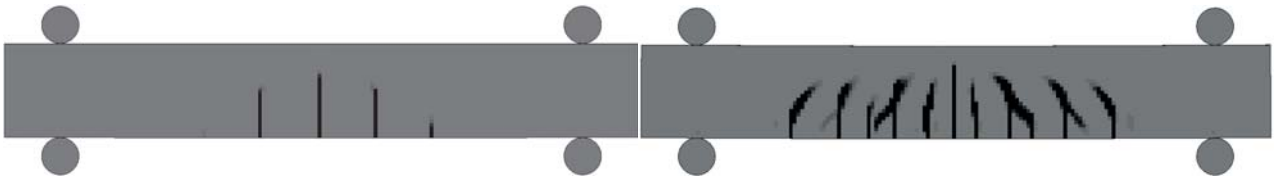

(a) *Crack pattern at 40kN.* (b) *Crack pattern at yeilding of reinforcement.*

Figure 8.1.5: *Static crack pattern for CSCM.*

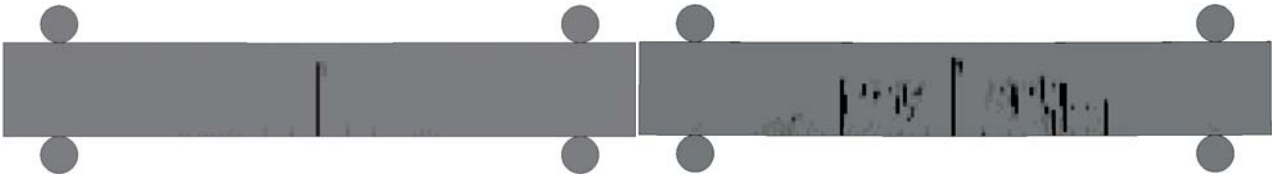

(a) *Crack pattern at 40kN.* (b) *Crack pattern at yeilding of reinforcement.*

Figure 8.1.6: *Static crack pattern for Winfrith.*

8.2 Dynamic performance

As stated in the introduction to this chapter, the material models will be evaluated by comparison to the experimental test results from Beam Case I. Hence, to simplify the comparison, the data from the experiment is shown again here in Figure 8.2.1 and Figure 8.2.2.

(a) *Crack pattern for Beam Case I with at a drop-height of 0.3 m.*

(b) *Crack pattern for Beam Case I with at a drop-height of 1.2 m.*

Figure 8.2.1: *Crack patterns from the Beam Case I experiment.*

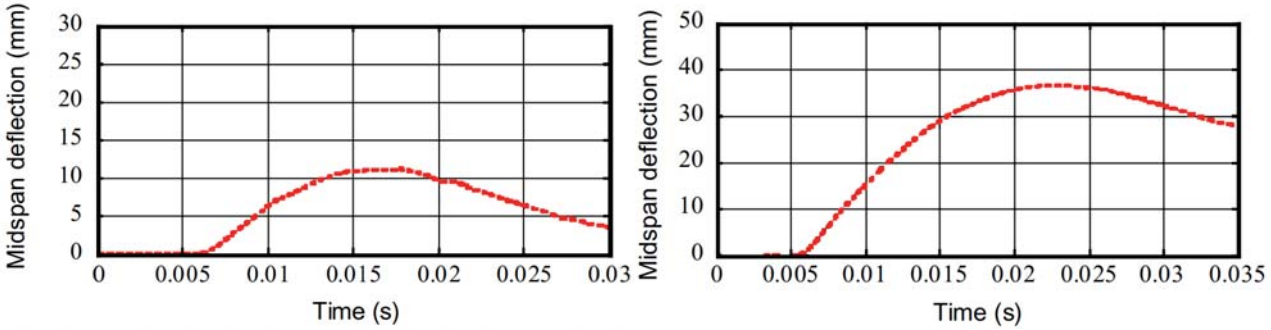

(a) *Displacement for Beam Case I with a drop-height of 0.3 m.*

(b) *Displacement for Beam Case I with a drop-height of 1.2 m.*

Figure 8.2.2: *Displacement history from the Beam Case I expemeriment.*

8.2.1 Mesh convergence

The mesh convergence study is made in order to evaluate the material models capability to converge towards a stable solution during mesh refinement. At the same time their computational efficiencies are measured by clocking the time it takes for the models to run the analyses. Each material model runs using three different mesh sizes. The meshes are created using cubic elements with the element lengths 20 mm, 10 mm and 5 mm, each applied on the FE-model of Beam Case I. In Figure 8.2.3 and Figure 8.2.4 the displacements of the beam is shown when the drop-weight is dropped from a height of 0.3 m. The figure shows the displacements at midspan for each material model using each mesh size.

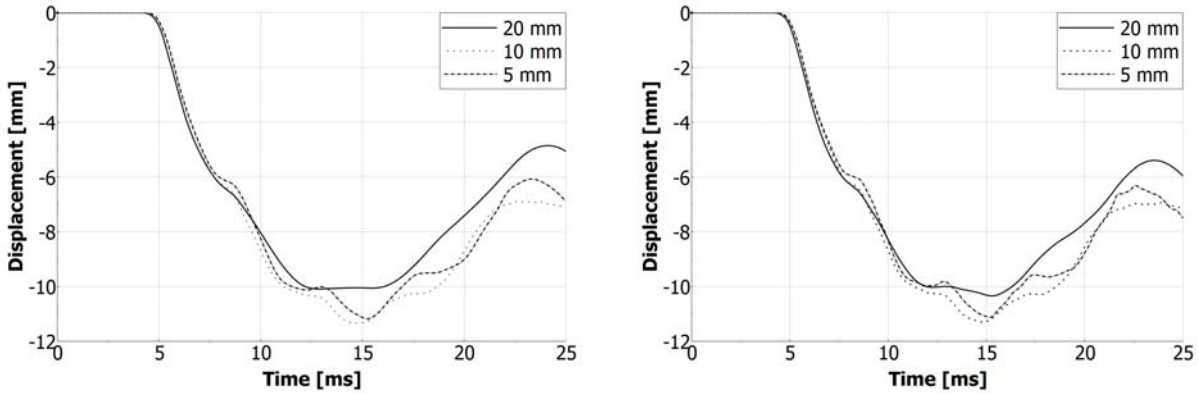

(a) *CDPM2-Bilinear.* (b) *CDPM2-Linear.*

Figure 8.2.3: *Mesh convergence study on CDPM2-Bilinear and CDPM2-Linear.*

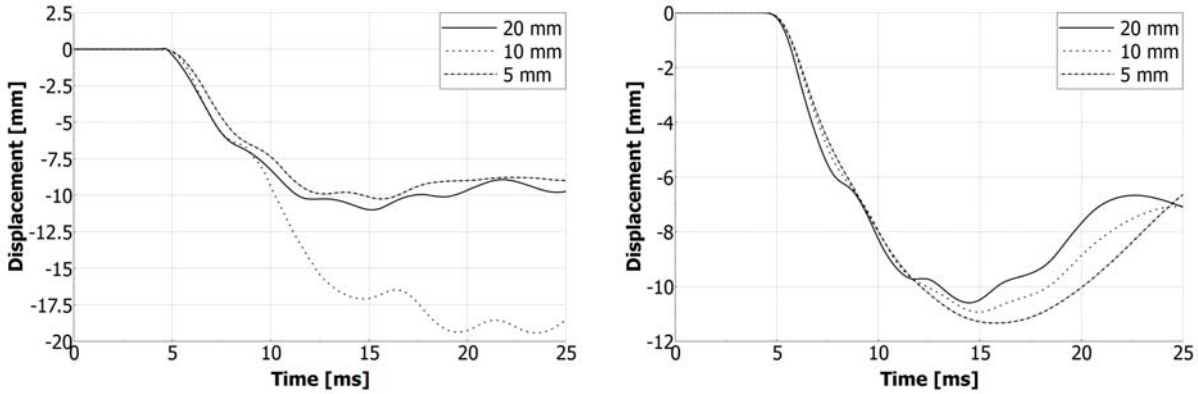

(a) *CSCM* (b) *Winfrith*

Figure 8.2.4: *Mesh convergence study on CSCM and Winfrith.*

During the convergence study each analysis were clocked in order to evaluate the computational efficiency of the material models. Those values are tabled in Table 8.2.1 along with a numerical summarization of the convergence study.

Table 8.2.1: *Results from mesh convergence analysis, it displays the maximum displacement. The diffecrence in displacement between the different mesh sizes and to the experiment. Total tun time and increase in run time between the different mesh sizes.*

	Disp.	Diff. mesh	Diff. to experiment	Run time	Incr. in run time
CDPM2 – Bilinear	[mm]	[%]	[%]	[s]	[-]
20 mm	−10.09	–	−10.31	2137	–
10 mm	−11.34	11.02	0.8	3484	1.6
5 mm	−11.18	−1.43	−0.62	35838	10.3
CDPM2 – Linear	[mm]	[%]	[%]	[s]	[-]
20 mm	−10.34	–	−8.09	2026	–
10 mm	−11.3	8.5	0.44	3486	1.7
5 mm	−11.18	−1.53	−1.07	35838	10.3
CSCM	[mm]	[%]	[%]	[s]	[-]
20 mm	−19.43	–	72.71	612	–
10 mm	−10.89	−75.42	−3.2	1994	3.3
5 mm	−10.27	−6.04	−8.71	18369	9.2
Winfrith	[mm]	[%]	[%]	[s]	[-]
20 mm	−10.59	–	−5.87	1784	–
10 mm	−10.94	−3.2	−2.76	2118	1.2
5 mm	−11.34	−3.53	−0.80	24658	11.6

8.2.2 Hourglass sensitivity

In this section the models sensitivity towards hourglass calibration is tested. The choice of hourglass type can make a significant difference in the solution when using underintegrated solid elements and large deformations can be expected. The hourglass sensitivity test is made by running all material models each with two different HG-types, namely HG-type 1 and HG-type 6. HG-type 1 is set as default in LS-DYNA. It is viscosity based, cheap to use but generally not the most effective choice. HG-type 6 is strongly recommended (LS-DYNA Support, 2015) to be invoked in all cases when underintegrated solid elements are used in implicit simulations. Reference is made to Chapter 6 for an explanation of hourglass effects.

Deflections at midspan are measured in order to see how the choice of HG-type affects the beam response during impact. In addition, during each analysis, the internal energy of the beam is logged as well as the hourglass energy. A good hourglass calibration should provide an hourglass energy less than ten percent of the internal energy of the beam (LS-DYNA Support, 2015).

As was the case for the mesh convergence study, the applied dynamic load consists of the drop-weight being dropped from a height of 0.3 m. Also, based on the convergence study above, a mesh size of 10 mm is used during the test. Figure 8.2.5 to Figure 8.2.8 displays differences with regard to midspan deflections and hourglass energy for each material model.

The midspan maximum deflections for different material models and HG-types as well as the differences in hourglass energies are summarized in Table 8.2.2.

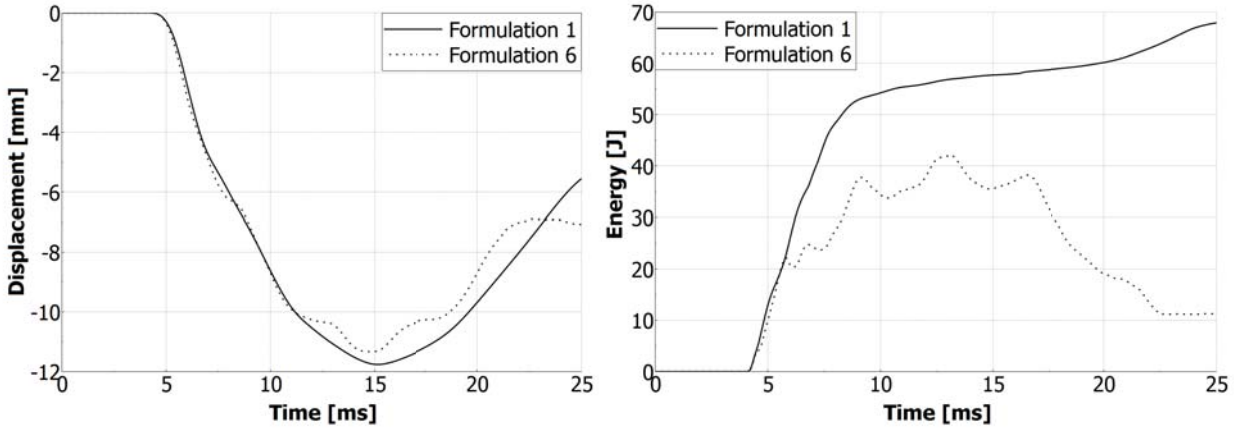

(a) *Displacements with HG-type 1 and HG-type 6 for CDPM2-Bilinear.*

(b) *Hourglass energy wit HG-type 1 and HG-type 6 for CDPM2-Bilinear.*

Figure 8.2.5: *Hourglass influence on CDPM2-Bilinear.*

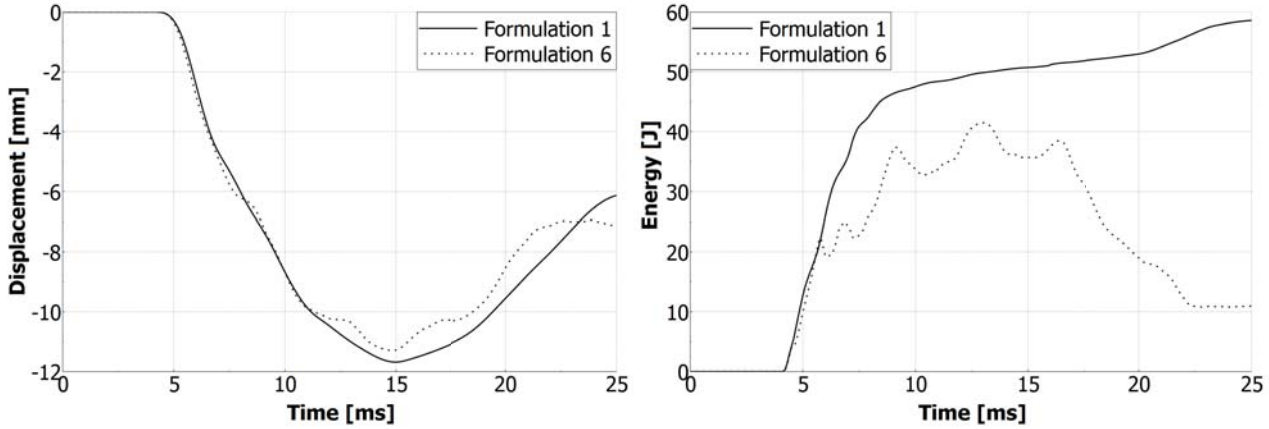

(a) *Displacements with HG-type 1 and HG-type 6 for CDPM2-Linear.*

(b) *Hourglass energy with HG-type 1 and HG-type 6 for CDPM2-Linear.*

Figure 8.2.6: *Hourglass influence on CDPM2-Linear.*

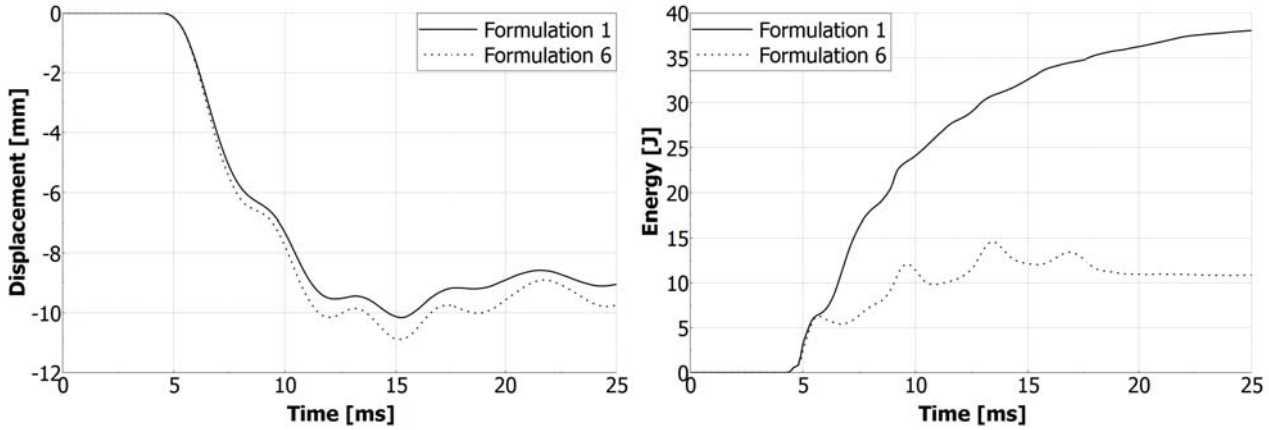

(a) *Displacements with HG-type 1 and HG-type 6 for CSCM.* (b) *Hourglass energy with HG-type 1 and HG-type 6 for CSCM.*

Figure 8.2.7: *Hourglass influence on CSCM.*

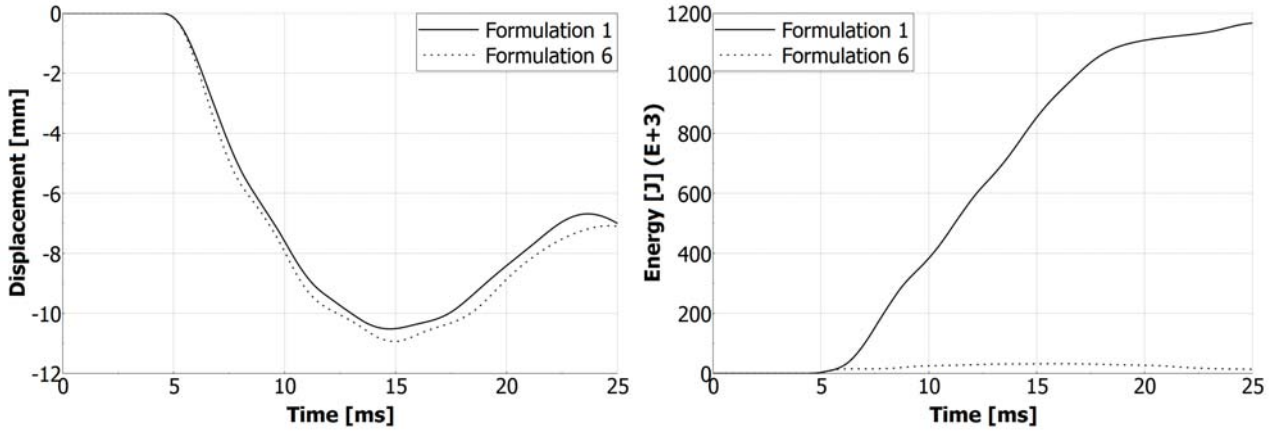

(a) *Displacements with HG-type 1 and HG-type 6 for Winfrith.* (b) *Hourglass energy with HG-type 1 and HG-type 6 for Winfrith.*

Figure 8.2.8: *Hourglass influence on Winfrith.*

Table 8.2.2: *Results from the hourglass analysis. Where the maximum displacement and difference to experiment is displayed. The difference between the internal energy and hourglassing energy is also displayed.*

	Disp.	Diff. to experiment	Internal energy	HG-energy	Diff. in energy
$CDPM2-Bilinear$	[mm]	[%]	[J]	[J]	[%]
HG-1	−11.76	4.53	873	67.89	7.78
HG-6	−11.34	0.8	916.3	11.29	1.23
$CDPM2-Linear$	[mm]	[%]	[J]	[J]	[%]
HG-1	−11.68	3.82	921	58	6.30
HG-6	−11.3	0.44	923	10.88	1.18
CSCM	[mm]	[%]	[J]	[J]	[%]
HG-1	−10.16	−9.69	1043	37.96	3.64
HG-6	−10.89	−3.2	1050	10.85	1.03
$Winfrith$	[mm]	[%]	[J]	[J]	[%]
HG-1	−10.52	−6.45	−209	1162	555.98
HG-6	−10.94	−2.76	−147.5	14.43	9.78

8.2.3 Comparison towards experimental results

The FE-model for Beam Case I is once again used to run analyses with the different material models. A comparison is made with the experimental test results with regard to deflections at midspan and overall crack patterns. The mesh size used is 10 mm and the drop-weight is dropped from the heights 0.3 m and 1.2 m. In the following sections the analysis results for each material model is displayed.

CDPM2-Bilinear

Figure 8.2.9 displays the maximum midspan deflection during impact when the drop-weight is dropped from the heights 0.3 m and 1.2 m respectively. Figure 8.2.10 shows the corresponding crack patterns where a damage parameter equal to one indicates a fully developed crack according to the theory behind CDPM2.

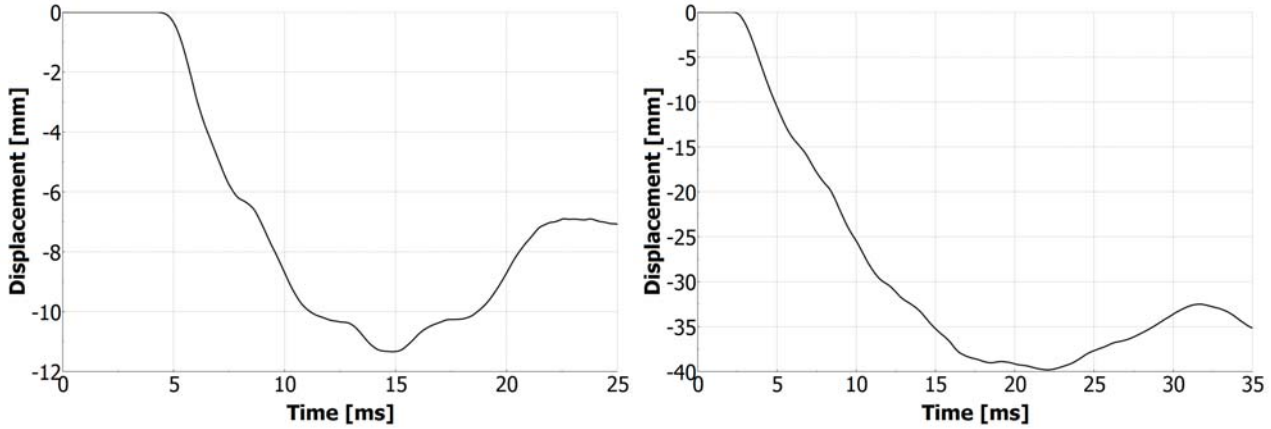

(a) *CDPM2-Bilinear with a drop-height of* 0.3 *m.* (b) *CDPM2-Bilinear with a drop-height of* 1.2 *m.*

Figure 8.2.9: *Displacement-time history for CDPM2-Bilinear.*

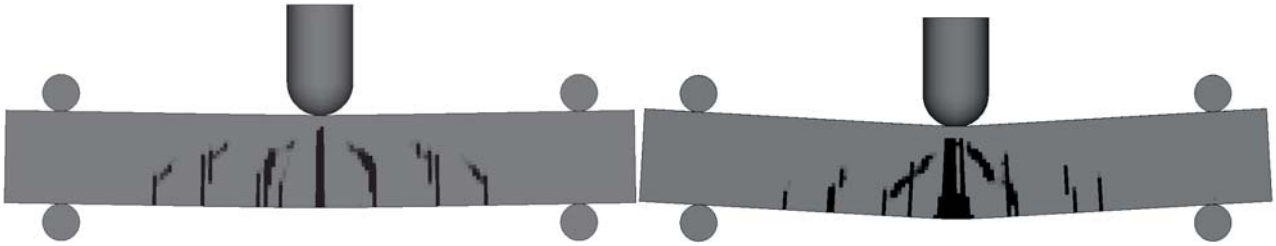

(a) *CDPM2-Bilinear with a drop-height of* 0.3 *m.* (b) *CDPM2-Bilinear with a drop-height of* 1.2 *m.*

Figure 8.2.10: *Crack patterns for CDPM2-Bilinear.*

Table 8.2.3 summarizes the maximum midspan deflections according to the FE-analyses and compares them to the experimental data presented in Figure 8.2.2.

Table 8.2.3: *Results from the numerical analysis with CDPM2-Bilinear compared to results from the experiment at the drop-heights 0.3 m and 1.2 m.*

Drop Height [m]	Midspan deflection [mm]	Experiment deflection [mm]	Difference [%]
0.3 m	−11.34	−11.25	0.8
1.2 m	−39.81	−36.60	8.06

CDPM2-Linear

Figure 8.2.11 displays the maximum midspan deflection during impact when the drop-weight is dropped from the heights 0.3 m and 1.2 m respectively. Figure 8.2.12 shows the corresponding crack patterns.

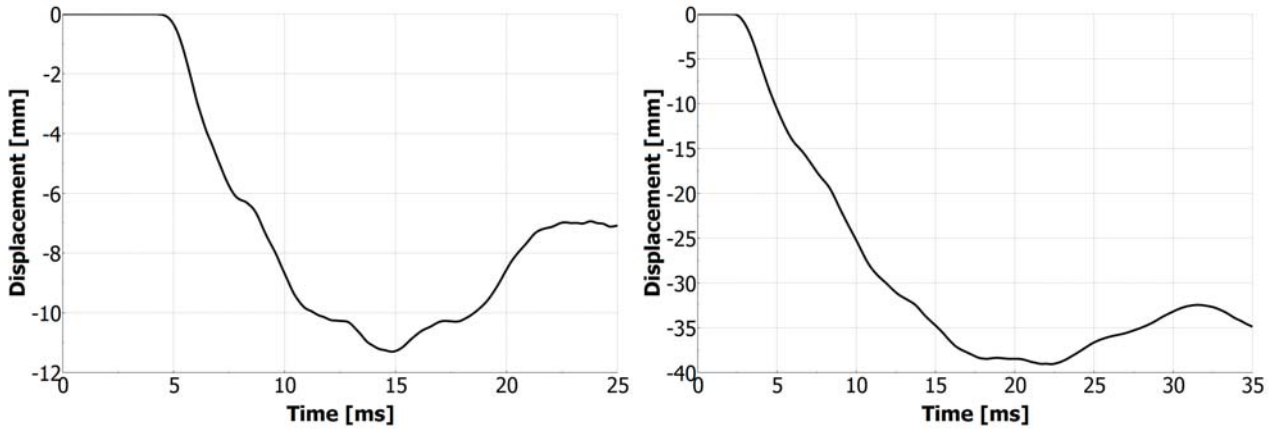

(a) *CDPM2-Linear with a drop-height of* 0.3 *m.* (b) *CDPM2-Linear with a drop-height of* 1.2 *m.*

Figure 8.2.11: *Displacement-time history for CDPM2-Linear.*

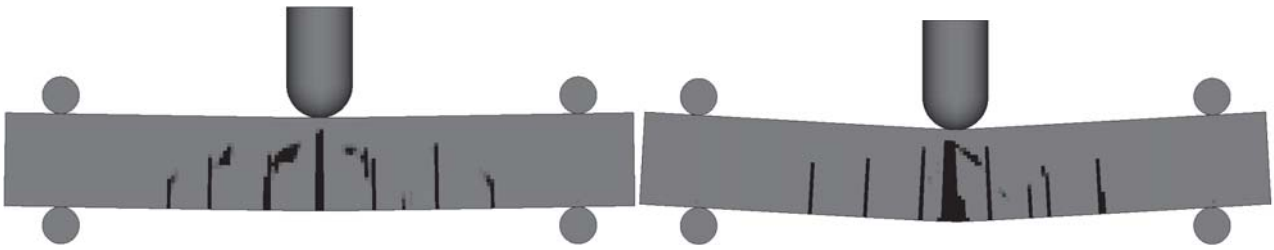

(a) *CDPM2-Linear with a drop-height of* 0.3 *m.* (b) *CDPM2-Linear with a drop-height of* 1.2 *m.*

Figure 8.2.12: *Crack patterns for CDPM2-Linear.*

Table 8.2.4 summarizes the maximum midspan deflections according to the FE-analyses and compares them to the experimental data presented in Figure 8.2.2.

Table 8.2.4: *Results from the numerical analysis with CDPM2-Linear compared to results from the experiment at the drop-heights 0.3 m and 1.2 m.*

Drop Height [m]	Midspan deflection [mm]	Experiment deflection [mm]	Difference [%]
0.3 m	−11.30	−11.25	0.44
1.2 m	−39.06	−36.60	6.3

CSCM

Figure 8.2.13 displays the maximum midspan deflection during impact when the drop-weight is dropped from the heights 0.3 m and 1.2 m respectively. Figure 8.2.14 shows the corresponding crack patterns.

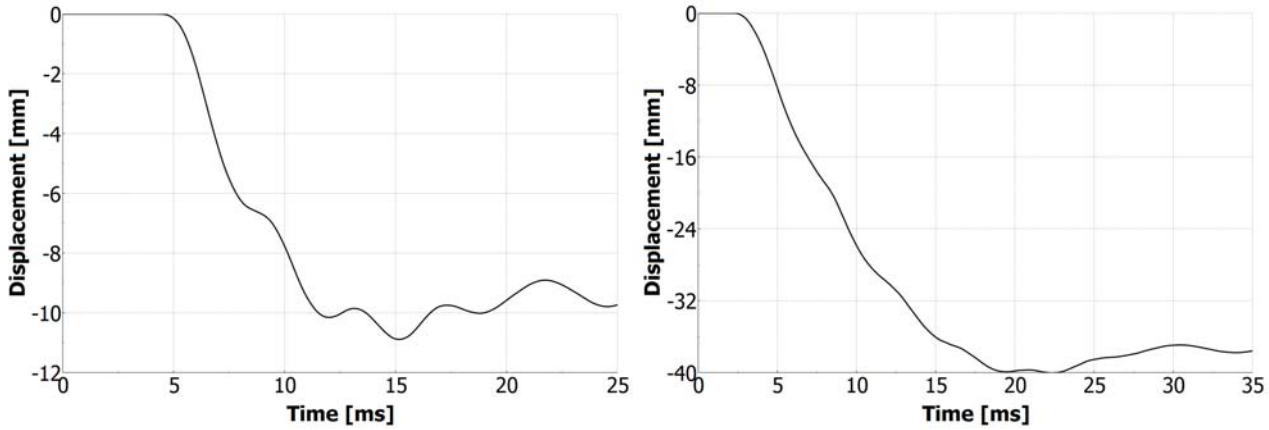

(a) *CSCM with a drop-height of* 0.3 *m.* (b) *CSCM with a drop-height of* 1.2 *m.*

Figure 8.2.13: *Displacement-time history for CSCM.*

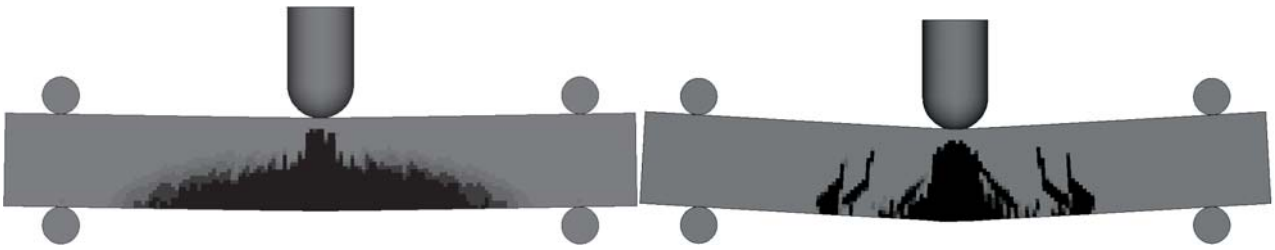

(a) *CSCM with a drop-height of* 0.3 *m.* (b) *CSCM with a drop-height of* 1.2 *m.*

Figure 8.2.14: *Crack patterns for CSCM.*

Table 8.2.5 summarizes the maximum midspan deflections according to the FE-analyses and compares them to the experimental data presented in Figure 8.2.2.

Table 8.2.5: *Results from the numerical analysis with CSCM compared to results from the experiment for the drop-heights 0.3 m and 1.2 m.*

Drop Height [m]	Midspan deflection [mm]	Experiment deflection [mm]	Difference [%]
0.3 m	−10.89	−11.25	−3.3
1.2 m	−40.03	−36.60	8.56

Winfrith

Figure 8.2.15 displays the maximum midspan deflection during impact when the drop-weight is dropped from the heights 0.3 m and 1.2 m respectively. Figure 8.2.16 shows the corresponding crack patterns.

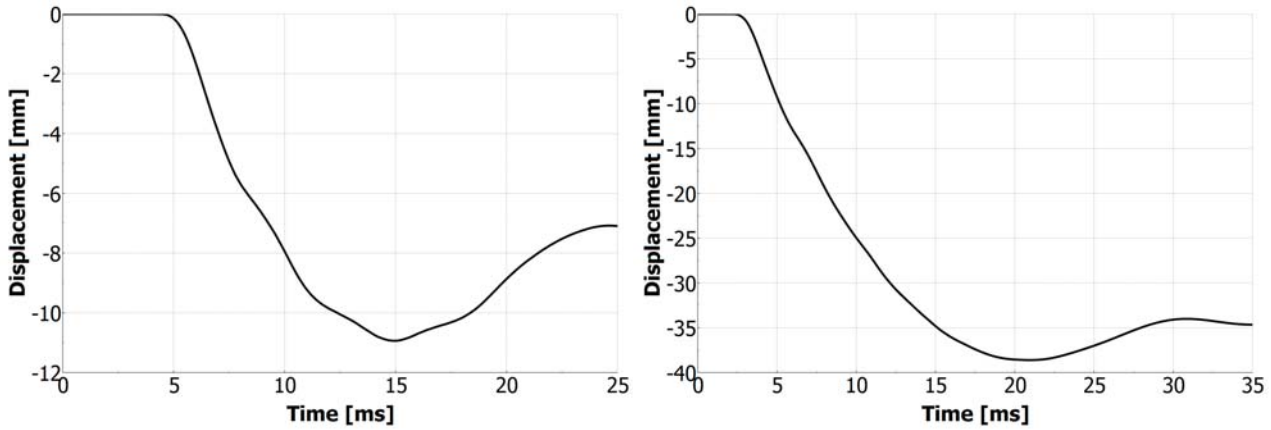

(a) *Winfrith with a drop-height of* 0.3 *m.* (b) *Winfrith with a drop-height of* 1.2 *m.*

Figure 8.2.15: *Displacement-time history for Winfrith.*

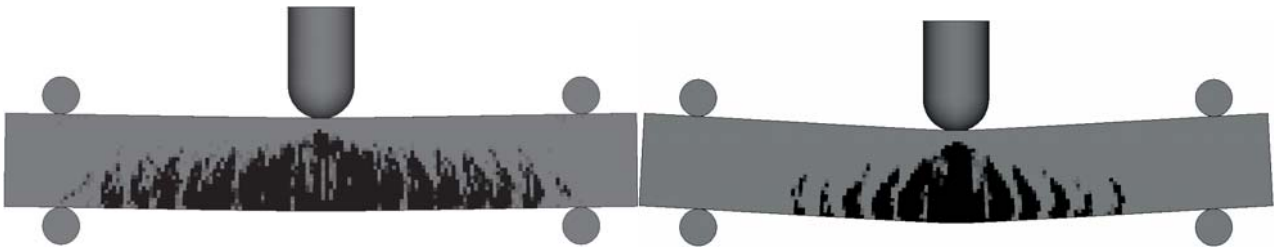

(a) *Winfrith with a drop-height of* 0.3 *m.* (b) *Winfrith with a drop-height of* 1.2 *m.*

Figure 8.2.16: *Crack patterns for Winfrith.*

Table 8.2.6 summarizes the maximum midspan deflections according to the FE-analyses and compares them to the experimental data presented in Figure 8.2.2.

Table 8.2.6: *Results from the numerical analysis with CSCM compared to results from the experiment for the drop-heights 0.3 m and 1.2 m.*

Drop Height [m]	Midspan deflection [mm]	Experiment deflection [mm]	Difference [%]
0.3 m	−10.94	−11.25	−2.83
1.2 m	−38.6	−36.60	5.18

8.3 Discussion regarding performance of the material models

In this section the material models are discussed with regard to mesh convergence, efficiency, hourglass sensitivity, correlations with experimental results, suitability according to theory and how easy they are to use.

8.3.1 CDPM2-Bilinear

Figure 8.1.2 display the static structural behaviour of the beam when using the CDPM2-Bilinear. A stiff behaviour can be seen up until the cracking load of 18 kN, followed by a stiffness reduction and a complete failure at a load of 99 kN. In Table 8.1.1 these values can be seen correspond approximately with the hand-calculated values used in the verification of Beam Case I in Chapter 7. With a verified static response the remainder of this section will treat the material model with regard to its dynamic performance.

Mesh convergence and computational efficiency

As can be seen in Figure 8.2.3 the maximum midspan deflection seem to converge towards a stable solution as the mesh is refined. Moreover this stabilization occurs around a displacement that almost exactly corresponds to the experimental result. A noteworthy observation is that the 20 mm mesh reaches a peak deflection and stays there over an extended time of about 4 ms. The reason behind this could be that the last impact impulse from the drop-weight occurs at the exact same time as the beam wants do deflect upwards. This results in a short period during which the downward impact is absorbed by the desired upward deflection of the beam, hence a short period of "equilibrium" arises that lasts until the impulse is absorbed and the beam can start to deflect upwards. Numerical values for the mesh convergence study are tabulated in Table 8.2.1 it can be seen that the gain from using 5 mm elements is small and that the model is the most time consuming to use.

Hourglass sensitivity

Figure 8.2.5a shows the maximum midspan deflection and how it is affected by the choice of HG-type. In Figure 8.2.5b the hourglass energies are logged during the impact phase. Those figures are coupled to Table 8.2.2 where, except numerical values from the graphs, also the value for the internal energy of the beam is displayed. The values in the table are taken from the time step when the maximum displacement occurs. An increased ratio between hourglass energy/internal energy should according to theory result in a more unreliable solution. However, in this case, the hourglass energy lies below the ten percent limit and therefore should not affect the solution notably.

Comparison to the experimental data

Figure 8.2.9 displays that a good correlation between the FE-simulations and the experimental data is achieved with regard to the maximum midspan deflections. Those values are tabled and compared in Table 8.2.3. Further, in Figure 8.1.3, the crack patterns according to the FE-model indicate a reasonable pattern although the amount of fully developed cracks seems to be less than what they are in the real experiment. The severity of the damage is however significantly larger in the simulations when the drop-weight is dropped from 1.2 m. This is reasonable and demonstrates that the material model is capable of showing an increase in damage.

Evaluation of CDPM2-Bilinear

Overall the simulations performed with CDPM2-Bilinear displayed good behaviour with a distinct crack pattern and good correlation between experimental and analytical results. The combined damage and plasticity behaviour is favourable when modeling concrete behaviour. Figure 6.1.6 show that the triaxial behaviour in the model display the best behaviour compared to the other models in this report. The model only need six input parameters to be defined and calculated by the user, while the remaining parameters has default values that can be used. This makes it easy to use while still retaining control over the material. It did however experience some technical difficulties as for example simulations suddenly failing and with some LS-DYNA binaries exhibiting weird behaviour, for example giving unreasonable results or simply not functioning at all.

8.3.2 CDPM2-Linear

In Figure 8.1.1 and Figure 8.1.2 the structural behaviour of the beam while using the CDPM2-Linear can be seen. The beam behaves according to expectations with a stiff behaviour up until the cracking load of about 20 kN, followed by a less stiff response until it finally fails at a load of about 100 kN. The cracking load as well as the failure load correspond relatively well to the hand calculated values used in the verification of Beam Case I in Chapter 7. With a verified static response the remainder of this section will treat the material model with regard to its dynamic performance.

Mesh convergence and computational efficiency

Figure 8.2.3 displays a convergence towards a stable solution as the mesh is refined. Moreover, the stabilization occurs around a displacement which is almost identical to the experimental result. Numerical values for the mesh convergence study are tabulated in Table 8.2.1 and it displays values very similar to CDPM2-Bilinear which was expected.

Hourglass sensitivity

Figure 8.2.6 shows the maximum midspan deflection and its dependency on the choice of HG-type and the hourglass energies are logged during the impact phase. Further, in Table 8.2.2, numerical values from the figures are listed and complemented with the internal energy of the beam. The tabulated values are taken from the time step when the maximum displacement occurs. As was the case for the CDPM2-Bilinear the hourglass energy lies well within the ten percent limit and hence it should not affect the reliability of the solution.

Comparison to experimental data

Figure 8.2.11 shows results that are very similar to the corresponding results for the CDPM2-Bilinear. They display a good correlation to the experimental data with regard to the maximum midspan displacements as well as the crack patterns. However, the CDPM2-Linear shows a somewhat more developed crack pattern where the cracks have propagated further in the beam than what the CDPM2-Bilinear does. But still the FE-model seems to underestimate the amount of fully developed cracks when compared to the experimental results. See Table 8.2.4 for a numerical summary of the graphical data in the figures.

Evaluation of CDPM2-Linear

The CDPM2-Linear behaved almost exactly as its bilinear version which was expected. It showed the same correlation with experiment and analytical results and experienced the same technical difficulties as CDPM2-Bilinear.

8.3.3 CSCM

The structural behaviour of the beam when using the CSCM as material model can be seen in Figure 8.1.1 and Figure 8.1.2. It displays a behaviour similar to the CDPM2-models where a defined cracking of the beam occur for a load of about 20 kN, followed by a stiffness reduction and a complete failure at a load of about 100 kN. These values correspond approximately with the hand calculated values used in the verification of Beam Case I in Chapter 7. With a verified static response the remainder of this section will treat the material model with regard to its dynamic performance.

Mesh convergence and computational efficiency

The mesh convergence study for the CSCM can be seen in Figure 8.2.4a. A convergence towards a stable solution is indicated; however this stabilization seems to be at a somewhat lower deflection compared to the experimental results. The reason for this is that the CSCM, as mentioned in Chapter 6, automatically generates all material properties based on the compressive strength of the material. Hence it has been observed that the tensile strength of the concrete material used in the mesh convergence study is slightly greater than the tensile strength of the other material models in this particular study.

It is notable how the 20 mm mesh seems to be unstable since it fails badly at coming even close to the deflection of the experimental results.

Numerical values for the mesh convergence study are tabulated in Table 8.2.1 and the simulation times for the different mesh sizes are tabulated here as well. The computational efficiency of the CSCM is good compared to the other material models as it performed approximately 50 percent faster than the CDPM-models and about 25 percent faster than the Winfrith-model.

Hourglass sensitivity

In Figure 8.2.7a the maximum midspan deflection and its dependency on the choice of HG-type is shown. Figure 8.2.7b demonstrates the logged hourglass energies during the impact phase. Numerical values from the figures along with the internal energy of the beam are displayed in Table 8.2.2. This information indicates that hourglass effects are not very pronounced.

Comparison to the experimental data

Figure 8.2.13 displays a good correlation to the experimental data with regard to maximum midspan deflections. However, the crack patterns presented in Figure 8.2.14 requires some comments as it at first sight do not seem to simulate the experimental results very well. As mentioned in Section 8.1 the crack pattern in this case is visualized by means of strain concentrations instead of a damage parameter. This is due to problems with visualization of the damage parameter in CSCM when using the post-processor META. It can be seen that the cracks are more smeared in the dynamic case,

as compared to the static crack pattern for CSCM in Figure 8.1.5. This is true for both the 0.3 m drop-height as well as for the 1.2 m drop-height, however in the latter a failure can be seen with some clear cracks occurring. See Table 8.2.5 for a numerical summary of the graphical data in the figures.

Evaluation of CSCM

The behaviour of CSCM showed good correlation with experimental and analytical results, CDPM2 showed only slightly better correlation. The crack pattern did however not really function as expected when modelling a full beam. In the cube test the damage parameter accumulated damage from zero to one once the ultimate tensile strength was reached. In the beams the values started accumulating but then after a while they started to fluctuate down to zero at seemingly random. Because of this the decision was made to plot all cracks using strains instead damage parameters. It can however be seen that the cracks in the static cases exhibit a good behaviour for CSCM. Despite that CSCM displayed a smeared crack pattern when subjected to dynamic loads. This could be due to its failure to accurately calculate confinement pressure as can be seen in Figure 6.1.9. The model is very easy to use with only three input parameters needed, on the other hand this leads to a loss in control since neither tensile strength or Young's modulus can be defined by the user. It was however deemed to be a good and efficient model.

8.3.4 Winfrith

In Figure 8.1.1 and Figure 8.1.2 the structural behaviour of the beam when using the Winfrith-model is shown. The model indicates a strange behaviour when compared to the other material models as it cracks at a load of about 26 kN. Moreover, after cracking, it seems to lose all stiffness as the deflection rises dramatically for no further increase of the load. The beam indicates a deviant structural response up until a load of about 60 kN where it once again joins in with the other material models with regard to structural behaviour. An explanation could be in the way Winfrith handles crack initiations during this particular load case. It was observed during the simulation that after the first crack occurred no more cracks were initiated for a period of time, instead the first crack was successively opened as the load was increased. This behaviour lasted up until a load of about 60 kN, which happens to be when the beam response once again joins the beam responses of the other material models according to Figure 8.1.2. It indicates that the model fails to handle the interaction between the reinforcement and the concrete for a period of time. This is strange since it manages to obtain that interaction when the load has increased well above the cracking load. The inability to capture a reasonable structural response during a simple static load case gives reasons to question the reliability of the model when accurate analyses are required.

Mesh convergence and computational efficiency

Figure 8.2.4b displays a good mesh convergence as the mesh is refined. Moreover stabilization seems to occur around a displacement that is almost identical to the experimental test result. The mesh convergence study is summarized with numerical values in Table 8.2.1 and it can be seen that the convergence for 10 mm elements is good and that Winfrith is an efficient model to use.

Hourglass sensitivity

Figure 8.2.8a demonstrates the maximum midspan deflection and how it is affected by the choice of HG-type. In Figure 8.2.8b the corresponding hourglass energies are logged during the impact phase.

Numerical data from the figures are tabulated in Table 8.2.2 along with the measured internal energy of the beam. The values in the table are taken from the time step when the maximum displacement occurs. According to the test the Winfrith model is the only among the material models that displays a significant amount of hourglass energy compared to the amount of internal energy (when using HG-type 1). Based on theory this should make the FE-solution unreliable. However, as shown in Figure 8.2.8a and inconsistently to the theory, the solution is basically unaffected by the choice of HG-type with regard to midspan deflections. The reason could be that the choice of HG-type affects other parameters such as stresses and strains to a larger extent than it does affect deflections. This is not unreasonable since hourglass effects originate from zero stress- and zero strains energies. See Chapter 6 for a more detailed explanation of hourglass effects.

Comparison to experimental data

Figure 8.2.15 shows a midspan displacement that corresponds well to the experimental results. Regarding the crack pattern, displayed in Figure 8.2.16, it can be seen that it exhibits a smeared behaviour and clear cracks are hard to make out for the 0.3 m drop-height. In the 1.2 m case the cracks are more pronounced but still to wide to be a depiction of a realistic crack pattern.

Evaluation of Winfrith

The Winfrith model is the simplest model evaluated in this report as it uses a basic plasticity model, do not account for shear dilation and is incapable of modeling triaxial pressures seen in Figure 6.1.12. In spite of this it showed good correlation with both experimental and analytical results, CSCM and CDPM2 showed slightly better results. As explain in Section 6.1.3 the damage parameter only has four different values. Because of this the crack patterns were difficult to interpret. In the static analysis one sudden crack opened as soon at the tensile strength of the concrete had been reached, which can be observed as the sudden increase in deformations in the load-displacement curve for 40 kN in Figure 8.1.1. During continued loading up until yielding some more smaller cracks occurred but still only one main crack. When subjected to dynamic loading it exhibited, like CSCM, a smeared crack pattern which again could be due to the inability to model confining pressures. It was easy to use only needing a few input parameters.

8.4 Decision on material model to use for remaining models

Based upon the evaluation of the material models CDPM2 is the one that would be preferable to continue using because of its superior cracking behaviour, good correlation with results and overall behaviour. However the prestressing method presented in Section 9.3.1 could not be combined with CDPM2 because of technical issues with the binaries available when writing this report. So instead CSCM was picked for continued use. Even thought it did not exhibit as good results it was deemed adequate for the simulations performed. The biggest problem being the crack pattern, but that was solved by using infinitesimal strain to show cracks.

9 Beam Case II- and III - Drop-weight analysis on a reinforced prestressed beam and an equivalent reinforced beam

In this chapter a prestressed beam is introduced as well as an equivalent reinforced beam, called Beam Case II and Beam Case III respectively. The reinforced beam is equivalent to the prestressed beam with regard to its capacity in the ultimate limit state. This equivalence is desirable to introduce in order to evaluate the effect of prestressing in a good way when the beams are loaded.

The beams will be subjected to both static and dynamic loads. In the static load case the load is applied as a point load in the middle of the span. The dynamic load is also applied at midspan by a drop-weight with an impact surface of 150 x 220 m^2 and a mass of 50 kg, dropped from 0.15 m, 1.0 m, 2.0 m and 3.0 m. Those drop-heights corresponds to the impact velocities 1.71 m/s, 4.43 m/s, 6.26 m/s and 7.67 m/s respectively. An illustration of the entire test set-up can be seen in Figure 9.1.

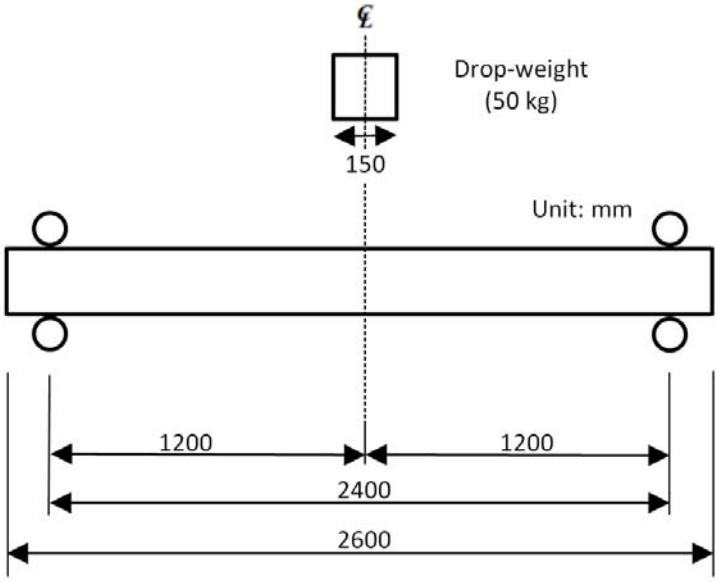

Figure 9.1: *Test set-up for Beam Case II and Beam Case III.*

9.1 Beam Case II - Reinforced- and prestressed beam

The schematics of the prestressed beam are showed in Figure 9.1.1. It has a total length of 2600 mm where the free span length is set to 2400 mm. The cross section of the beam is quadratic with a cross sectional area of 220 x 220 mm^2. Top- and bottom reinforcement is symmetrically placed consisting of two $\phi 12$ bars in each layer. All longitudinal reinforcement has a yield strength of 500 MPa. The prestressing is introduced by a straight prestressing wire placed with an eccentricity of 50 mm below the system line of the beam. It has a diameter of 13 mm, a yield strength of 1590 MPa and an ultimate capacity of 1860 MPa. The prestressing wire is anchored in rigid plates on both sides of the beam, 60 mm high and 120 mm broad, and the initial prestressing force is 164 kN. There is no strain compatibility between the prestressing wire and the surrounding concrete during the tensioning

phase. However, just before the external load application, the prestressing duct is grouted which means that a full bond is established between the prestressing wire and the surrounding concrete.

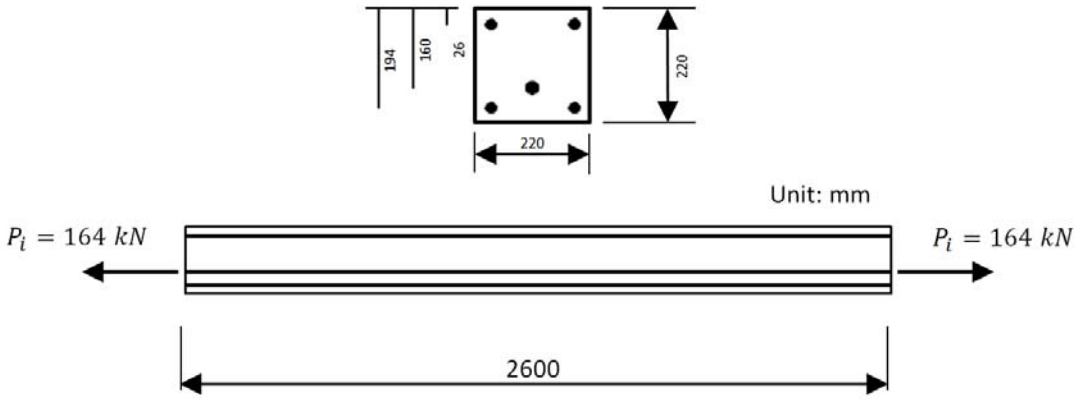

Figure 9.1.1: *Beam geometry and reinforcement arrangement for Beam Case II and Beam Case III.*

The beam geometry as well as the drop-weight data presented in Figure 9.1 and Figure 9.1.1 are summarized in Table 9.1.1 and Table 9.1.2 respectively.

Table 9.1.1: *Summarization of the beam geometry and reinforcement arrangement.*

Concretebeam	l_{span} [mm]	h [mm]	b [mm]
	2400	220	220
	d' [mm]	d_p [mm]	d [mm]
	26	160	194

Table 9.1.2: *Summarization of the drop-weight data.*

$Drop-weight$	m [kg]	$b_{fallweight}$ [mm]	$w_{fallweight}$ [mm]	$h_{fallweight}$
	400	150	90	386
	h_{drop1} [m]	h_{drop2} [m]	h_{drop3} [m]	h_{drop4} [m]
	0.15	1	2	3

9.2 Beam Case III - Equivalent reinforced beam

This beam is almost identical to the prestressed beam described above, with the only difference that the prestressing effect is taken away. The prestressing wire is replaced with a regular reinforcement bar with the same placement, diameter and yield strength as the prestressing wire.

9.3 Creation of the FE-models for Beam Case II- and III

The FE-modeling technique used to model reinforced concrete beams in LS-DYNA was described and verified in Chapter **??**. Further, in Chapter 8, an appropriate concrete material model was chosen to be used in the upcoming analyses. In this chapter the already verified modeling technique is used as a basis upon which the complexity of the FE-model is increased by introducing prestressing. The main modeling procedure of the prestressed beam is according to Chapter **??**. Only components that is added to the FE-model, such as prestressing, is explained in this chapter. An illustration of the complete model can be seen in Figure 9.3.1 showing a transparent solid beam with the reinforcement arrangement.

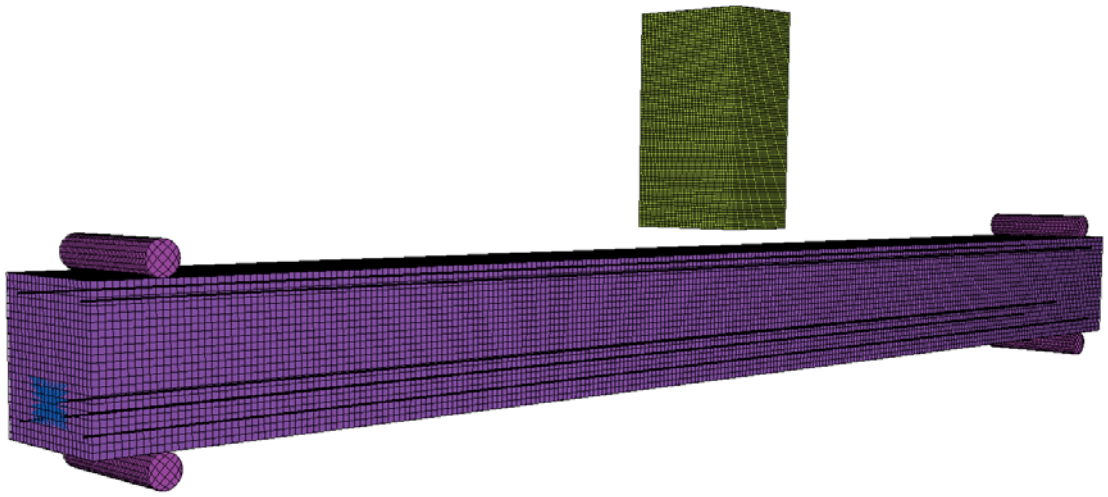

Figure 9.3.1: *Visualization of the complete prestressed concrete beam.*

The entire FE-model are described in AppendixB as a text input file. This is the file that are read by the LS-DYNA solver in order to execute the FE-calculation. Detailed numerical information about materials, elements, loads, contacts, control cards etc. can be found there. Material- and element properties are described in Chapter **??**.

9.3.1 Modeling of the prestressing effect

The desired type of prestressing in the FE-model was a post tensioning which was then grouted before any external load was applied. To achieve this effect the modeling was divided into four steps, each representing a step taken in real life when applying prestressing to a post-tensioned beam.

Stage I - Creating the prestressing duct

As a first step the prestressing duct was modeled. This was done by introducing a "guiding cable" along the desired location of the prestressing duct, which was a straight horizontal line in this case. The guiding cable was modeled with beam elements given the material type *MATNULL, which means that the duct will not contribute to any stiffness of the structure. In order to couple the prestressing duct to the surrounding concrete, a *CONSTRAINED-LAGRANGE-IN-SOLID contact was used, as was the case when coupling the regular reinforcement to the concrete. See Figure 9.3.2.

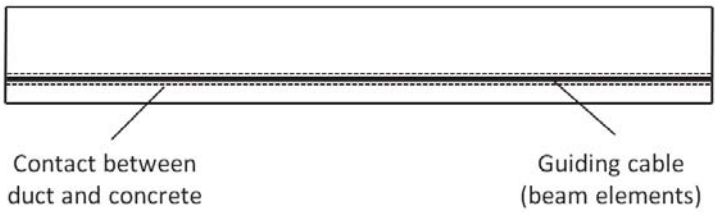

Figure 9.3.2: *The prestressing duct (beam elements) are coupled to the surrounding concrete (solid elements).*

Stage II - Placing of the prestressing wire into the duct

The prestressing wire was modeled with beam elements that was placed along the same line and with the same geometry as the guiding cable in the previous stage. Further, it was given the same material type as the regular reinforcement, *MAT-PLASTIC-KINEMATIC. In the next modeling step the prestressing wire was placed "inside" the prestressing duct. This was done by implementing the contact *CONTACT-GUIDED-CABLE-SET between the prestressing wire and the prestressing duct. The contact allows the wire to slide freely inside the duct while still providing pressure on the surrounding concrete when the wire is tensioned (e.g. when a parabolic prestressing wire is tensioned). The modeling procedure for stage II is illustrated in Figure 9.3.3. In order to achieve the free movement of the prestressing wire inside the duct, a part set ID (the beam elements representing the prestressing wire) and a node set ID (the nodes of the beam elements representing the guiding cable) must be defined in the contact card. This is so beam elements of the prestressing wire are allowed to slide between the nodes of the beam elements representing the guiding cable.

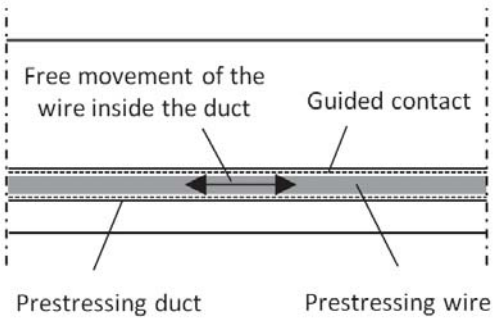

Figure 9.3.3: *The prestressing wire are allowed to move freely inside the duct.*

Stage III - Tensioning of the beam

The beam was tensioned from both ends. Anchoring plates was modelled at the beam ends by defining sets of nodal rigid bodies, i.e. nodes that together creates rigid surfaces. To achieve a tensioning effect the outermost beam elements of the prestressing wire was changed to the material type *MAT-ELASTIC-PLASTIC-THERMAL which is a thermo elastic material capable to deform when subjected to temperature gradients. The nodes of those thermal beam elements are at one side pasted together with one of the nodes of the anchoring plate and at the other side pasted together with the prestressing wire. The guiding cable must not be pasted to the tensioning element. An illustration showing the modeling of the first part of the tensioning procedure is presented in Figure 9.3.4.

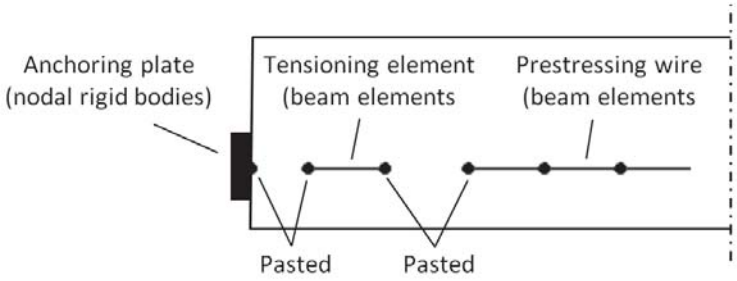

Figure 9.3.4: *The tensioning element is pasted to the prestressing wire and the anchoring plate.*

When the entire prestressing mechanism had been modelled a negative temperature load was applied on the nodes of the tensioning elements in order to give them a negative strain. This was done using the "Thermal variable" option in LS-DYNA. Since the tensioning elements was pasted to the anchoring plates as well as the prestressing wire it starts to pull in them, introducing a normal force into the concrete beam. See Figure 9.3.5.

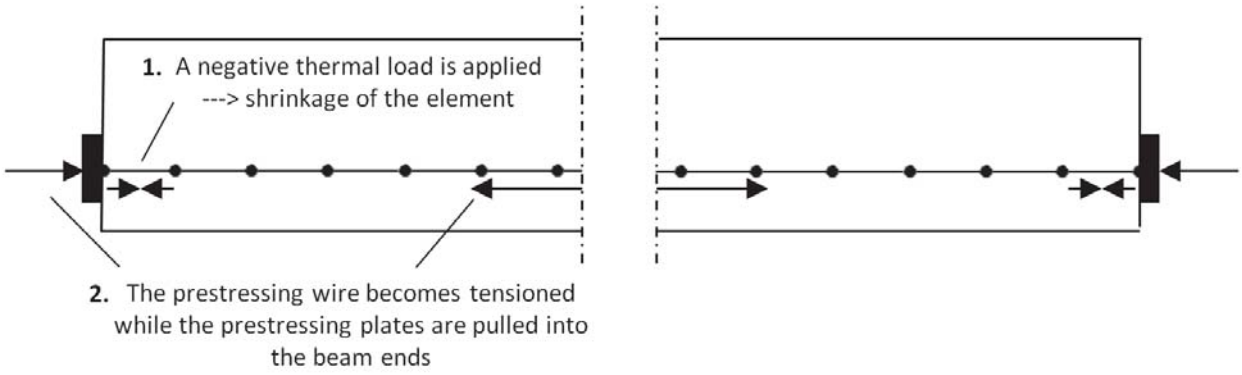

Figure 9.3.5: *Visualization of how a thermal load is applied in order to achieve a prestressing effect in the beam.*

Stage IV - Grouting of the prestressing duct

Post-tensioned structures are grouted soon after the tensioning phase. By doing so full strain compatibility between the prestressing steel and the surrounding concrete is achieved. In the FE-model the grouting was modeled by introducing a *CONSTRAINED-LAGRANGE-IN-SOLID contact between the prestressing steel and the surrounding concrete. The contact was not activated until the tensioning of the beam was complete. The postponed activation of the contact was controlled using the "Birth" option in the Lagrange contact card.

9.4 Creation of the FE-model - Beam Case III

Beam Case III is a regular reinforced beam. Hence the FE-modeling technique will not be explained here; instead reference is made to **??**. Beam geometries and longitudinal reinforcement arrangement is identical to Beam Case II with the only difference being that the prestressing wire is replaced by a reinforcement bar with the same yield strength as the prestressing steel.

9.5 Verification of the FE-models - Beam Case II- and III

A successful verification of Beam Case II- and III means that they are approved to be used as test beams when the prestressing effect is evaluated during dynamic loading in Chapter 10. The following verification is based on a static load case, were the beams are loaded until their ultimate capacities, as well as a dynamic load case, where comparisons is made to a SDOF-system. To further clarify the effect of prestressing the beams are verified alongside each other in the same sections. The means of verification is first introduced followed by the actual verification results.

9.5.1 Means of verification and verification results

The verification of Beam Case II- and III follows the same procedure as for Beam Case I. I.e. different contour plots of the models are first examined visually to see if the beams respond as can be expected. If so, further verifications are made by comparisons to hand calculations according to Eurocode.

Visual verification

Figure 9.5.1 shows the deflection of the beam as well as the stress distribution within the beam due to prestressing. The response is desirable as the beam curves upwards while it becomes compressed at the bottom side and tensioned at the top side. In Figure 9.5.2 the stress distributions in the beams are visualized just before cracking. Both beams shows stress distributions according to expectations, however, the applied load on the prestressed beam is greater than the load applied on the equivalent reinforced beam. This is noteworthy since it indicates that the modelled prestressing works as desired.

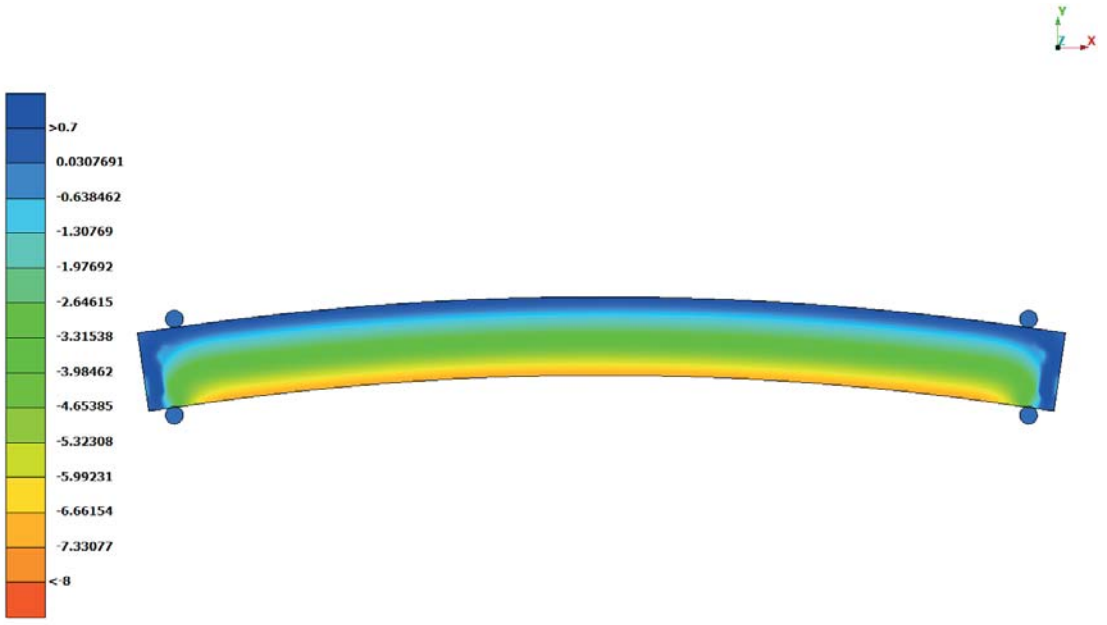

Figure 9.5.1: *Contour plot showing the Von Mises stress distribution as well as the upward deflection of the beam immediately after tensioning.*

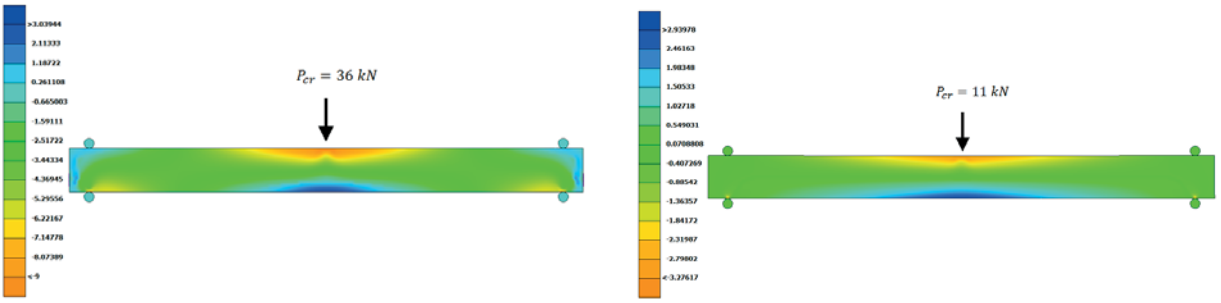

(a) *Prestressed beam.* (b) *Equivalent beam.*

Figure 9.5.2: *Contour plots showing the Von Mises stress distribution just before cracking for the prestressed beam as well as for the equivalent beam. Observe the different magnitudes of the cracking loads.*

Verification towards Eurocode

In Figure 9.5.3 the applied prestressing force is plotted against the midspan upward deflection of the beam during the tensioning phase. The FE-model displays an upward deflection of $u_{prestr.DYNA} = 0.87$ mm after complete tensioning, corresponding to a prestressing force of $P_i = 164$ kN. This deflection conforms well to the hand calculations which give a deflection of $u_{prestr.} = 0.90$ mm, see AppendixE.2. The tensioning phase is further verified by a comparison of sectional stresses. Stresses at five locations are compared; concrete stresses at top- and bottom side of the beam as well as steel stresses in all steel layers. See Figure 9.5.4. The compared numerical values between the FE-model and the hand calculations are displayed in Table 9.5.1. It should be noted that the ratios comparing the stress values for the "Concrete top side" and "Top reinforcement" displays large differences. This is however an effect due to the very small values that are compared. Reference is made to Appendix**??**app:beam2tens where the hand calculation procedure can be found.

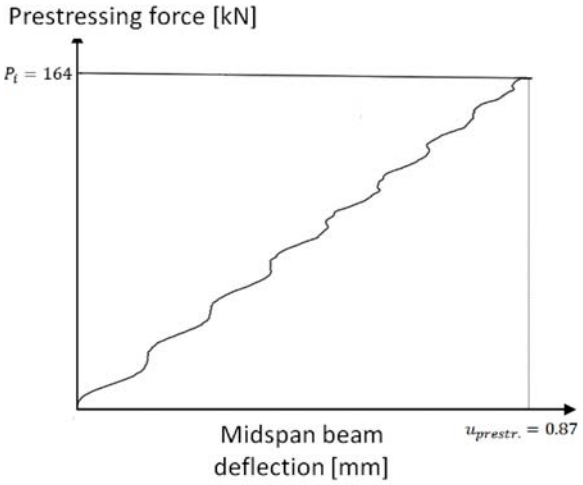

Figure 9.5.3: *The applied prestressing force plotted against the midspan upward deflection of the beam.*

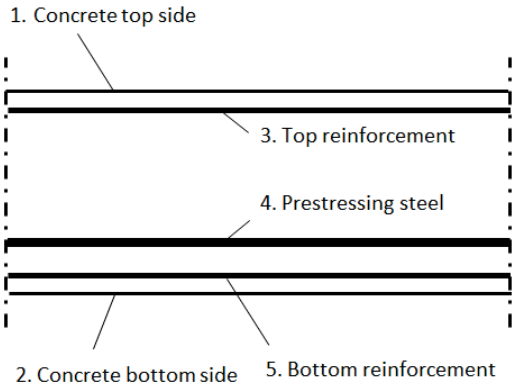

Figure 9.5.4: *Layers where stresses are compared between the FE-model and hand calculations immediately after tensioning of the beam.*

Table 9.5.1: *Comparison between FE-model results and hand calculated values according to Eurocode. The stresses are calculated at midspan immediately after tensioning.*

Beam Case II	FEM	Eurocode	Comparison
Concrete top side [MPa]	−0.750	0.820	0.521
Concrete bottom side [MPa]	−7.200	−7.250	1.007
Top reinforcement [MPa]	−0.200	0.070	0.259
Bottom reinforcement [MPa]	−43.50	−44.15	1.015
Prestressing steel [MPa]	1238	1203	0.9720

Figure 9.5.5 displays the load-deformation curves for the prestressed beam and the equivalent beam respectively. Both curves demonstrate structural behaviors in line to what can be expected. Points of interests with regard to the verification is marked in the figure as 1) being the cracking of the beams and 2) representing failure of the beams. Numerical values for the cracking load, deflection at cracking, ultimate capacity and deflection at failure is tabled in Table 9.5.2 and Table 9.5.3 where they are compared to corresponding values from the hand calculations for each beam. The FE-model results corresponds relatively well to the hand calculated values, however, the deflections just before failure should be taken with caution as they can vary significantly in between time steps. The hand calculations for the prestressed beam and and the equivalent beam can be seen in AppendixE.3 and AppendixE.4, respectively.

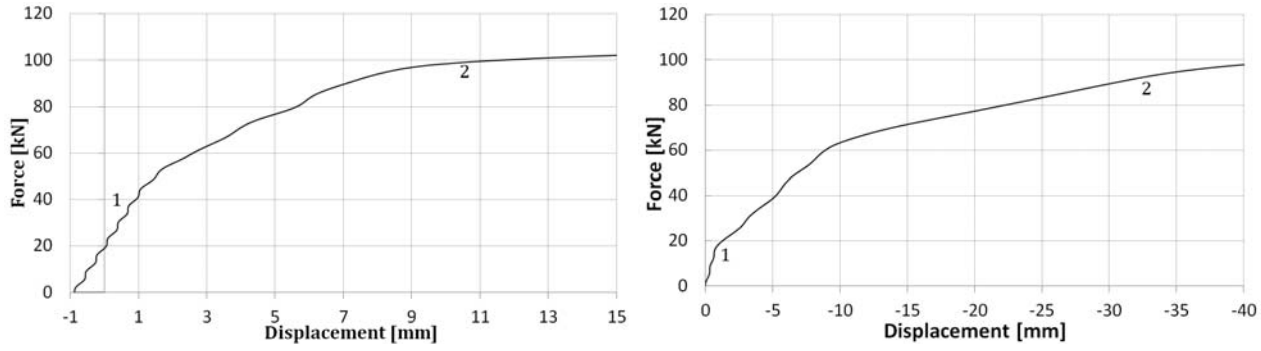

(a) *Prestressed beam.* (b) *Equivalent beam.*

Figure 9.5.5: *Load-displacement curves for the prestressed beam and the equivalent beam respectively. The scaling of the displacement-axis does not correlate inbetween the graphs. A reference is made to Table 9.5.2 and Table 9.5.3 for numerical values at point 1) and 2).*

Table 9.5.2: *Comparison between FE-results and hand calculations according to Eurocode for the prestressed beam, see figure Figure 9.5.5a.*

Compared parameter	FE-model	Eurocode	Comparison
P_{cr}[kN]	38.30	36.0	0.941
u_{cr}[mm]	0.776	0.659	0.849
P_{ult}[kN]	99.20	84.60	0.852
u_{ult}[mm]	10.62	12.04	1.13

Table 9.5.3: *Comparison between FE-results and hand calculations according to Eurocode for the equivalent beam, see figure* **??**.

Compared parameter	FE-model	Eurocode	Comparison
P_{cr}[kN]	11.4	11.0	0.962
u_{cr}[mm]	0.542	0.477	0.881
P_{ult}[kN]	93.5	84.6	0.904
u_{ult}[mm]	33.71	14.977	0.444

Verification of prestressing force

In Section 9.3.1 the method for achieving prestressing is explained. In the analysis described in this section a temperature difference of $= -5000°$C was applied, a case where $= -2500°$C was also examined to investigate the correlation between applied load and obtain prestressing force. The coefficient of thermal expansion was set to $\alpha = 0.0001$. The prestressing force was then calculated analytically and compared to the numerical value obtained in LS-DYNA. The results are summarised in Table 9.5.4. ε_w is the strain in one element of the prestressing wire and σ_p is the stress in the prestressing wire.

Table 9.5.4: *Correlation between applied temperature difference, strains and stress in the prestressing wire.*

		ε_p [-]	ε_w [-]	σ_p [MPa]
−5000				
	Analytically	−0.5	0.007813	1641
	Numerically	−0.4941	0.005894	1238
	Difference [%]	−1.18	−25.14	−24.56
−2500				
	Analytically	−0.25	0.003906	820
	Numerically	−0.2467	0.003308	695
	Difference [%]	−1.32	−15.31	−15.24

Dynamic verification

To get an analytical comparison for Beam Case II- and III were turned into equivalent SDOF systems, here the static cross section parameters calculated in AppendixE.3 and AppendixE.4 were used for both the equivalent beam and the prestressed beam. Because of the problem with calculating the transformation factor for stiffness, κ_k, when a normal force is present which is explained in Section **??**. The same transformation factors where used for both cases. The impulse was calculated to be $I = 221.5$ Ns and the impact obtained in the FE-analysis was used in MATLAB and calibrated, as little as possible, to obtain the deformations. Figure 9.5.6 show impacts on the equivalent beam and Figure 9.5.7 show the impacts on the prestressed beam.

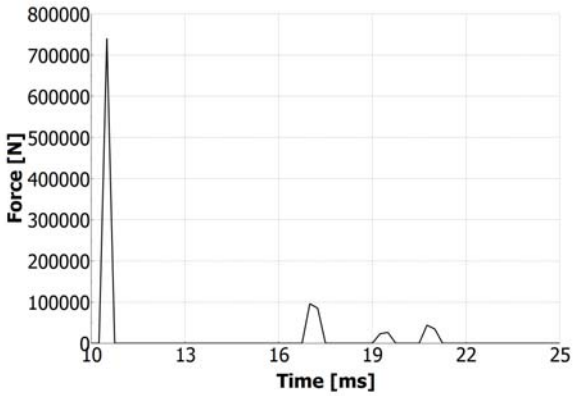

(a) *Impact force between drop-weight and concrete beam in LS-DYNA.*

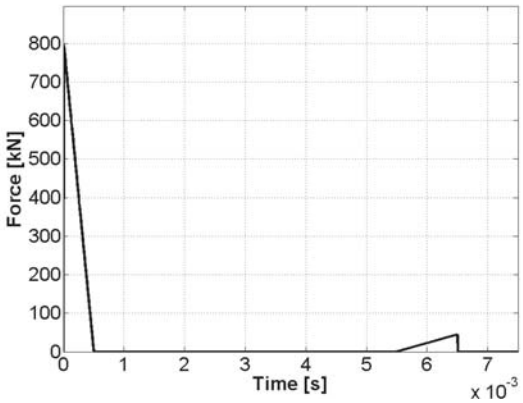

(b) *Calibrated impact force in SDOF system.*

Figure 9.5.6: *Impact force at a drop-height of 1 m.*

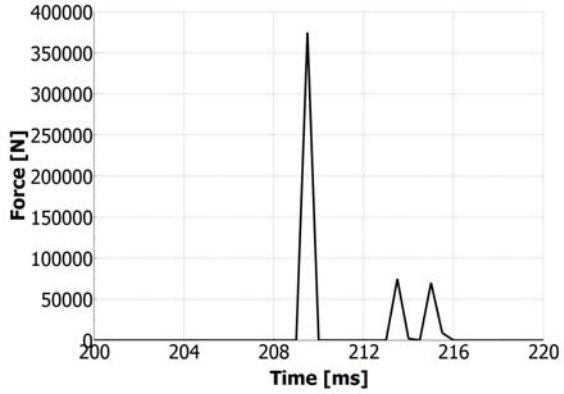

(a) *Impact force between drop-weight and concrete beam in LS-DYNA.*

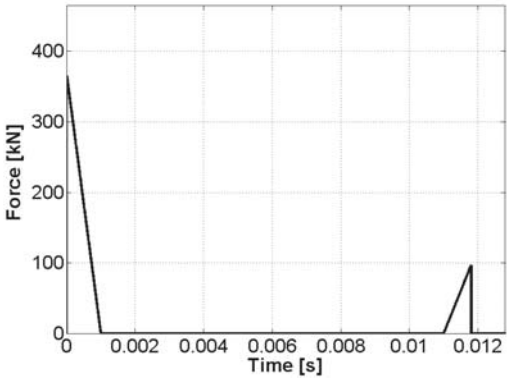

(b) *Calibrated impact force in SDOF system.*

Figure 9.5.7: *Impact force at a drop-height of 1 m.*

Here there are two clear peaks that correspond to the initial impulse from the drop-weight while the last peaks are the beam pushing away the drop-weight. The displacements can be seen in Figure 9.5.8 and Figure 9.5.9.

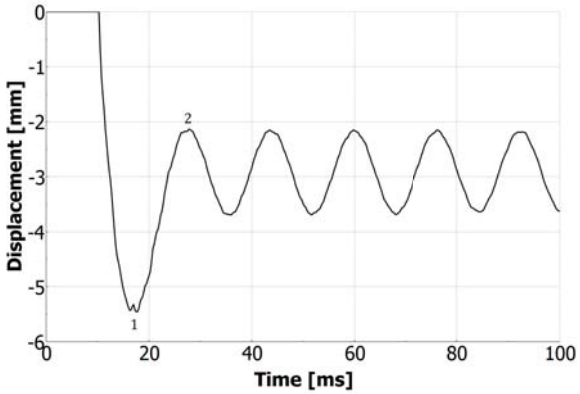

(a) *Displacement in LS-DYNA for the equivalent beam.*

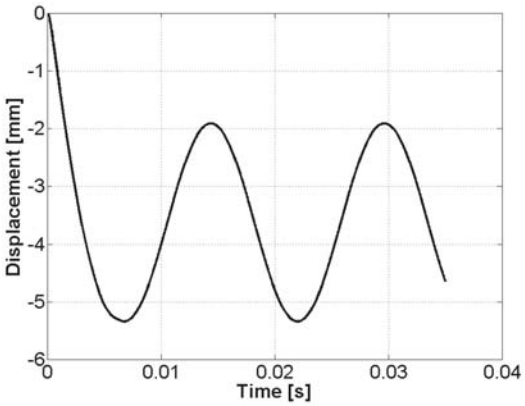

(b) *Displacement from the SDOF analysis on the equivalent beam.*

Figure 9.5.8: *Displacement for the equivalent beam for a drop-height of 1 m.*

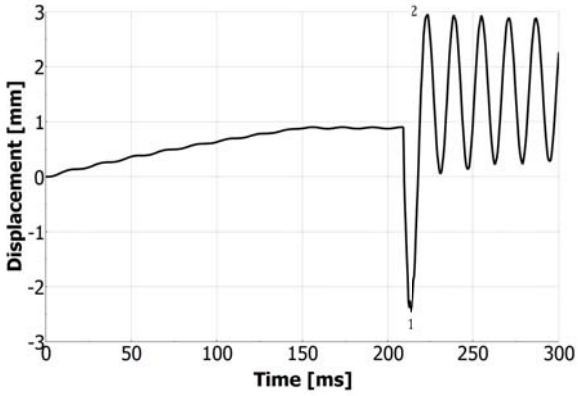

(a) *Displacement in LS-DYNA for the prestressed beam.*

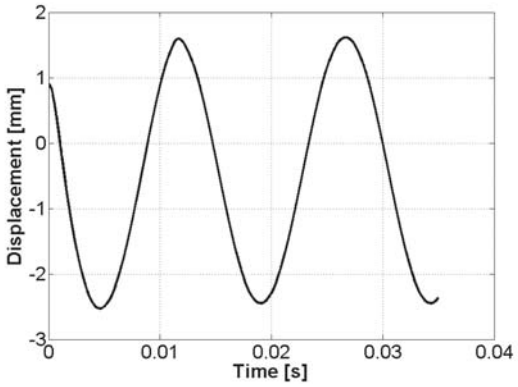

(b) *Displacement from the SDOF analysis on the prestressed beam.*

Figure 9.5.9: *Displacement for the prestressed beam for a drop-height of 1 m.*

The maximum displacement for the equivalent beam in Figure 9.5.8b was -3.375 mm in Ls-DYNA, in the SDOF it was -3.4 mm which is in good correlation with each other. For the prestressed beam the maximum displacement was -2.426 mm while from the SDOF it was -2.8 mm.

10 Results from drop-weight analyses on Beam Case II and Beam Case III - Effect of prestressing

Drop-weight analyses are made on Beam Case II and Beam Case III. Information about the test set-up, geometries and beam data can be found in Chapter **??**.

For each drop-height the prestressed beam (Beam Case II) and the equivalent beam (Beam Case III) are compared with regard to midspan deflections, crack patterns and stresses in the reinforcement steel.

10.1 0.15m drop-height

Figure 10.1.1 displays the midspan deflections for the prestressed beam and the equivalent beam when the drop-weight falls from a height of 0.15 m. The numbers 1 and 2 denotes the times when the maximum downward deflection occur (1) and when the maximum upward deflection occur (2).

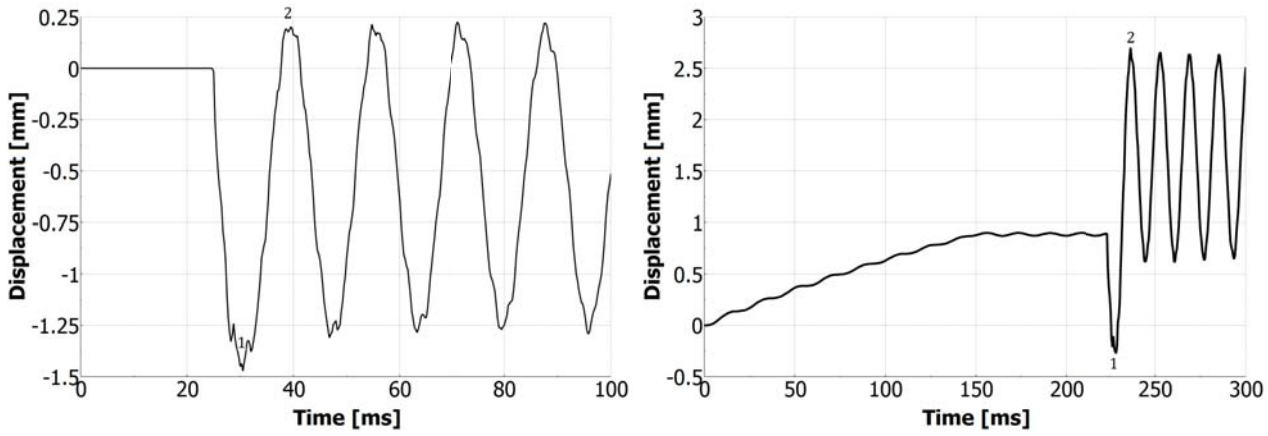

(a) *Displacement of the equivalent beam* (b) *Displacement of the prestressed beam*

Figure 10.1.1: *Displacement of the equivalent and prestressed beam for a drop-height of 0.15 m.*

The prestressed beam reaches a maximum downward deflection of -0.25 mm followed by a notable maximum upward deflection of 2.7 mm. After impact the beam starts to oscillate around a new equilibrium deflection of about 1.75 mm. The prestressing effect counteracts the initial downward deflection with a reversed second order moment effect. While this effect is beneficial during the downward deflection phase it becomes an unfavorable effect once the beam starts to deflect upwards as it amplifies the upward acceleration of the beam. This behaviour can also explain the new, somewhat higher, equilibrium deflection of the beam. Due to the relatively high upward deflection the beam experiences tensile stresses along the top surface. Those stresses give rise to tensile strains that, even though they are not large enough to cause fully developed cracks, induces permanent damage along the top side of the beam, see Figure 10.4.3b. This damage seems to be enough to make the beam less stiff in the upward direction, hence resulting in a new upward equilibrium deflection due to the prestressing force.

The equivalent beam reaches a maximum downward deflection of -1.4 mm followed by a maximum upward deflection of 0.20 mm. After impact the beam oscillates around a new equilibrium deflection of about -0.5 mm. The reason behind the new equilibrium level follows the same arguing as for the prestressed beam, i.e. during the downward deflection the bottom side of the beam experiences tensile strains which are large enough to induce permanent damage, see Figure 10.1.2a. This damage is enough to make the beam less stiff in the downward direction. It should however be noted that the new equilibrium deflection level is very close to zero, the beam could be said to behave more or less like an uncracked beam.

Figure 10.1.2 and Figure 10.1.3 displays the crack patterns for the equivalent and the prestressed beam respectively. The figures labelled a) shows the crack patterns at the time of the maximum downward deflections while those labelled b) shows the crack patterns at the time of the maximum upward deflections. None of the beams displays any fully developed cracks. However, Figure 10.4.3b and Figure 10.1.1b indicates permanent tensile strains close to the cracking strains at the top- and bottom of the beam respectively. As mentioned in the text regarding the midspan deflections, this damage is enough to set the beam into a new equilibrium deflection after impact.

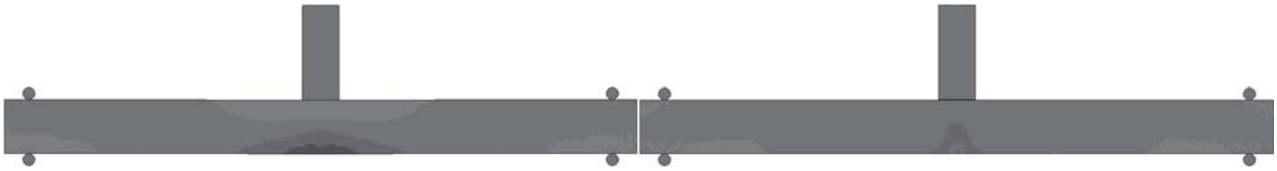

(a) *Crack pattern at maximum downward displacement* (b) *Crack pattern at maximum upward deflection*

Figure 10.1.2: *Crack patterns of the equivalent beam for a drop-height of 0.15 m.*

(a) *Crack pattern at maximum downward displacement* (b) *Crack pattern at maximum upward deflection*

Figure 10.1.3: *Crack patterns of the prestressed beam for a drop-height of 0.15 m.*

Figure 10.1.4 displays the stresses in the steel layers for the prestressed and the equivalent beam and how it changes over time. The numbers 1 and 2 denotes the times when the maximum downward deflection occur (1) and when the maximum upward deflection occur (2). Those numbers corresponds to the same numbers in Figure 10.1.1.

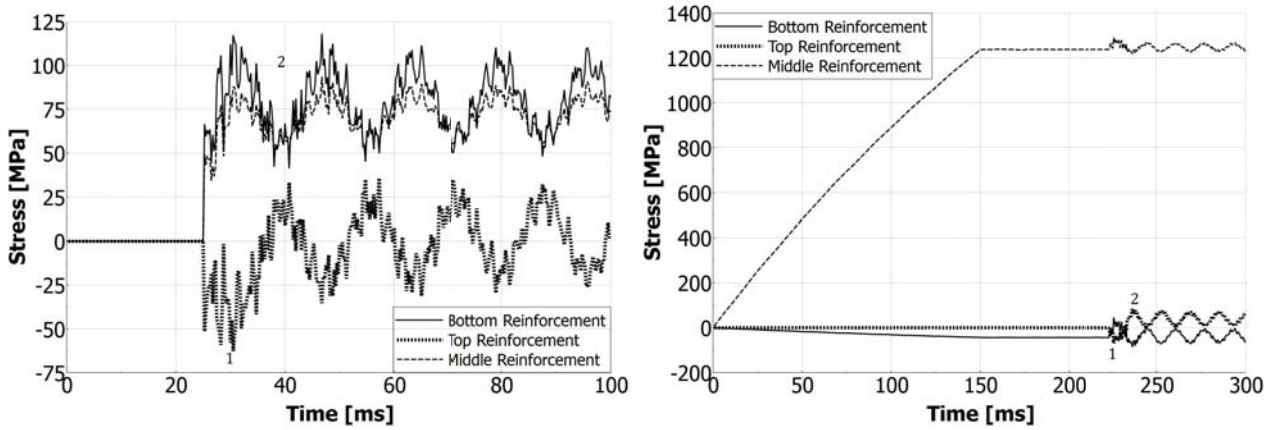

(a) *Steel stresses in the equivalent beam* (b) *Steel stresses in the prestressed beam*

Figure 10.1.4: *Steel stresses for the equivalent and prestressed beam for a drop-height of 0.15 m.*

The prestressing steel in the prestressed beam are tensioned during the first 150 ms after which the stress becomes constant for a period of time. Simultaneously as the beam is being tensioned the bottom reinforcement becomes successively more compressed while the top reinforcement experiences some very small tensile stresses (not visible in the graph). The drop-weight hits the beam at a time of approximately 225 ms which induces some stress variations into the steel layers. Using point 1 and 2 as reference points it can be seen that the steel stresses oscillates according to expectations following the oscillations of the beam deflection. However, a noteworthy observation is that the top reinforcement oscillates around a new stress level after impact. This observation can be coupled to the reasoning above regarding the damaged top surface of the beam during the upward deflection. If this damage resulted in a less stiff beam in the upward direction and hence also a new larger equilibrium deflection, it is only reasonable that also the stresses in the top reinforcement oscillates around a new higher stress level.

10.2 1.0m drop-height

Figure 10.2.1 displays the midspan deflections for the prestressed beam and the equivalent beam when the drop-weight falls from a height of 1.0 m. The numbers 1 and 2 denotes the times when the maximum downward deflection occur (1) and when the maximum upward deflection occur (2).

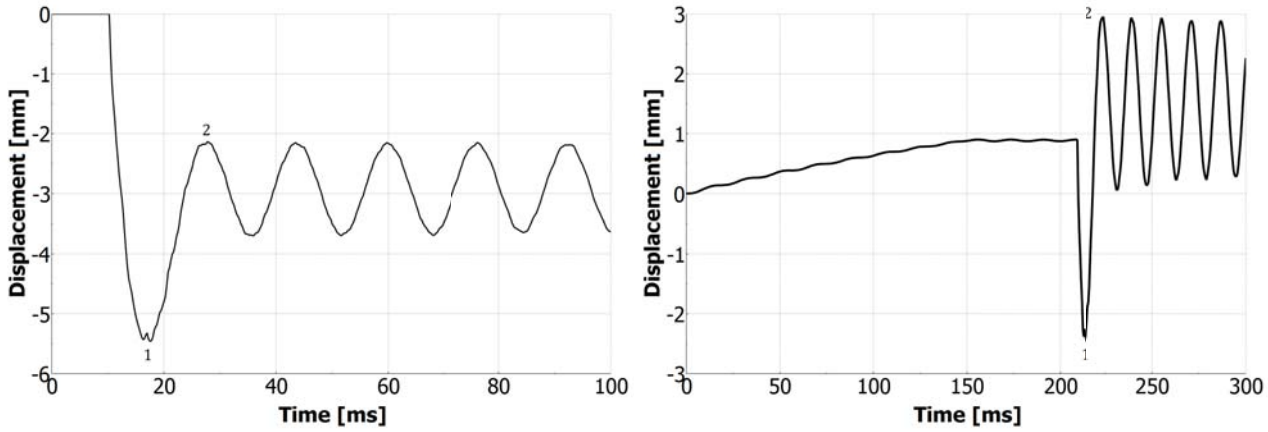

(a) *Displacement of the equivalent beam* (b) *Displacement of the prestressed beam*

Figure 10.2.1: *Displacement of the equivalent and prestressed beam for a drop-height of 1.0 m.*

The prestressed beam reaches a maximum downward deflection of -2.5 mm followed by a relatively large upward deflection of 3.0 mm. A new equilibrium deflection is found at around 1.5 mm. Aside from the overall larger deformations the shape of the deflection curve is very similar to the corresponding curve for the 0.15 m drop-height. Hence a reference is made to that section for an explanation of the curve.

The maximum downward deflection of the equivalent beam is -5.5 mm while the maximum upward deflection is -2.2 mm. After impact the beam oscillates around a new equilibrium deflection of about -2.9 mm. The relatively large maximum downward deflection as well as the following oscillation level indicates that the beam has become cracked at the bottom side. A noteworthy observation can be made here. Since none of the steel layers yields, see Figure 10.3.4a,and because gravity is not considered the weight do not rest on the beam after impact. The beam should deflect back towards its original position around zero deflection and start oscillation approximately around this level. The fact that it does not indicates a strange behaviour. The reason behind this could be connected to how the CSCM handles damage. As explained in Chapter 6 damage will start to accumulate once the tensile strength has been reached and then if unloaded it will obtain a new lower stiffness and plastic deformations. If at this point the solid is subjected to compression the curve starts at the new point of equilibrium. This is visualized in Figure 10.2.2 where a cube is subjected to tension and then compressed. It can be seen there are plastic strains due to the tension, and then once compression starts it follow the compression curve with the initial Young's modulus.

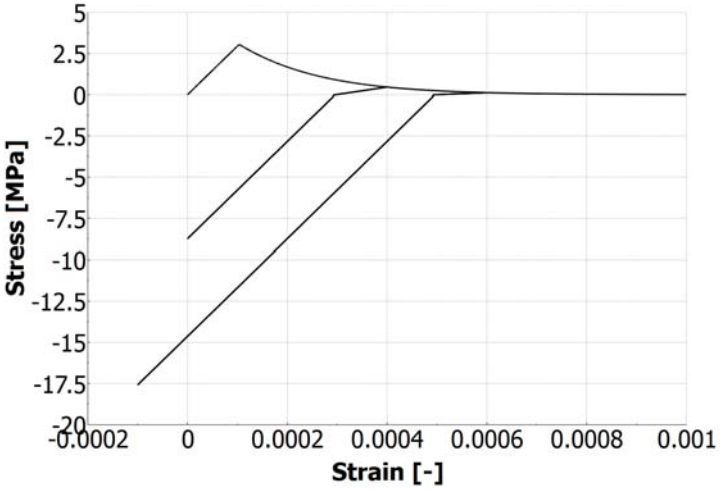

Figure 10.2.2: *The transition behaviour between tension and compression for a cube.*

Since the compression curve is elastic up until the compressive strength no negative plastic deformations will occur until that point has been reached. This is a realistic since in reality the cracks are permanent, if the reinforcement does not yield the cracks would return to their original state when unloaded, and thereby close the cracks. In the models however the motion of the reinforcement is fully coupled to the motions of the surrounding concrete. If the concrete then experience plastic deformations in tension the reinforcement will be forced to experience the same amount of plastic deformations even though it is still in its elastic range. The result is a permanent deflection of the beam which is indicated by the new equilibrium deflection level in Figure 10.2.1a.

Figure 10.2.3 and Figure 10.3.2 displays the crack patterns for the prestressed and the equivalent beam respectively. The figures labelled a) shows the crack patterns at the time of the maximum downward deflections while those labelled b) shows the crack patterns at the time of the maximum upward deflections. Notable is that the prestressed beam indicates a relatively small amount of cracking at the bottom side as well as at the top side while the equivalent beam is cracked at the bottom side while the top side cracking is not very large.

(a) *Crack pattern at maximum downward displacement* (b) *Crack pattern at maximum upward deflection*

Figure 10.2.3: *Crack patterns of the equivalent beam for a drop-height of 1.0 m.*

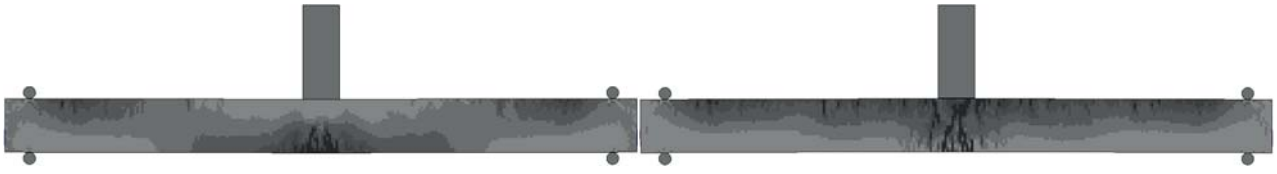

(a) *Crack pattern at maximum downward displacement* (b) *Crack pattern at maximum upward deflection*

Figure 10.2.4: *Crack patterns of the prestressed beam for a drop-height of 1.0 m.*

Figure 10.2.5 displays the stresses in the steel layers for the prestressed and the equivalent beam respectively and how it changes over time. The numbers 1 and 2 denotes the times when the maximum downward deflection occur (1) and when the maximum upward deflection occur (2). Those numbers corresponds to the same numbers in Figure 10.2.1.

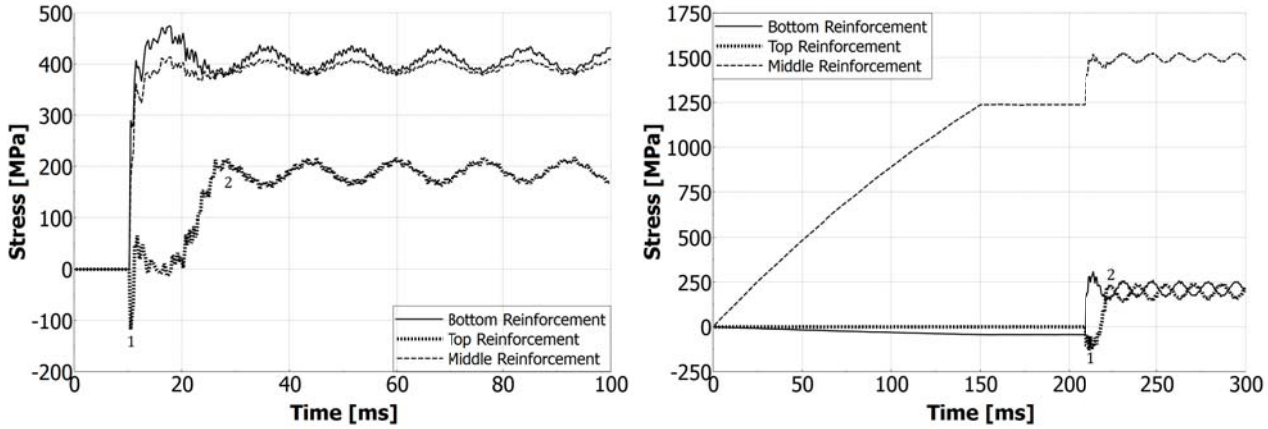

(a) *Steel stresses in the equivalent beam* (b) *Steel stresses in the prestressed beam*

Figure 10.2.5: *Steel stresses for the equivalent and prestressed beam for a drop-height of 1.0 m.*

The drop-weight hits the prestressed beam at a time of approximately 210 ms which induces stress variations into the steel layers. At the time 1 the stresses in all steel layers behaves according to expectations; cracks occur at the top- and bottom side followed by stress concentrations in the steel. However, at time 2, the stress behaviour starts to deviate from expectations. As none of the steel layers yields they should strive to elastically return to their original locations after impact and oscillate around those levels. Hence the stresses should follow the same behaviour; to oscillate around their original steel stresses as they were before impact. Instead, the steel stresses at time 2 shows a response where new equilibrium stress levels are found. Moreover those stress levels indicates that the entire cross section would be in tension as all steel layers oscillates around tension stress levels. This behaviour does not follow an expected structural behaviour and is probably due to the same cause as for the unexpected deflection shape for the equivalent beam described above. I.e. that the steel are prevented to elastically regress by surrounding concrete elements and therefore stays in a tensioned state.

The equivalent beam behaves similarly to the prestressed beam with regard to the steel stresses. None of the steel layers reaches yielding which means that the oscillations should occur around the original equilibrium steel stresses, i.e. around zero stresses. This is not the case according to the graph which shows new equilibrium stress levels, all within the tension field.

10.3 2.0m drop-height

Figure 10.3.1 displays the midspan deflections for the prestressed beam and the equivalent beam respectively when the drop-weight falls from a height of 2.0 m. The numbers 1 and 2 denotes the times when the maximum downward deflection occur (1) and when the maximum upward deflection occur (2).

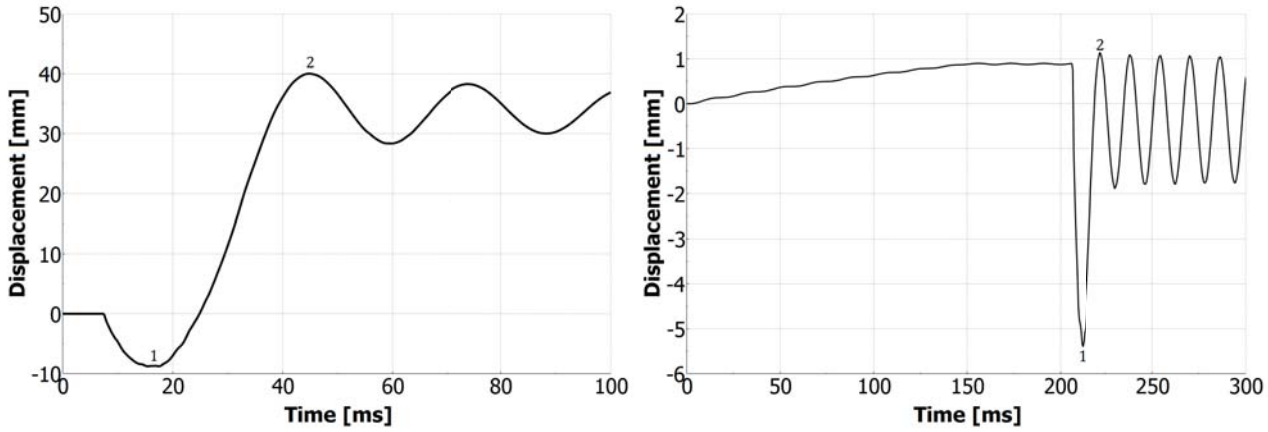

(a) *Displacement of the equivalent beam* (b) *Displacement of the prestressed beam*

Figure 10.3.1: *Displacement of the equivalent and prestressed beam for a drop-height of 2.0 m.*

The prestressed beam reaches a maximum downward deflection of -5.5 mm followed by an upward deflection of 1.2 mm. Further, a new equilibrium deflection is found around a negative deflection of about -0.5 mm. Again the shape of the deflection curve is very similar to the ones presented in Figure 10.1.1b and Figure 10.2.1b. The large upward deflection relatively the maximum downward deflection could once again be due to favourable second order moment effects during the upward acceleration of the beam. Moreover, since none of the steel layers yields, it could again be argued that the equilibrium deflection level should be around the original deflection due to prestressing. If the lower stiffness in upward direction, due to cracks on the top part of the beam, is also added to the reasoning, the new equilibrium oscillation level should even be higher than the original deflection of the beam, as was the case for the 0.15 m drop-height see Section 10.1. This is however not the case according to Figure 10.3.1. And once again a possible explanation could be that the bottom side of the beam is significantly damaged in tension during the downward deflection, and while the still elastic steel strives to get back to its original position it is prevented to do so by the surrounding permanently damaged concrete. A direct consequence of this would be a permanent downward deflection of the beam, which is what Figure 10.3.1 indicates.

The deflection of the equivalent beam provides no useful information. All steel layers has reached yielding after 20 ms, see Figure 10.3.4, which approximately corresponds to the time of the maximum downward deflection. This is followed by a huge upward deflection and a new equilibrium deflection level of about 13 mm. The strange deformation curve is a consequence of the failure of the beam. And this failure can be questioned since it has been showed above that the stress levels in the steel layers is increased during the downward deflection but are not allowed to experience any stress relief when the beam starts to deflect upwards again.

Figure 10.3.2 and Figure 10.3.3 displays the crack patterns for the prestressed and the equivalent beam respectively. The figures labelled a) shows the crack patterns at the time of the maximum downward deflections while those labelled b) shows the crack patterns at the time of the maximum upward deflections. It can be seen that the prestressed beam shows distinct crack patterns both at the top- and bottom side of the beam leading to large stress concentrations in the steel layers, see Figure 10.3.4. Regarding the equivalent beam the crack patterns visualizes severe damage along the top- and bottom side of the beam. This corresponds well to the failure behaviour indicated in Figure 10.3.1.

(a) *Crack pattern at maximum downward displacement* (b) *Crack pattern at maximum upward deflection*

Figure 10.3.2: *Crack patterns of the equivalent beam for a drop-height of 2.0 m.*

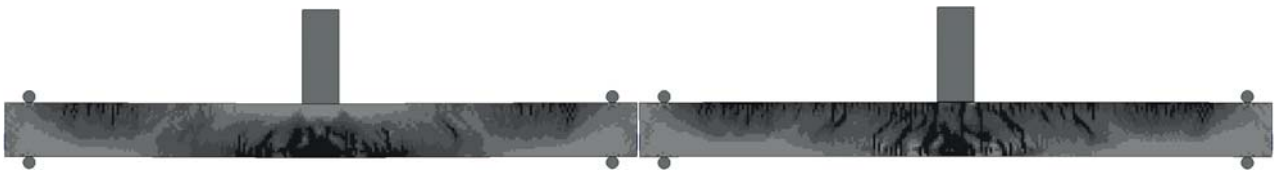

(a) *Crack pattern at maximum downward displacement* (b) *Crack pattern at maximum upward deflection*

Figure 10.3.3: *Crack patterns of the prestressed beam for a drop-height of 2.0 m.*

Figure 10.3.4 displays the stresses in the steel layers for the prestressed and the equivalent beam respectively and how it changes over time. The numbers 1 and 2 denotes the times when the maximum downward deflection occur (1) and when the maximum upward deflection occur (2).

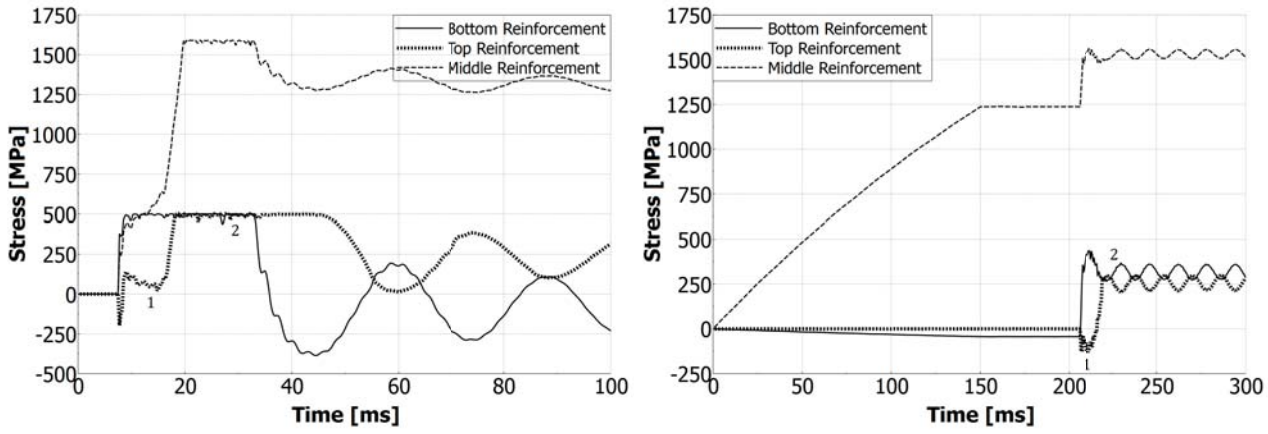

(a) *Steel stresses in the equivalent beam* (b) *Steel stresses in the prestressed beam*

Figure 10.3.4: *Steel stresses for the equivalent and prestressed beam for a drop-height of 2.0 m.*

Aside the magnitudes of the stresses, the steel stresses in the prestressed beam follow the exact same behaviour as was the case for the 1.0 m drop-height shown in Figure 10.2.5. A reference is made to the previous section for comments on the behaviour. Figure 10.3.4b confirms what have been stated

above regarding failure of the equivalent beam. The figure mainly serves as a verification of that theory.

10.4 3.0m drop-height

Figure 10.4.1 displays the midspan deflections for the prestressed beam and the equivalent beam respectively when the drop-weight falls from a height of 3.0 m. This load case merely intends to show a scenario where both beams fails. It is hard to discuss any results beyond the very first downward deflection of the beams and therefore no in-depth explanations will be given regarding their structural behaviour.

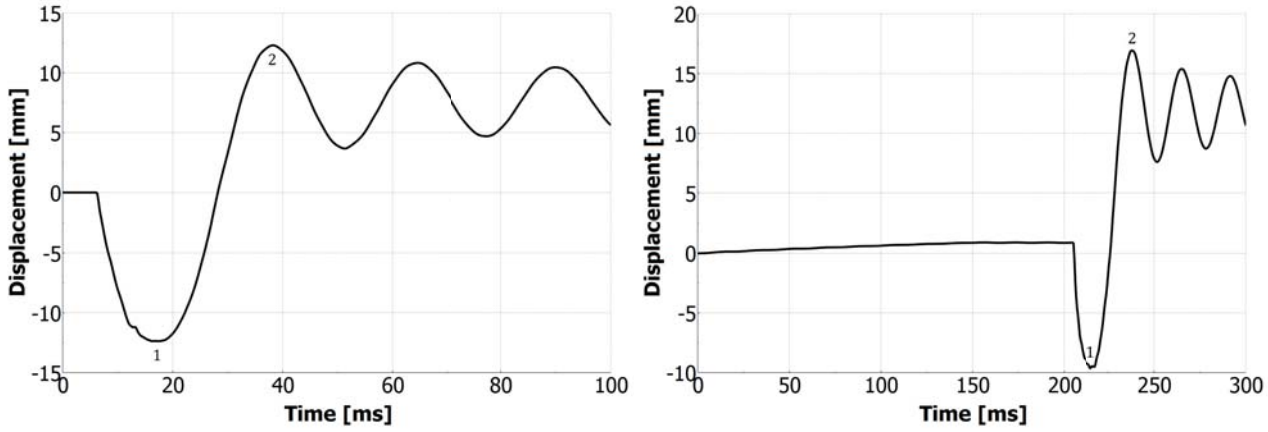

(a) *Displacement of the equivalent beam* (b) *Displacement of the prestressed beam*

Figure 10.4.1: *Displacement of the equivalent and prestressed beam for a drop-height of 3.0 m.*

The prestressed beam reaches a maximum downward deflection of -9 mm followed by an upward deflection of 17 mm. It can be seen that the upward deflection occurs simultaneously as the yielding of the steel layers, see Figure 10.4.4. Hence an explanation to the very large positive deformation could be that the second order moment effects, due to prestressing, experiences very little resistance from the beam as it pushes the beam upwards. This is not a reasonable structural behaviour and once again it seems to originate from the strange way in which the model accumulates tensile stresses into the steel layers.

The equivalent beam reaches a maximum downward deflection of -23.5 mm followed by a maximum upward deflection of -6.5 mm. A new equilibrium deflection level is approximately found around -11.5 mm. In contrast to the equivalent beam for the 2.0 m drop-height this beam displays a reasonable structural behaviour. The new lower equilibrium deflection level is now motivated by the fact that the steel actually yields and so gives the beam a permanent downward deflection. It could of course be argued if this new equilibrium level should be smaller, closer to zero, based on the previously presented theory that elastic regression of the steel is prevented once the surrounding concrete has been damaged in tension.

Figure 10.4.2 and Figure 10.4.3 displays the crack patterns for the prestressed and the equivalent beam respectively. The figures labelled a) shows the crack patterns at the time of the maximum

downward deflections while those labelled b) shows the crack patterns at the time of the maximum upward deflections. As can be seen in the figures both beams are severely damaged during impact and they mostly serves as a visual confirmation of the failure of the beams.

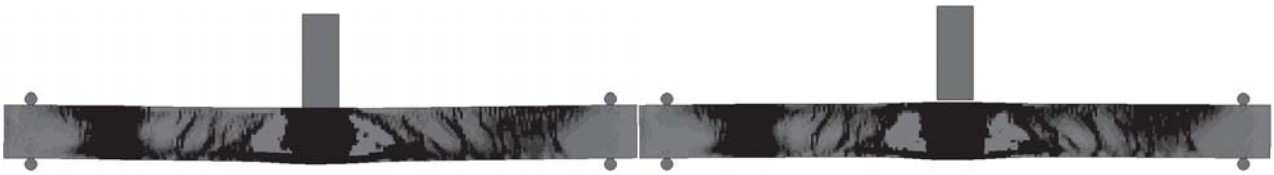

(a) *Crack pattern at maximum downward displacement* (b) *Crack pattern at maximum upward deflection*

Figure 10.4.2: *Crack patterns of the equivalent beam for a drop-height of 2.0 m.*

(a) *Crack pattern at maximum downward displacement* (b) *Crack pattern at maximum upward deflection*

Figure 10.4.3: *Crack patterns of the prestressed beam for a drop-height of 2.0 m.*

Figure 10.4.4 displays the stresses in the steel layers for the prestressed and the equivalent beam and how it changes over time. The strange behaviour of the steel stresses has been discussed in previous sections so the figures mostly serve as a proof of the failure of the beams.

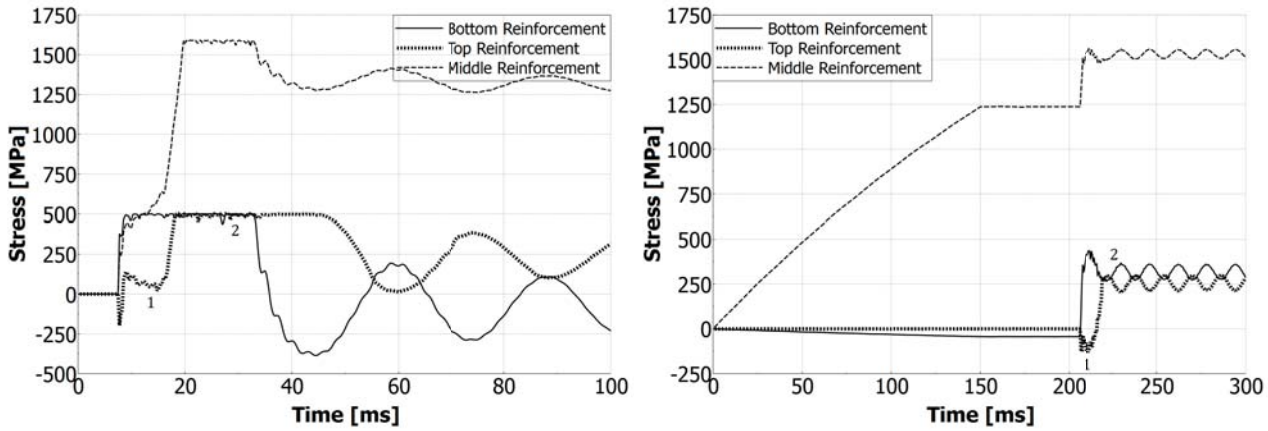

(a) *Steel stresses in the equivalent beam* (b) *Steel stresses in the prestressed beam*

Figure 10.4.4: *Steel stresses for the equivalent and prestressed beam for a drop-height of 3.0 m.*

11 Discussion

The main objectives have been achieved in this thesis. A well performing FE-model of a reinforced- and prestressed concrete beam has been developed using the FE-software LS-DYNA. Further, the four concrete material models CDPM2-Bilinear, CDPM2-Linear, CSCM and Winfrith has been evaluated with regard to performance during both statically- and dynamically applied loads. Their sensitivity towards calibration of certain parameters was also tested. Finally, with the use of the developed FE-model and a suitable concrete material model, the effect of prestressing was evaluated for dynamically loaded concrete beams.

In this chapter some discussions will be made linked to the main objectives as well to some other that have emerged during the working process.

11.1 The effect of prestressing on dynamically loaded concrete beams

In Chapter 10 the results from a drop weight falling on a prestressed and an equivalent reinforced beam can be seen. The effect of prestressing is mainly that, as could be expected, it has delayed crack initiation, smaller deflections and higher capacity compared to a reinforced beam. One interesting effect that can be observed however is the new equilibrium that the beam reaches after the impact. The change in equilibrium is present in both the reinforced and the prestressed cases. But in the prestressed case it is more prominent and it even experience an upward shift in equilibrium. It is the authors theory that this is because of the reduction in stiffness in that direction, cracks forming and unsymmetrical placement of reinforcement. So after the impact the prestressing force will have a bigger impact on the upward deflection. It could be argued that if gravity had been included in the models this behaviour would have disappeared, but since the effect of gravity would have been constant through the whole simulation and therefore caused a shift i downwards for all the results. For example when looking at the weight falling from 0.15 m in Section 10.1 there are no cracks formed in the bottom part of the beam during impact while the upper part experience some cracking. Therefore even if gravity was present the loss in upward stiffness should result in an increase in deflection due to prestressing force. The fact that equivalent reinforced beam experience a shift in equilibrium even though the reinforcement does not yield will be discussed in Section 11.2.

An other observation that can be made about the effect of prestressing is the crack pattern, for all the drop heights it displays a more distinct pattern of cracks in the top part of the beam compared to the equivalent. This again is something that could be expected due to the positive moment the prestressing causes. Since the prestressing reinforcement is straight this moment is constant over the length of the beam which can be seen causing a rather uniform distribution of cracks in the top of the beam. The lack of an experiment to properly validate the dynamic behaviour of a prestressed beam is missing, this was due to the difficulties in finding one where the test set-up and beam where adequately described, most of them had crucial details missing and therefore no good comparison could be made. But since the static behaviour of both reinforced and prestressed beams correlated well with analytical results and that the dynamic behaviour of a reinforced beam correlated well with experiments. It was reasonable to suggest that the prestressed beam would also behave in a satisfactory way during dynamic loading.

It should also be said the the behaviour after the initial peak is difficult to interpret and that this behaviour needs to be investigated further. The first peak displacement however is seen to be in good correlation with what could be expected.

11.2 Discussion about modelling technique and LS-DYNA

All the models in this report where created using the pre-processing software ANSA with a LS-DYNA deck, then LS-DYNA was used as a solver while the post processing was performed with META which is a part of ANSA. This caused some issues since ANSA and META did not contain all of the functions and material models available in LS-DYNA. For example CDPM2 had to be manually defined and then added into the input file. This lead to some restriction as to what could be analysed, for example an extra way of coupling the reinforcement to the concrete with *CONTACT-1D seemed promising but any attempts at doing it manually were unsuccessful an therefore it had to be omitted from the report. With the post-processor the main issue was that there was no way of obtaining a moment or shear force curve. Ls-DYNA itself however yielded good results especially in the dynamic load cases. For static loads the software is very sensitive, if things has the possibility to osculate they will start to osculate, and this can also be seen in the results form the static analyses. Even thought the load was ramped up linearly and very slowly it caused some oscillations. These were deemed to be small enough but could still be one reason as to why the analytical and numerical static results differ.

The prestressing method put forward in this report, is behaving in an satisfactory way. In the static analyses a force displacement curve was obtained that corresponds well with the real behaviour of a prestressed beam. The only main issue with the method is that the strain calculated from a certain temperature differ slightly from the strain seen in the actual model. This is believed to be because of local deformations that occur around the rigid edges that the prestressing is connected to. For the lower temperature the strains correlated better than for the higher temperature, the same correlation could be seen with the local deformations. This was however deemed to have very little impact on the global behaviour of the model. The method for grouting the prestressing wire with a *CLIS* constraint to obtain a strain compatibility also seems to be working but however this constraint seems to have some issues in dynamic post peak behaviour.

A theory behind the strange post peak behaviour is presented in Chapter 10 and could possibly be resolved by using a different method for the reinforcement-concrete interaction but further investigations need to be done on this behaviour.

11.3 Discussion about material model evaluation

The material models where mainly evaluated against displacements and crack patterns. This is not enough to make a full evaluation of a material model. However in the scope of this report it was considered enough since those where the main parameters that were going to be compared. Because of that it was a big problem that the CSCM crack pattern could not be plotted in META, the infinitesimal strains did however display good approximative crack patterns. CDPM2 did show very good behaviour in all of the different analyses and would have been preferable to continue using on the prestressed beam. But when running simulations with CDPM2 a specific binary had to be used.

The same binary did not function with the method for modelling prestressing. The reason behind this could not be found and therefore the decision to go forward with CSCM was taken. It also would have been preferable to compare several material models, but due to time restrictions and lack of models implemented in ANSA this had to be limited.

11.4 Discussion about SDOF

The SDOF-analyses where added to the report to be used as an analytical validation of the maximum displacements during impact loading. As it turned out it was not a very effective tool to use in this way, mainly because it is very sensitive to the shape of the force applied. In previous reports (ULRIKAS rapport) that used the same SDOF method a force was defined in MATLAB and then the same force was applied to a FE-model. In this report the opposite was attempted, to match the MATLAB force to an actual experiment and results from FEM. Even though the same impulse was used the shape of the force yielded very different results. So quite a bit of calibration had to be done in order to get a good correlation between the results. Therefore it could be argued that it's not really a validation for the beam. A decision was made to leave the SDOF results in the report anyway as a way to shine a light on the issues found.

11.5 Further Research

In this report the influence of prestressing on beams was investigated for impact loads, and three different material models were evaluated. There is still however several things that is in need of investigation. Below are some suggestions:

- There is still a lot of research to be performed on the behaviour of prestressed beam that are subjected to dynamic forces. In this report indications could be seen of a possible increase in upwards deflection after an impact. This needs to be further investigated with a different concrete-reinforcement interaction and with gravity to make sure it is a real behaviour. Also the effects on the moment-shear force curve needs to be investigated.
- For evaluating the material models further more analyses should also be performed to for example investigate how they handle shear forces.
- The post peak behaviour needs to be investigated further, for example running the simulations for a longer time to be able to make a judgement once the oscillations have been greatly reduced.
- The behaviour of the Constrained Lagrange in Solid combined with material models that experience damage needs to be investigated further as it seems to cause some issues during dynamic loading.
- The SDOF transformation factors needs to be investigated, in the case when a normal force is present and how to deal with that when deriving the stiffness transformation.

12 References

Bathe, K.-J. (1996) *Finite Element Procedures*. Prentice Hall, Englewood Cliffs, New Jersey, USA.

Belaoura, M. (2010) Compressive behaviour of concrete at high strain rates. *Urban Habitat Constructions under Catastrophic Events*, Taylor and Francis Group, London, pp. 447-450.

Cusatis, G. (2010) Strain-rate effects on concrete behavior, *International Journal of Impact Engineering*, Vol 38, pp. 162-170.

Engström, B. *Design and analysis of prestressed concrete structures*. Göteborg: Chalmers University of Technology. (Report 2011:7)

Erhart, T. (2011) Review of Solids Element Formulations in LS-DYNA. *LS-DYNA Forum 2011*, 12 October, 2011, Stuttgart.

Fujikake, K. Li, B. Soeun, S. (2009) Impact Response of Reinforced Concrete Beam and Its Analytical Evaluation. Journal Of Structural Engineering, vol. 135, ss 938-950. DOI: 10.1061/(ASCE)ST.1943-541X.0000039

Grassl, P. Jirásek, M. (2006) *Damage-plastic model for concrete failure*. Int.J.Solids Struct. 43, 7166-7196

Johansson, M. Laine, L. (2012) *Bebygelsens motståndsförmåga mot extrem belastning, Del 3: Kapacitet hos byggnader*, s.1:MSB

Livermore Software Technology Corporation (2015) *Hourglassing*.
http://ftp.lstc.com/anonymous/outgoing/jday/hourglass.pdf (2015-04-28)

LS-DYNA MANUAL I. (2012) *LS-DYNA KEYWORD USER'S MANUAL VOLUME I*. Livermore

LS-DYNA MANUAL II. (2012) *LS-DYNA KEYWORD USER'S MANUAL VOLUME II- Material Models*. Livermore

LS-DYNA Support (2015) *Hourglass*.
http://www.dynasupport.com/howtos/element/hourglass (2015-04-29)

Murray, Y. Abu-Odeh, A Bligh, R. (2007) *Evaluation of LS-DYNA Concrete Material Model 159* Federal Highway Administration (FHWA-HRT-05-063)

Nyström, U. (2006) *Design with regard to explosions*. Göteborg: Chalmers University of Technology.(Master's Thesis in the International Master's Programme Structural Engineering)

Nyström, U. (2013) *Modelling of Concrete Structures Subjected to Blast and Fragment Loading* Göteborg: Chalmers University of Technology. (Thesis for the Degree of Doctor of Philosophy)

Riedel, W. Forquin, P. (2013) Modelling the response of concrete structures to dynamic loading, *Understanding the Tensile Properties of Concrete*, Woodhead Publishing, pp. 125-142.

Sangi, A.J (2011) *(*Reinforced Concrete Structures Under Impact Loads). Edinburgh: Heriot-Watt University (Thesis for the Degree of Doctor of Philosophy)

Schwer, L. (2011) The Winfrith Concrete Model: Beauty or Beast ? Insights into the Winfrith Concrete Model. In *8th European LS-DYNA Users Conference*, 23-24 May, 2011, Strasbourg.

Schwer, L. (2014) *Modeling Rebar: The Forgotten Sister in Reinforced Concrete Modeling*

Schwer, L. Murray, Y. (2002) Continuous Surface Cap Model for Geomaterial Modeling: A New LS-DYNA Material Type. In *7th International LS-DYNA Users Conference*, 19-21 May, 2002, Dearborn, 16-35 - 16-50

Räddningsverket. (2005) *Dynamisk lastpåverkan Referensbok*. Räddningsverket, Karlstad, Sweden.

Weerheijm, J. Van Doormaal, J.C.A.M. (2007) Tensile failure of concrete at high loading rates: New test data on strength and fracture energy from instrumented spalling tests. *International Journal of Impact Engineering*, vol.34, issue 3, ss 609-626.

Weerheijm, J. Forquin, P. (2013) Response mechanisms of concrete under impulsive tensile loading, *Understanding the Tensile Properties of Concrete*, Woodhead Publishing, pp. 181-217.

Wu, Y. Crawford, J.E. Magallanes J.M. (2012) Performance of LS-DYNA Concrete Constitutive Models. In *12th International LS-DYNA Users Conference*, 3-5 June, 2012, Dearborn.

A Material models in LS-DYNA

In the following chapter an example of how the material models were defined in LS-DYNA are shown.

A.1 CDPM2

```
*MAT_CONCRETE_DAMAGE_PLASTIC_MODEL
$ Material Type 16 (units: Newtons-millimeter-millisecond-MPa)
$--+---1---+---2---+---3---+---4---+---5---+---6---+---7---+---8
$     MID        RO         G        PR
$#    mid        ro         e        pr       ecc       qh0        ft        fc
      273 2.400E-3     29279    0.1900   1.04439     0.300     3.045    42.000
$#     hp        ah        bh        ch        dh        as        df       fc0
   0.5000  8.000E-2  3.00E-3     2.000  1.00E-6  15.0000    0.8500     10.00
$#   type        bs        wf       wf1       ft1    strflg   failflg
    0.000   1.00000    0.1270       0.0       0.0    0.0000       0.0
```

A.2 CSCM

```
$ .....................................................................
$                          MAT159 MAT_CSCM_CONCRETE
$ .....................................................................
$                  Unconfined Compression Strength
$                f'c = 34.48 MPa (5 ksi cylinder test)
$                3/8in = 9.525mm maximum diameter aggregate
$ Mat 159 (units: KiloNewtons-millimeter-milliseconds-MPa-g-mm^3)
*MAT_CSCM_CONCRETE
 34.48e0   -145.0       0.0       0.0     000.0       0.0      1.25       0.0
$      ER       PRR      SIGY      ETAN       LCP       LCR
$     mid        ro     nplot     incre     irate     erode     recov  itretrc
      273  2.40E-3         1     0.000         0    0.0000     0.000         0
$       pred
       0.000
$--+---1---+---2---+---3---+---4---+---5---+---6---+---7---+---8
$Lambda1  Lambda2  Lambda3  Lambda4  Lambda5  Lambda6  Lambda7  Lambda8
$     fpc     dagg    units
   42.000   10.000        1
$  0.383    0.247    0.173    0.136    0.114    0.086    0.056      0.0
$--+---1---+---2---+---3---+---4---+---5---+---6---+---7---+---8
$       |        |        |        |        |        |        |        |
```

A.3 Winfrith

```
*MAT_WINFRITH_CONCRETE
$     mid        ro        tm        pr       ucs       uts        fe     asize
      273  2.40e-3     29279      0.19        42     3.045     0.090    10.000
$       e        ys        eh   uelong      rate      conm      conl      cont
      0.0       0.0     0.000     0.000       1.0        -3         0         0
$    eps1      eps2      eps3      eps4      eps5      eps6      eps7      eps8
    0.000     0.000     0.000     0.000     0.000     0.000     0.000     0.000
$      p1        p2        p3        p4        p5        p6        p7        p8
    0.000     0.000     0.000     0.000     0.000     0.000     0.000     0.000
```

A.4 Steel

```
*MAT_PLASTIC_KINEMATIC_TITLE
Bending_Rebar
         2 0.00785  200000.       0.3      426.       0.       0.
                                    0.
*MAT_PLASTIC_KINEMATIC_TITLE
Shear_Rebar
         3 0.00785  200000.       0.3      295.       0.       0.
                                    0.
*MAT_PLASTIC_KINEMATIC_TITLE
Prestressing_wire
         5 0.00785  210000.       0.3     1590.       0.       0.
                                    0.
*MAT_NULL_TITLE
Guiding_Cable
         6 0.00785       0.        0.        0.        0. 210000.       0.3
*MAT_ELASTIC_PLASTIC_THERMAL_TITLE
Prestressing_elements
           7    0.00785
    -10000.     10000.
    210000.    210000.
       0.3         0.3
    0.0001      0.0001
     1590.       1590.
     2100.       2100.
```

A.5 Rigid bodies

```
*MAT_RIGID_TITLE
Supports
         4 0.00785 210000.       0.3        0.        0.        0.
       1.0        7.        0.
        0.        0.        0.        0.        0.        0.
*MAT_RIGID_TITLE
Drop_Weight
         5 .059160744 210000.       0.3        0.        0.        0.
       1.0           6.        7.
        0.           0.        0.        0.        0.        0.
```

B Prestressed Beam LS-DYNA

Here is an example of the input data to dyna, this particular one is for the prestressed beam being hit by a falling weight. This is the only one showed in the appendices since it contain all of the setups from the other models but also some extra that are specific for prestressing. In some categories as *NODES the list of nodes has been removed to save space and because it adds no information.

```
$
$ANSA_VERSION;15.1.2;
$
$
$ file created by  A N S A  Sun May 24 18:54:09 2015
$
$ output from :
$
$ C:/Adam/Simuleringar/Beams/Comparison/Prestressed-Equivalent
/Prestressed.ansa
$
*KEYWORD
$
$
$
*CONTROL_ENERGY
         2         2         1         1
*CONTROL_HOURGLASS
         6       0.1
*CONTROL_TERMINATION
     300.
*DATABASE_SECFORC
       0.5         2                 0
*DATABASE_NODOUT
       0.5         2                 0        0.         1
*DATABASE_ELOUT
       0.5         2                 0
*DATABASE_GLSTAT
       0.5         2                 0
*DATABASE_SSSTAT
       0.5         2                 0
*DATABASE_MATSUM
       0.5         2                 0
*DATABASE_NCFORC
       0.5         2                 0
*DATABASE_RCFORC
       0.5         2                 0
*DATABASE_NODFOR
       0.5         2                 0
```

```
*DATABASE_SLEOUT
       0.5         2                    0
*DATABASE_BINARY_D3PLOT
         1.
          0
*DATABASE_BINARY_D3THDT
         1.
*DATABASE_BINARY_INTFOR
         1.
*DATABASE_EXTENT_BINARY
        16         0         3         1         1         1         1         1
         0         0         2         1         1         1         2         1
         1         0        1.         0         0         0
          0
*DATABASE_BINARY_D3CRACK
         1.
*DATABASE_CURVOUT
       0.5         2                   0
*NODE
       3          0.               26.              26.       0       0
       ....
       ....
*CONSTRAINED_NODAL_RIGID_BODY
     271231                      16                    0         0         0
     271232                      17                    0         0         0
*ELEMENT_BEAM_ORIENTATION
       1       2       3       4
        0.       1.       0.
         ...
         ...
*ELEMENT_SOLID
 15077       4
  3464   3465   3466   3467   5882  111490  14285  15579       0       0
 15078       4
  3468   3467   3466   3469  15580   15579  14285  14286       0       0
    ...
    ...
*SET_NODE_LIST
         16
     254919   254921   134227   134248   134269   134290   134206   134185
      ...
      ...
```

```
*SET_NODE_LIST
         17
    254920   254918   133786   133807   133828   133849   133765   133744
    ...
    ...
$ANSA_ID;1;
*CONSTRAINED_LAGRANGE_IN_SOLID_TITLE
        1Top_Rebar
         3        5        1        1        0        2        0        0
        0.       0.       0.       0.       0.       0        0      0.3
        0.       0.       0.        0       0.       0        0        0
                  0        0        0       0.       0       0.
        0.       0.       0.       0.       0.       0.       0.       0.
$ANSA_ID;2;
*CONSTRAINED_LAGRANGE_IN_SOLID_TITLE
        2Bottom_Rebar
         2        5        1        1        0        2        0        0
        0.       0.       0.       0.       0.       0        0      0.3
        0.       0.       0.        0       0.       0        0        0
                  0        0        0       0.       0       0.
        0.       0.       0.       0.       0.       0.       0.       0.
$ANSA_ID;3;
*CONSTRAINED_LAGRANGE_IN_SOLID_TITLE
        3Guiding_TUBe
         7        5        1        1        0        2        0        0
        0.     176.       0.       0.       0.       0        0      0.3
        0.       0.       0.        0       0.       0        0        0
                  0        0        0       0.       0       0.
        0.       0.       0.       0.       0.       0.       0.       0.
$ANSA_ID;4;
*CONSTRAINED_LAGRANGE_IN_SOLID_TITLE
        4Wire_Lagrange
         8        5        1        1        0        2        0        0
      175.    9999.       0.       0.       0.       0        0      0.3
        0.       0.       0.        0       0.       0        0        0
                  0        0        0       0.       0       0.
        0.       0.       0.       0.       0.       0.       0.       0.
*CONTACT_AUTOMATIC_SURFACE_TO_SURFACE_ID
1         Drop_Weight
         1        2        0        0                         1        1
                                                             0

*CONTACT_AUTOMATIC_SURFACE_TO_SURFACE_ID
2         Top_Left_Support
         3        4        0        0                         1        1
                                                             0
```

```
*CONTACT_AUTOMATIC_SURFACE_TO_SURFACE_ID
3         Bottom  Left  support
         6         5         0         0                                   1         1
                                                                           0

*CONTACT_AUTOMATIC_SURFACE_TO_SURFACE_ID
4         Top_Right  Support
         7         8         0         0                                   1         1
                                                                           0

*CONTACT_AUTOMATIC_SURFACE_TO_SURFACE_ID
5         Bottom_Right  support
        10         9         0         0                                   1         1
                                                                           0

*CONTACT_GUIDED_CABLE_SET_ID
6         *CONTACT_GUIDED_CABLE_SET
        11        12         0        1.
*PART
Bottom_Rebar
         2         2         2                                             0
*SECTION_BEAM_TITLE
Bottom_Rebar
       2       1      1.       2      1.
    12.     12.      0.      0.      0.      0.
*PART
Top_Rebar
         3         3         3                                             0
*SECTION_BEAM_TITLE
Top_Rebar
         3         1        1.         2        1.
       12.       12.        0.        0.        0.        0.
*PART
Rigid_Drop_Weight
         4         4         9                   0         0
*SECTION_SOLID_TITLE
Rigid_Drop_Weight
         4         1
*PART
Solid_Concrete
         5         5       273                   0         0
*SECTION_SOLID_TITLE
Solid_Concrete
         5         1
```

```
*PART
Rigid_Supports
         6         6         8                   0           0
*SECTION_SOLID_TITLE
Rigid_Supports
         6         1
*PART
Guiding_Tube
         7         7         6                             0
*SECTION_BEAM_TITLE
Guiding_Tube
         7         1        1.         2        1.
       13.       13.        0.        0.        0.        0.
*PART
Prestressing_Wire
         8         8                                       0
*SECTION_BEAM_TITLE
Prestressing_Wire
         8         1        1.         2        1.
       13.       13.        0.        0.        0.        0.
*PART
Prestressing_Element
         9         9         7                             0
*SECTION_BEAM_TITLE
Prestressing_Element
         9         1        1.         2        1.
       13.       13.        0.        0.        0.        0.
*LOAD_THERMAL_VARIABLE
$ANSA_ID;1;
        13         0
   -5000.        0.         2
*BOUNDARY_PRESCRIBED_MOTION_RIGID_ID
         1Velocity
         4         2         0         1    -4.43         0      201.      200.
*MAT_PLASTIC_KINEMATIC_TITLE
Bottom-Rebar
         2 0.00785  210000.       0.3      500.         0.        0.
                                    0.
*MAT_PLASTIC_KINEMATIC_TITLE
Top_Rebar
         3 0.00785  210000.       0.3      500.         0.        0.
                                    0.
*MAT_PLASTIC_KINEMATIC_TITLE
Prestressing_wire
         5 0.00785  210000.       0.3     1590.         0.        0.
                                    0.
```

```
*MAT_NULL_TITLE
Guiding_Cable
         6 0.00785        0.        0.        0.        0. 210000.       0.3
*MAT_ELASTIC_PLASTIC_THERMAL_TITLE
Prestressing_elements
           7    0.00785
    -10000.      10000.
    210000.     210000.
         0.3          0.3
      0.0001       0.0001
       1590.        1590.
       2100.        2100.
*MAT_RIGID_TITLE
Rigid-Supports
         8 0.00785  210000.       0.3        0.        0.        0.
       1.0         7.         7.
         0.         0.         0.         0.         0.         0.
*MAT_RIGID_TITLE
Drop_Weight
         9 0.003925  210000.       0.3        0.        0.        0.
       1.0         6.         7.
         0.         0.         0.         0.         0.         0.
$ ......................................................................
$                          MAT159 MAT_CSCM_CONCRETE
$ ......................................................................
$                  Unconfined Compression Strength
$                f'c = 34.48 MPa (5 ksi cylinder test)
$                3/8in = 9.525mm maximum diameter aggregate
$ Mat 159 (units: KiloNewtons-millimeter-milliseconds-MPa-g-mm^3)
*MAT_CSCM_CONCRETE
$34.48e0   -145.0       0.0       0.0     000.0       0.0      1.25       0.0
$      ER       PRR      SIGY      ETAN       LCP       LCR
$     mid        ro     nplot     incre     irate     erode     recov  itretrc
       273  2.40E-3         1        0.         1    0.0000      0.00         0
$#   pred
    0.000
$---+---1---+---2---+---3---+---4---+---5---+---6---+---7---+---8
$Lambda1  Lambda2  Lambda3  Lambda4  Lambda5  Lambda6  Lambda7  Lambda8
$     fpc      dagg     units
   48.000    8.0000         1
$  0.383     0.247     0.173     0.136     0.114     0.086     0.056       0.0
$---+---1---+---2---+---3---+---4---+---5---+---6---+---7---+---8
$       |         |         |         |         |         |         |         |
```

```
*HOURGLASS_TITLE
Anonymous HOURGLASS Card
         1         4        0.         0        0.        0.        0.        0.
*DEFINE_CURVE_TITLE
Initial_Velocity
         1         0        1.        1.        0.        0.         0
                  0.                  1.
                100.                  1.
*DEFINE_CURVE_TITLE
Thermal
         2         0        1.        1.        0.        0.         0
                  0.                  0.
                150.                  1.
                300.                  1.
*DATABASE_CROSS_SECTION_PLANE_ID
           1Cross Section
        14    1299.8    −0.2      −0.2   1300.8     −0.2     −0.2        0.
   1299.8     220.2     −0.2     220.4    220.4        0        0
*DATABASE_CROSS_SECTION_PLANE_ID
         2Cross Section quarer
        15   1949.8    220.2     −0.21949.99612    220.2     −0.2        0.
   1949.8     220.2     220.2     220.4      220.4         0        0
$ANSA_ID;1;
*DATABASE_HISTORY_BEAM
   270855   270854   270853   270852   270851   270850   270849   270848
      ...
      ...
$ANSA_ID;2;
*DATABASE_HISTORY_SOLID
   140377   140398   140399   140419   140420   140421   140440   140441
   140442   140443   140461   140462   140463   140464   140465   140482
      ...
      ...
$ANSA_ID;3;
*DATABASE_HISTORY_NODE
   129595   125502   114265   115820
*SET_SEGMENT_TITLE
Under_Weight
         1
   128906   128941   128954   128934
      ...
      ...
```

```
*SET_SEGMENT_TITLE
Drop_Weight
         2
   111490     14285     14256    111492
      ...
      ...
*SET_SEGMENT_TITLE
Beam_Left_Top
         3
   126888    126889    126887    126886
      ...
      ...
*SET_SEGMENT_TITLE
Top_Left_support
         4
   248772    111285    111280    111305
      ...
      ...
*SET_SEGMENT_TITLE
Bottom_Left_support
         5
   250180    108131    108125    108155
      ...
      ...
*SET_SEGMENT_TITLE
Beam_Left_Bottom
         6
    63139      6995      7174     63167
       ...
       ...
*SET_SEGMENT_TITLE
Beam_Right_Top
         7
   131694    131712    131691    131673
      ...
      ...
*SET_SEGMENT_TITLE
Support_right_top
         8
   251244    109904    109898    109928
      ...
      ...
```

```
*SET_SEGMENT_TITLE
Bottom_Right_Support
         9
   252652    109486    109481    109506
      ...
      ...
*SET_SEGMENT_TITLE
Beam_Right_Bottom
        10
   116723    116754    116777    116741
      ...
      ...
*SET_NODE_LIST_TITLE
Guiding_Nodes
        11
   254404    254405    254406    254407    254408    254409    254410    254411
      ...
      ...
*SET_PART_LIST_TITLE
Prestressing_Wire_elements
        12
         8
*SET_NODE_LIST_TITLE
TEMP_Nodes
        13
   254661    254917    254918    254921
*SET_PART_LIST_TITLE
Cross  Section
        14
         5
*SET_PART_LIST_TITLE
Cross  Section@_1
        15
         5

*END
```

C SDOF calculations in MATLAB

Here the MATLAB code for calculating the SDOF response of the beams, using transformations factors. The main algorithm shown here is for Beam Case I. For Case II and III the same code was used but the all the cross sectional parameters were calculated in Mathcad, and this algorithm was then used to find the response of the impact.

C.1 Main algorithm

```
%%%%%%%%%%%%%%%%%%%%%%%%%%%%%%%%%%%%%%%%%%%%%%%%%%%%%%%%%%%%%%%%%%%%%%%%%%%%%%%%%%%%%%%%%%%%%%%%%%%%%%%%%%%%%%%%%%%%%%%%%%%%%%%%%
%   Main algorithm for calculating SDOF response for a RC-beam.
%   Adam Johansson - Johan Fredberg
%   2015-03-16
%%%%%%%%%%%%%%%%%%%%%%%%%%%%%%%%%%%%%%%%%%%%%%%%%%%%%%%%%%%%%%%%%%%%%%%%%%%%%%%%%%%%%%%%%%%%%%%%%%%%%%%%%%%%%%%%%%%%%%%%%%%%%%%%%
%---------------------------------------------------------------------------------------
clc
clear all
close all
tic
%---------------------------------------------------------------------------------------
%% Inputs %%%-------------------------------------------------------------------------------------------
%Units: N-m-s-Pa
%----- Inputs Beam -----%
Ec=30.65*10^9;          % [Pa]   Youngs modulus for concrete
fcc=48*10^6;            % [Pa]   Concrete compression strength
fct=3.177*10^6;         % [Pa]   Concrete tensile strength
L=2.4;                  % [m]    Length of beam
h=0.22;                 % [m]    Height of the beam
w=0.22;                 % [m]    Witdh of the beam
rho=2400;               % [kg/m^3] Density of beam
M=h*w*L*rho;            % [kg]   Mass of beam
A=h*w;                  % [m^2]  Area of beam
ecu=3.5*10^(-3);        % [/]    Ultimate concrete strain

%----- Inputs steel -----%
Es=210*10^9;            % [Pa]   Youngs modulus for steel
fy=500*10^6;            % [Pa]   Steel yield strength
fyp=1590*10^6;          % [Pa]   Prestressing Stel yield strength
d1=0.012;               % [m]    Diamter of reinforcement
d2=0.013;               % [m]    Diamter of prestressing steel
nc=2;                   % [/]    Number of compressive bars
nt=2;                   % [/]    Number of tensile bars
Ast=((d1^2*pi)/4)*nt;% [m^2]  Area of steel in tension
Asc=((d1^2*pi)/4)*nc;% [m^2]  Area of steel in compression
Ast2=((d2^2*pi)/4)      % [m^2]  Area of prestressing steel
```

```
cover=0.02+d1/2;        % [m]     Cover thickness
dp=0.16                 % [m]     Distance from prestressing bar to top
dt=0.194;               % [m]     Distance from tension rebar to top
dc=0.026;               % [m]     Distance from compression rebar to top
C=0;                    % [Ns/m] Damping is neglected

% Factors %
alpha=Es/Ec;        % [/] Relationship between E for concrete and steel
%------ Transformation Factors ------%
%Elastic range
kmel=0.486;
%Plastic range
kmpl=1/3;
%Elasto-plastic range
kmelpl=(kmel+kmpl)/2;
%-----------------------------------------------------------------------
%% Calculating Moment capacity %%
%-----------------------------------------------------------------------
%------ Moment capacity Stadium I ------%
% The values here are taken from hand calculated values in APPENDIX XX

cg=0.111                % [m]     Center of Gravity
z=h-cg;                 % [m]     Distance from top to Cog
A1=0.052;               % [m^2] Equivalent crosssection Area
I1=2.158*10^(-4);       % [m^4] Moment of inertia Stadium I
k=0.6+(0.4/(h^(1/4))) % [/]     Factor for the flexular strength 1<k<1.45
if k<=1
    k=1;
end

if 1.45<=k
    k=1.45;
end
fcbt=k*fct;             % [Pa]   Flexular strength of concrete
Mcr=6.577*10^3;         % [Nm]   Moment capacity for Stadium I

%------ Moment capacity Stadium II ------%

x=0.051                 % [m]     Distance to neutral layer
Acc=w*x;                % [m^2] Area of cracked concrete
A2=0.015;               % [m^2] Equivalent Area in Stadium  II
I2=5.305*10^(-5)        % [m^4] Moment of inertia Stadium II
fs=fy/alpha;            % [Pa] Fictive concrete stress at rebar level
z=dt-x;                 % [m] Dist. from neutral layer to tension rebar
Mspl=50.74*10^3;        % [Nm] Momencapacity Stadium II
```

```
%-------------------------------------------------------------------------
%% Calculating the critical displacements %%
%-------------------------------------------------------------------------
%------ ucr ------%
Fcr=11;                 % [N] Critical force
ucr=0.477*10^(-3)       % [m] Critical displacement for elastic region

%------ uspl ------%
Fspl=(Mspl*4)/L;        % [N] Critical force
uspl=14.97*10^-3;       % [m] Critical dis for elasto-plastic region

%------ upl ------%
Fpl=(Mspl*4)/L;                 % [N] Critical force
upl=uspl+(Fpl*L^3)/(48*Ec*I2);  % [m] Critical dis for plastic region

%-------------------------------------------------------------------------
%% Calculating stiffness for the system %%
%-------------------------------------------------------------------------
K1=(48*Ec*I1)/(L^3);          % [N/m] Stiffness for elastic region
K2=(48*Ec*I2)/(L^3);          % [N/m] Stiffness for Stadium 2
K21=(Fspl-Fcr)/(uspl-ucr); % [N/m] Stiffness for elasto-plastic region
K=[K1,K21,K2];                % Compiling the stiffnes
%-------------------------------------------------------------------------
%% Central difference method %%
%-------------------------------------------------------------------------
%------ Calculating the eigenfrequency ------%
lambda1=eig(K1,M*kmpl);                 % Eigenfrequency Stadium I
lambda2=eig(K21,M*kmpl);                % Eigenfrequency Stadium II
lambda3=eig(K2,M*kmpl);                 % Eigenfrequency Stadium III
Lambda=[lambda1,lambda2,lambda3];
%------ Calculating the timestep ------%

t_crit=2/max(sqrt((max(Lambda))));  % [s] Critical timestep
%t_step=0.01*t_crit;                % [s] Decreased timestep
%t_tot=10;                          % [s] Total time
t_step=0.003*(10^-3);               % [s] Predefined time step
t_tot=35*(10^-3);                   % [s] Total run time
n=ceil(t_tot/t_step);               % [s] Number of iterations
ms=0.001                            % [s] Impact time
nostep=round(ms/t_step)             % [/] Number of steps for impact
%------ Define point Load ------%

M_w=50;
vel=4.43;
Imp=M_w*vel;
t1=0.0005;
```

```
P1=round((0.9*Imp*2)/t1)
nostep1=round(t1/t_step);
t2=0.005;
P2=round(((0)*Imp*2)/t2);
nostep2=round(t2/t_step)
t3=0.001;
P3=round(((0.1*Imp*2)/t3))
nostep3=round(t3/t_step)

%------ Impact Load ------%
P=Pel;
F=zeros(1,n+1);
F(2:nostep1)=linspace(P1,0,length(2:nostep1));
F((nostep1+1):(nostep1+nostep2))=...
linspace(P2,0,length(((nostep1+1):(nostep1+nostep2))));
F((nostep1+nostep2+1):(nostep1+nostep2+nostep3))=...
linspace(0,P3,length(((nostep1+nostep2+1):(nostep1+nostep2+nostep3))));
Impulse=P1*((nostep1*t_step)/2)...
+P2*((nostep2*t_step)/2)+P3*((nostep3*t_step)/2)

%------ Perform the central difference method ------%
[u,a,v,k,F,o,R] = CDM(M,K,C,F,n,t_step,ucr,uspl,upl,Fpl,Fcr,h);

u=-u;
%------ Plot the results ------%
figure(1)
%subplot(2,2,2)
plot((1:o)*t_step,u(1:o)*1000,'k')
title('Time vs Displacement')
xlabel('Time [s]')
ylabel('Displacement [mm]')

figure(2)
%subplot(2,2,3)
plot((1:o)*t_step,F(1:o)/1000,'k')
title('Time vs Force')
xlabel('Time [s]')
ylabel('Force [kN]')
axis([0,(t1+t2+t3+0.001),0,P1/1000+100])

figure(3)
%subplot(2,2,4)
plot(u(1:o)*1000,R(1:o)/1000,'k')
title('Reaction Force vs Displacement')
xlabel('Displacement [mm]')
ylabel('Force [kN]')
```

C.2 Resisting Forces

```
function [R,m,ucr,uperm,uel]=Rforce(u,i,R,K,ucr,uspl,M,kfac,Fpl,uperm,uel)
%-------------------------------------------------------------------------%
% Resisting Forces
% Calculating the resisting forces for the different regions
%-------------------------------------------------------------------------%
m=0;

%% Elastic Range %%

    if u(i)<uel
        R(i)=K(1)*u(i)-K(1)*uperm;
        m=kfac(1)*M;
    end


%% Elastoplatic Range %%
    if uel<=u(i) && u(i)<uspl
        R(i)=K(1)*ucr+K(2)*(u(i)-ucr);
        m=kfac(2)*M;
        uperm=(u(i)-R(i)/K(1));
        uel=u(i);
    end

%% Elastplastic Final Range &&

    if uspl<u(i)&& R(i)<Fpl && uel<u(i)
        R(i)=K(1)*ucr+K(2)*(u(i)-ucr);
        m=kfac(3)*M;
        uperm=u(i)-(R(i)/K(1));
        %(u(i))-R(i)/K(1))
        uel=u(i);
    end
%% Plastic Range %%

    if R(i)>=Fpl
        R(i)=Fpl;
        uel=u(i);
        m=kfac(3)*M;
        uperm=u(i)-(R(i)/K(1));
    end
end
```

C.3 Central Difference Method

```
function [u,a,v,k,F,o,R] = CDM(M,K,C,F,n,t_step,ucr,uspl,upl,Fpl,Fcr,h)
%%%%%%%%%%%%%%%%%%%%%%%%%%%%%%%%%%%%%%%%%%%%%%%%%%%%%%%%%%%%%%%%%%%%%%%%%%%%%%%%
%   Central difference method for trilinear material
%   Adam Johansson - Johan Fredberg
%   2015-03-16
%%%%%%%%%%%%%%%%%%%%%%%%%%%%%%%%%%%%%%%%%%%%%%%%%%%%%%%%%%%%%%%%%%%%%%%%%%%%%%%%
%------ Predefining ------%
u=zeros(1,n);               % [m] Displacement
v=zeros(1,n);               % [m/s] Velocity
a=zeros(1,n);               % [m/s^2] Acceleration
k=zeros(1,n);               % [N/m] Stiffness
R=zeros(1,n);               % [N] Reaction Force

%------ Transformation Factors ------%
%Elastic range
kmel=0.486;
%Plastic range
kmpl=1/3;
%Elasto-plastic range
kmelpl=(kmel+kmpl)/2;
kfac=[kmel,kmelpl,kmpl];
%------ Initial Conditions ------%
u(1)=0;
a(1)=0;
o=0;
uel=ucr;
%------ Starting Values ------%
u0=u(1)-t_step*v(1)+(t_step^2/2)*a(1);
uperm=0;
%------ Loop ------%
for i=1:n
  o=o+1;
  if (i-1)==0
    [R,m,ucr,uperm,uel]=Rforce(u0,i,R,K,ucr,uspl,M,kfac,Fpl,uperm,uel);
    me=(1/t_step^2)*m+(1/2*t_step)*C;
    Fe=F(i)-R(i)+(2/t_step^2)*m*u(i)-((1/t_step^2)*m-(1/2*t_step)*C)*u0;
    u(i+1)=Fe*(me^-1);
    a(i+1)=(1/t_step^2)*(u0-2*u(i)+u(i+1));
    v(i+1)=(1/2*t_step)*(-u0+u(i+1));
    k(i)=K(1);
  else
    [R,m,ucr,uperm,uel]=Rforce(u,i,R,K,ucr,uspl,M,kfac,Fpl,uperm,uel);
    me=(1/t_step^2)*m+(1/2*t_step)*C;
```

```
        Fe=F(i)-R(i)+(2/t_step^2)*m*u(i)...
        -((1/t_step^2)*m-(1/2*t_step)*C)*u(i-1);
        u(i+1)=Fe*(me^-1);
        a(i+1)=(1/t_step^2)*(u(i-1)-2*u(i)+u(i+1));
        v(i+1)=(1/2*t_step)*(-u(i-1)+u(i+1));
        k(i)=K(1);
    end
end
```

D Reinforcement with different material models

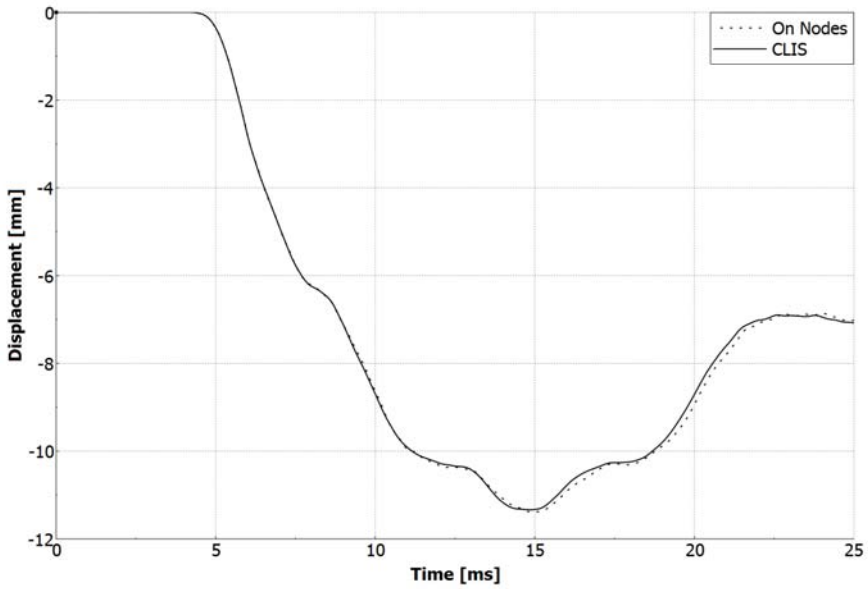

Figure 4.1: *Beam Case 1 using CDPM2-Bilinear with reinforcement constrained by CLIS and on nodes.*

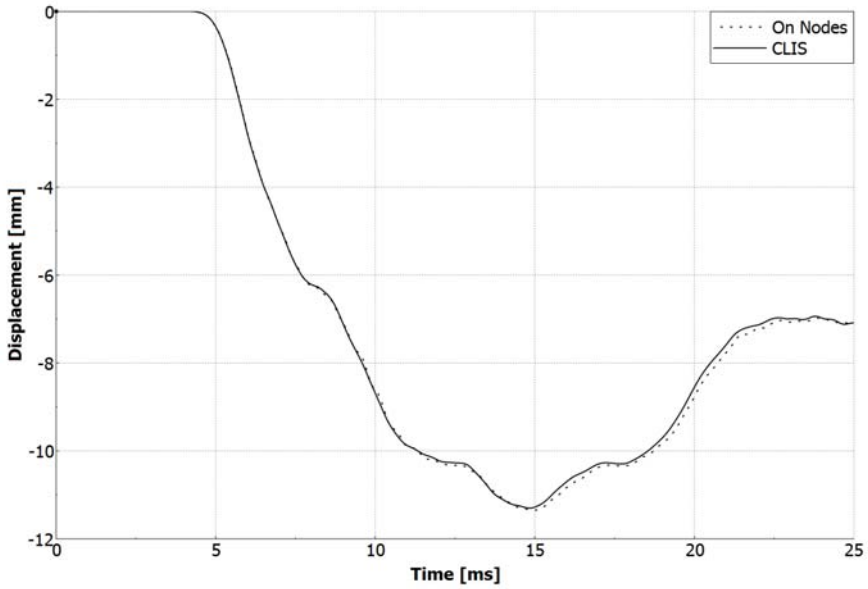

Figure 4.2: *Beam Case 1 using CDPM2-Linear with reinforcement constrained by CLIS and on nodes.*

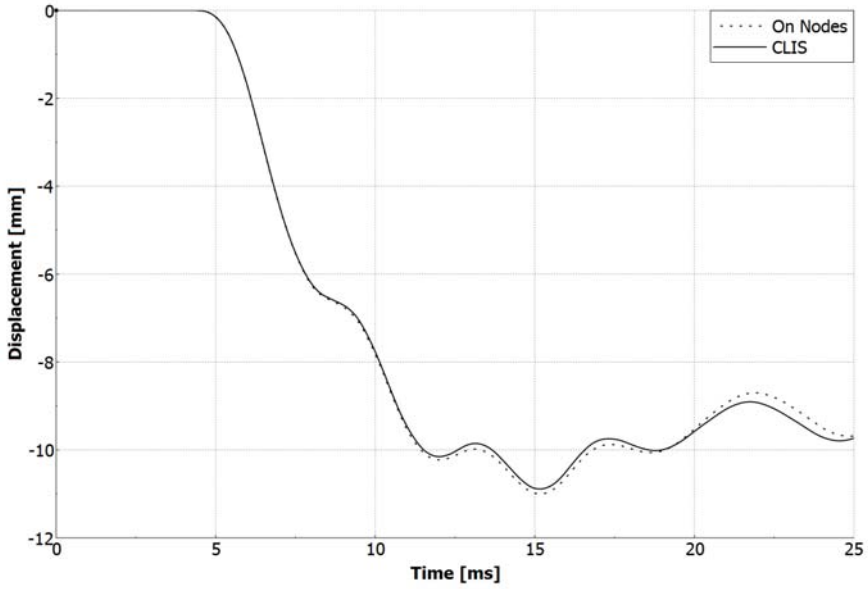

Figure 4.3: *Beam Case 1 using CSCM with reinforcement constrained by CLIS and on nodes.*

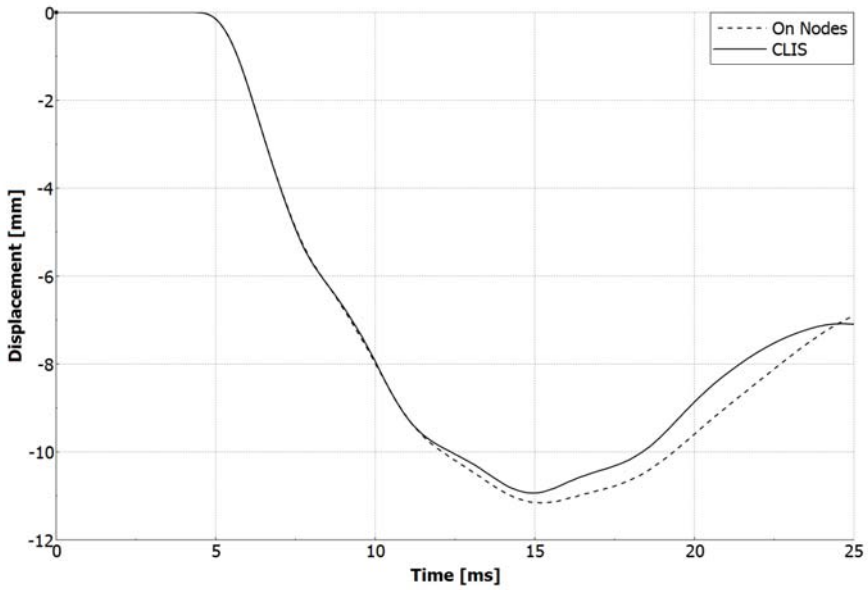

Figure 4.4: *Beam Case 1 using Winfrith with reinforcement constrained by CLIS and on nodes.*

E Mathcad calculations

On the following pages the hand calculations performed in MathCad are presented for the different beam cases.

E.1 Capacity for Beam Case 1

Geometries

$L := 1.4m$ $h := 0.25m$ $b := 0.15m$

$\phi_{top} := 0.016m$ $\phi_{bottom} := 0.016m$

$n_{top} := 2$ $n_{bottom} := 2$

$c_{concrete.cover} := 0.032m$

$l_{concrete.element} := 0.01m$

Material data

$f_c := 42MPa$ $f_t := 3.045MPa$ $E_c := 29.279GPa$

$\varepsilon_{cu} := 0.0035$ $\alpha_R := 0.81$ $\beta_R := 0.416$

Reinforcement B500B

$E_s := 200GPa$ $f_s := 426MPa$ $\varepsilon_{sy} := \frac{f_s}{E_s} = 2.13 \times 10^{-3}$

Modular ratios

$\alpha := \frac{E_s}{E_c} = 6.831$

Uncracked beam, state I

Cross sectional data, state I

$$d := h - \left(c_{concrete.cover} + \frac{\phi_{bottom}}{2} \right) = 0.21\,m$$

$$d' := c_{concrete.cover} + \frac{\phi_{top}}{2} = 0.04\,m$$

$$A_c := b \cdot h = 0.038\,m^2$$

$$A_s := n_{bottom} \cdot \pi \cdot \left(\frac{\phi_{bottom}^2}{4} \right) = 4.021 \times 10^{-4}\,m^2 \qquad A'_s := n_{top} \cdot \pi \cdot \left(\frac{\phi_{top}^2}{4} \right) = 4.021 \times 10^{-4}\,m^2$$

$$A_I := b \cdot h + (\alpha - 1) \cdot A'_s + (\alpha - 1) \cdot A_s = 0.042\,m^2$$

$$x_1 := \frac{(b \cdot h) \cdot \frac{h}{2} + \left[(\alpha - 1) \cdot A'_s \right] \cdot d' + \left[(\alpha - 1) \cdot A_s \right] \cdot d}{A_I} = 0.125\,m$$

$$I_I := \frac{b \cdot h^3}{12} + b \cdot h \cdot \left(\frac{h}{2} - x_1 \right)^2 + (\alpha - 1) \cdot A'_s \cdot \left(x_1 - d' \right)^2 + (\alpha - 1) \cdot A_s \cdot \left(d - x_1 \right)^2 = 2.292 \times 10^{-4}\,m^4$$

Cracking moment

$$z_{bottom} := \left(h - \frac{l_{concrete.element}}{2} \right) - x_1 = 0.12\,m$$

$$M_{cr} := \frac{f_t \cdot I_I}{z_{bottom}} = 5.816 \cdot kN \cdot m$$

Cracking load

$$P_{cr} := \frac{4 \cdot M_{cr}}{L} = 16.617 \cdot kN$$

$$P_{cr.DYNA} := 17.31 kN$$

$$\Delta_{crackingload} := \frac{P_{cr}}{P_{cr.DYNA}} = 0.96$$

Deflection at midspan just before cracking

Since the beam is simply supported and the stiffness, EI, is constant along the beam, elementary cases can be used to solve the midspan deflection

$$u_{mid} := \frac{P_{cr} \cdot L^3}{48 \cdot E_c \cdot I_I} = 0.142 \cdot mm$$

$$u_{mid.DYNA} := 0.178mm$$

$$\Delta_{deflection} := \frac{u_{mid}}{u_{mid.DYNA}} = 0.795$$

Cracked beam, state II

The midspan deflection will be calculated for a load that is greater than the cracking load but still well below the ultimate capacity of the beam.

The centre of gravity, and hence also the neutral layer, will change when the beam cracks.

Cross sectional data, state II

Centre of gravity for the cracked section

$$x_{cg} := 0.1m$$

$$x_{CG} := root\left[\left[b \cdot x_{cg} \cdot \frac{x_{cg}}{2} + (\alpha - 1) \cdot A'_s \cdot \left(x_{cg} - d'\right) - \alpha \cdot A_s \cdot \left(d - x_{cg}\right)\right], x_{cg}\right]$$

$$x_{CG} = 0.067\,m$$

$$A_{II} := b \cdot x_{CG} + (\alpha - 1)A'_s + \alpha \cdot A_s = 0.015\,m^2$$

$$I_{II} := \frac{b \cdot x_{CG}^3}{12} + b \cdot x_{CG} \cdot \left(\frac{x_{CG}}{2} - x_{CG}\right)^2 + (\alpha - 1) \cdot A'_s \cdot \left(x_{CG} - d'\right)^2 + \alpha \cdot A_s \cdot \left(d - x_{CG}\right)^2 = 7.291 \times 10^{-5}\,m$$

Deflection at midbeam, state II

$P := 40kN$

$R_A := \frac{P}{2} = 20 \cdot kN$

It is necessary to decide what part of the beam that is cracked/uncracked for this particular load.

Cracking moment

$M_{cr} = 5.816 \cdot kN \cdot m$

Derivation of sectional forces gives:

$x_{cr} := \frac{M_{cr}}{R_A} = 0.291\,m$

Max moment in the span:

$M_{max} := \frac{P \cdot L}{4} = 14 \cdot kN \cdot m$

Curvatures

Max curvature for the uncracked section:

$\kappa_I := \frac{M_{cr}}{E_c \cdot I_I} = 8.667 \times 10^{-4} \frac{1}{m}$

Min curvature for the cracked section:

$\kappa_{II.min} := \frac{M_{cr}}{E_c \cdot I_{II}} = 2.724 \times 10^{-3} \frac{1}{m}$

Max curvature for the cracked section:

$\kappa_{II.max} := \frac{M_{max}}{E_c \cdot I_{II}} = 6.558 \times 10^{-3} \frac{1}{m}$

"Areas" and "leverarms" for the curvature distributions

$$A_{01} := \frac{\kappa_I \cdot x_{cr}}{2} = 1.26 \times 10^{-4} \qquad x_{01} := x_{cr} \cdot \frac{2}{3} = 0.194\,m$$

$$A_{02} := \kappa_{II.min} \cdot \left(\frac{L}{2} - x_{cr}\right) = 1.115 \times 10^{-3} \qquad x_{02} := x_{cr} + \frac{\left(\frac{L}{2} - x_{cr}\right)}{2} = 0.495\,m$$

$$A_{03} := \frac{\left(\kappa_{II.max} - \kappa_{II.min}\right) \cdot \left(\frac{L}{2} - x_{cr}\right)}{2} = 7.844 \times 10^{-4} \qquad x_{03} := x_{cr} + \left(\frac{L}{2} - x_{cr}\right) \cdot \frac{2}{3} = 0.564\,m$$

Deflection at midbeam in state II

$$u_{mid.state.II} := A_{01} \cdot x_{01} + A_{02} \cdot x_{02} + A_{03} \cdot x_{03} = 1.019 \cdot mm$$

$$u_{mid.state.II.DYNA} := 0.81mm$$

$$\Delta_{deflection.state.II} := \frac{u_{mid.state.II}}{u_{mid.state.II.DYNA}} = 1.258$$

Ultimate capacity, state III

The concrete strain limitation is assumed to be decisive.

First assumption

Top reinforcement does not yield

Bottom reinforcement does yield

$$\sigma'_{s1}(x_1) := E_s \cdot \left(\frac{d' - x_1}{x_1} \right) \cdot \varepsilon_{cu}$$

$$\sigma_{s1} := f_s = 426 \cdot MPa$$

Horizontal equilibrium, (first assumption)

$$x_1 := 0.05m$$

$$x_1 := root\left[\left[\alpha_R \cdot x_1 \cdot b \cdot f_c - \sigma'_{s1}(x_1) A'_s - (\sigma_{s1} \cdot A_s) \right], x_1 \right]$$

$$x_1 = 0.037\,m$$

Observe that the compressive zone is located above the top reinforcement. Hence the horizontal equilibrium as well as the definition of the steel strain for the top reinforcement is changed.

Control of assumptions, (first assumption)

$$\varepsilon_{sy} = 2.13 \times 10^{-3}$$

$$\varepsilon'_{s1} := \frac{d' - x_1}{x_1} \cdot \varepsilon_{cu} = 2.432 \times 10^{-4}$$ Does not yield

$$\varepsilon_{s1} := \frac{d - x_1}{x_1} \cdot \varepsilon_{cu} = 0.016$$ Yields

Assumptions correct!

Ultimate moment capacity when the concrete strain limit is desicive

Moment equilibrium at the level of the bottom reinforcement:

$$M_{Rd} := \alpha_R \cdot x_1 \cdot b \cdot f_c \cdot \left(d - \beta_R \cdot x_1\right) - \sigma'_{s1}\left(x_1\right) \cdot A'_s \cdot (d - d') = 33.787 \cdot kN \cdot m$$

$$P_{ultimate} := \frac{4 \cdot M_{Rd}}{L} = 96.533 \cdot kN$$

$$P_{ultimate.DYNA} := 100.4kN$$

$$\Delta_{P.ultimate} := \frac{P_{ultimate}}{P_{ultimate.DYNA}} = 0.961$$

Cross sectional data, state II

Centre of gravity for the cracked section

$$x_{cg} := 0.1m$$

$$x_{CG} := root\left[\left[b \cdot x_{cg} \cdot \frac{x_{cg}}{2} + (\alpha - 1) \cdot A'_s \cdot \left(x_{cg} - d'\right) - \alpha \cdot A_s \cdot \left(d - x_{cg}\right)\right], x_{cg}\right]$$

$$x_{CG} = 0.067\,m$$

$$A_{II} := b \cdot x_{CG} + (\alpha - 1)A'_s + \alpha \cdot A_s = 0.015\,m^2$$

$$I_{II} := \frac{b \cdot x_{CG}^3}{12} + b \cdot x_{CG} \cdot \left(\frac{x_{CG}}{2} - x_{CG}\right)^2 + (\alpha - 1) \cdot A'_s \cdot \left(x_{CG} - d'\right)^2 + \alpha \cdot A_s \cdot \left(d - x_{CG}\right)^2 = 7.291 \times 10^{-5}\,m^4$$

Deflection at midspan just before failure

The deflection just before failure will only be calculated approximately since it will only serve as a rough comparison to the ultimate deflection in the FE-model. The approximation lies within the assumption that the beam is fully cracked along its length. I.e. the moment of inertia for state II, I_{II} are valid along the whole beam and elementary cases can be used to solve the deflection.

$$u_{mid.ultimate} := \frac{P_{ultimate} \cdot L^3}{48 E_c \cdot I_{II}} = 2.585 \cdot mm$$

$$u_{mid.ultimate.DYNA} := 3.06mm$$

$$\Delta_{deflection.ultimate} := \frac{u_{mid.ultimate}}{u_{mid.ultimate.DYNA}} = 0.845$$

Ultimate capacity, state III

The ultimate capacity is calculated when the yield strain of the reinforcement is desicive

The steel strain is known, while the concrete strain at the top side of the beam is unknown. Hence the concrete strain must be guessed and iterated until the calculations conforms.

Ultimate strains for concrete and reinforcement

$\varepsilon_{cu} = 3.5 \times 10^{-3}$ $\varepsilon_{sy} = 2.13 \times 10^{-3}$

Guessing a value of the concrete strain

$\text{scalefactor} := 0.253$

$\varepsilon_{cc.guessed} := \text{scalefactor} \cdot \varepsilon_{cu} = 8.855 \times 10^{-4}$

Which gives the stress block factors:

$$\text{alpha}_{interpolation} := 0.347 + (0.417 - 0.347) \cdot \frac{(0.886 - 0.8)}{1.0 - 0.8} = 0.377$$

$$\text{beta}_{interpolation} := 0.346 + (0.350 - 0.346) \cdot \frac{(0.886 - 0.8)}{1.0 - 0.8} = 0.348$$

$\alpha := 0.377$ $\beta := 0.348$

Calculation of the compressive zone based on the strain distribution

$$x := \frac{\varepsilon_{cc.guessed}}{\varepsilon_{cc.guessed} + \varepsilon_{sy}} \cdot d = 0.062\,m$$

Horizontal equilibrium

$$\alpha \cdot f_c \cdot x \cdot b + A'_s \cdot E_s \cdot \left(\frac{x - d'}{x} \cdot \varepsilon_{cc.guessed} \right) = f_s \cdot A_s$$

The horizontal equilibrium equation should be true if the guessed concrete strain was correct

Left hand side of the equation: $\alpha \cdot f_c \cdot x \cdot b + A'_s \cdot E_s \cdot \left(\frac{x - d'}{x} \cdot \varepsilon_{cc.guessed} \right) = 171.486 \cdot kN$

Right hand side of the equation: $f_S \cdot A_S = 171.305 \cdot kN$

Ultimate moment capacity when the steel yield limit is decisive

Moment equilibrium at the level of the bottom reinforcement:

$$M_{Rd} := \alpha \cdot x \cdot b \cdot f_c \cdot (d - \beta \cdot x) + E_s \cdot \left(\frac{x - d'}{x} \cdot \varepsilon_{cc.guessed} \right) \cdot A'_s \cdot (d - d') = 31.868 \cdot kN \cdot m$$

$$P_{ultimate} := \frac{4 \cdot M_{Rd}}{L} = 91.051 \cdot kN$$

$$P_{ultimate.DYNA} := 100.4kN$$

$$\Delta_{P.ultimate} := \frac{P_{ultimate}}{P_{ultimate.DYNA}} = 0.907$$

E.2 Verification of Beam Case II during tensioning

Geometry

$L := 2.4m$ $h := 0.220m$ $b := 0.220m$

$\phi_{top} := 0.012m$ $\phi_{bottom} := 0.012m$ $\phi_{p} := 0.013m$

$n_{top} := 2$ $n_{bottom} := 2$

$c_{concrete.cover} := 0.02m$

$l_{concrete.element} := 0.01m$

$e_{excentricity} := 0.05m$

Material data

$f_c := 48MPa$ $f_t := 3.177MPa$ $E_c := 30.65GPa$

Reinforcement B500B

$E_s := 210GPa$ $f_s := 500MPa$ $\varepsilon_{sy} := \frac{f_s}{E_s} = 2.381 \times 10^{-3}$

Prestressing steel Compacted 7-wire strand

$E_p := 210GPa$ $f_{p.yield} := 1590MPa$ $f_{p.ultimate} := 1860MPa$

Modular ratios

$\alpha := \frac{E_s}{E_c} = 6.852$ $\alpha_p := \frac{E_p}{E_c} = 6.852$

Prestressed beam with straight prestressing wire

The beam has a straight prestressing wire placed with an excentricity of 50 mm. There is no bond between the concrete and the prestressing steel during the tensioning phase, hence the following calculations will be based on the **"Tendon force approach"**.

Top reinforcement consists of two ϕ12 bars, concrete cover 20mm.
Bottom reinforcement consists of two ϕ12 bars, concrete cover 20mm.

Cross sectional data

$$d := h - \left(c_{concrete.cover} + \frac{\phi_{bottom}}{2} \right) = 0.194\,m$$

$$d' := c_{concrete.cover} + \frac{\phi_{top}}{2} = 0.026\,m$$

$$d_p := \frac{h}{2} + e_{excentricity} = 0.16\,m$$

$$A_c := b \cdot h = 0.048\,m^2 \qquad A_p := \pi \cdot \left(\frac{\phi_p^{\,2}}{4} \right) = 1.327 \times 10^{-4}\,m^2$$

$$A_s := n_{bottom} \cdot \pi \cdot \left(\frac{\phi_{bottom}^{\,2}}{4} \right) = 2.262 \times 10^{-4}\,m^2 \qquad A'_s := n_{top} \cdot \pi \cdot \left(\frac{\phi_{top}^{\,2}}{4} \right) = 2.262 \times 10^{-4}\,m^2$$

$$A_{net} := A_c - A_p + (\alpha - 1) \cdot A_s + (\alpha - 1) \cdot A'_s = 0.051\,m^2$$

$$x_1 := \frac{(b \cdot h) \cdot \frac{h}{2} + \left[(\alpha - 1) \cdot A'_s \right] \cdot d' + \left[(\alpha - 1) \cdot A_s \right] \cdot d}{A_{net}} = 0.11\,m$$

$$I_{I.net} := \frac{b \cdot h^3}{12} + b \cdot h \cdot \left(\frac{h}{2} - x_1 \right)^2 + (\alpha - 1) \cdot A'_s \cdot \left(x_1 - d' \right)^2 + (\alpha - 1) \cdot A_s \cdot \left(d - x_1 \right)^2 = 2.139 \times 10^{-4}\,m^4$$

Calculation of cross sectional stresses

When using the "Tendon force approach" the stress calculations is based on the actual initial prestressing force, P_i

$\sigma_{pi} := 1238\text{MPa}$

$P_i := \sigma_{pi} \cdot A_p = 164.323 \cdot \text{kN}$

Initial stresses

Concrete stresses (top side of the beam)

$$z_{top} := -\left(x_1 - \frac{l_{concrete.element}}{2}\right) = -0.105\,\text{m}$$

$$\sigma_{top} := \frac{-P_i}{A_{net}} + \frac{-P_i \cdot e_{excentricity}}{I_{I.net}} \cdot z_{top} = 0.817 \cdot \text{MPa} \qquad \sigma_{top.DYNA} := -0.75\text{MPa}$$

Difference:

$$\Delta_{concrete.stresses.top} := \frac{\sigma_{top}}{\left|\sigma_{top.DYNA}\right| + \left|\sigma_{top}\right|} = 0.521$$

Concrete stresses (bottom side of the beam)

$$z_{bottom} := \left(h - \frac{l_{concrete.element}}{2}\right) - x_1 = 0.105\,\text{m}$$

$$\sigma_{bottom} := \frac{-P_i}{A_{net}} + \frac{-P_i \cdot e_{excentricity}}{I_{I.net}} \cdot z_{bottom} = -7.25 \cdot \text{MPa} \qquad \sigma_{bottom.DYNA} := -7.20\text{MPa}$$

Difference:

$$\Delta_{concrete.stresses.bottom} := \frac{\sigma_{bottom}}{\sigma_{bottom.DYNA}} = 1.007$$

Steel stresses in the top reinforcement

$z_{top.steel} := -(x_1 - d') = -0.084\,m$

$\sigma_{top.steel.level} := \frac{-P_i}{A_{net}} + \frac{-P_i \cdot e_{excentricity}}{I_{I.net}} \cdot z_{top.steel} = 0.01 \cdot MPa$

$\sigma_{top.steel} := \sigma_{top.steel.level} \cdot \alpha = 0.07 \cdot MPa$ $\sigma_{top.steel.DYNA} := -0.2MPa$

Difference:

$\Delta_{steel.stresses.top} := \frac{\sigma_{top.steel}}{|\sigma_{top.steel.DYNA}| + |\sigma_{top.steel}|} = 0.259$

Steel stresses in the bottom reinforcement

$z_{bottom.steel} := d - x_1 = 0.084\,m$

$\sigma_{bottom.steel.level} := \frac{-P_i}{A_{net}} + \frac{-P_i \cdot e_{excentricity}}{I_{I.net}} \cdot z_{bottom.steel} = -6.443 \cdot MPa$

$\sigma_{bottom.steel} := \sigma_{bottom.steel.level} \cdot \alpha = -44.145 \cdot MPa$ $\sigma_{bottom.steel.DYNA} := -43.5MPa$

Difference:

$\Delta_{steel.stresses.bottom} := \frac{\sigma_{bottom.steel}}{\sigma_{bottom.steel.DYNA}} = 1.015$

Steel stresses in the prestressing steel

$z_p := e_{excentricity} = 0.05\,m$

$\sigma_{p.steel.level} := \frac{-P_i}{A_{net}} + \frac{-P_i \cdot e_{excentricity}}{I_{I.net}} \cdot z_p = -5.148 \cdot MPa$

$\sigma_p := \frac{P_i}{A_p} + \sigma_{p.steel.level} \cdot \alpha_p = 1.203 \times 10^3 \cdot MPa$ $\sigma_{p.DYNA} := 1238MPa$

Difference:

$\Delta_{prestressing.steel} := \frac{\sigma_p}{\sigma_{p.DYNA}} = 0.972$

Calculation of the midspan deflection due to the prestressing force

In this case the prestressing force is the only contribution to the curvature of the beam. The curvature is based on the "Tendon force approach".

Curvature contribution from the prestressing force

$$M_{max} := -P_i \cdot e_{excentricity} = -8.216 \cdot kN \cdot m$$

$$\kappa := \frac{M_{max}}{E_c \cdot I_{I.net}} = -1.253 \times 10^{-3} \frac{1}{m}$$

$$A := \kappa \cdot \frac{L}{2} = -1.504 \times 10^{-3}$$

$$x := \frac{L}{2} \cdot \frac{1}{2} = 0.6\,m$$

Deflection at midspan

$$u_{mid} := A \cdot x = -0.902 \cdot mm \qquad u_{midDYNA} := -0.870mm$$

Difference:

$$\Delta_{deflection} := \frac{u_{mid}}{u_{midDYNA}} = 1.037$$

E.3 Capacity for Beam Case 2

The following calculations aims at obtaining the cracking load, P_{cr}, the ultimate load, P_u, and mid-beam defelction, u_{mid}, for the prestressed beam.
A comparison is made with the FE-model in order to verify that the hand calculations and the FE-model corresponds to each other.
The calculations is based on "Design and analysis of prestressed concrete structures" by B.Engström, which is a summarization of the calculation principles stated in Eurocode 5.

In the FE-model there is no strain compatibility between the prestressing steel and the concrete during the tensioning of the beam. However, just before the external load is applied on the beam "*CONSTRAINED_LAGRANGE_IN_SOLID"-contact is introduced between the prestressing ste and the surrounding concrete. This contact provides strain compatibility between the materials, hence the calculations in this sheet can be based on the **"Strain compatibility approach"**.

Geometry

$L := 2.4m$ $h := 0.220m$ $b := 0.220m$

$\phi_{top} := 0.012m$ $\phi_{bottom} := 0.012m$ $\phi_p := 0.013m$

$n_{top} := 2$ $n_{bottom} := 2$

$c_{concrete.cover} := 0.02m$

$l_{concrete.element} := 0.01m$

Material data

$f_c := 48\text{MPa}$ $f_t := 3.177\text{MPa}$ $E_c := 30.65\text{GPa}$

Reinforcement

$f_s := 500\text{MPa}$ $E_s := 210\text{GPa}$ $\varepsilon_{sy} := \frac{f_s}{E_s} = 2.381 \times 10^{-3}$

Prestressing steel Compacted 7-wire strand

$E_p := 210\text{GPa}$ $f_{p.yield} := 1590\text{MPa}$ $f_{p.ultimate} := 1860\text{MPa}$

$E_{p.strainhardening} := 2100\text{MPa}$ (From LS-DYNA)

Modular ratios

$\alpha := \frac{E_s}{E_c} = 6.852$ $\alpha_p := \frac{E_p}{E_c} = 6.852$

Calculation for the uncracked beam

Cross sectional data

$e_{excentricity} := 0.05\text{m}$

$d := h - \left(c_{concrete.cover} + \frac{\phi_{bottom}}{2} \right) = 0.194\,\text{m}$

$d' := c_{concrete.cover} + \frac{\phi_{top}}{2} = 0.026\,\text{m}$

$d_p := \frac{h}{2} + e_{excentricity} = 0.16\,\text{m}$

$A_c := b \cdot h = 0.048\,\text{m}^2$ $A_p := \pi \cdot \left(\frac{\phi_p^{\,2}}{4} \right) = 1.327 \times 10^{-4}\,\text{m}^2$

$A_s := n_{bottom} \cdot \pi \cdot \left(\frac{\phi_{bottom}^{\,2}}{4} \right) = 2.262 \times 10^{-4}\,\text{m}^2$ $A'_s := n_{top} \cdot \pi \cdot \left(\frac{\phi_{top}^{\,2}}{4} \right) = 2.262 \times 10^{-4}\,\text{m}$

$A_I := b \cdot h + (\alpha - 1) \cdot A'_s + (\alpha - 1) \cdot A_s + (\alpha_p - 1) \cdot A_p = 0.052\,\text{m}^2$

$$x_1 := \frac{(b \cdot h) \cdot \frac{h}{2} + \left[(\alpha - 1) \cdot A'_s\right] \cdot d' + \left[(\alpha - 1) \cdot A_s\right] \cdot d + \left[(\alpha - 1) \cdot A_p\right] \cdot d_p}{A_I} = 0.111\,\text{m}$$

$$I_I := \frac{b \cdot h^3}{12} + b \cdot h \cdot \left(\frac{h}{2} - x_1\right)^2 + (\alpha - 1) \cdot A'_s \cdot \left(x_1 - d'\right)^2 + (\alpha - 1) \cdot A_s \cdot \left(d - x_1\right)^2 \ldots = 2.158 \times 10^{-4}\,\text{m}^4$$
$$+ \left(\alpha_p - 1\right) \cdot A_p \cdot \left(d_p - x_1\right)^2$$

Cracking moment

$$\sigma_{pi} := 1238\text{MPa}$$

$$P_{0i.guess} := 130\text{kN}$$

$$P_{0i} := \text{root}\left[\left[\sigma_{pi} - \frac{P_{0i.guess}}{A_p} - \alpha_p \cdot \left(\frac{-P_{0i.guess}}{A_I}\right)\right], P_{0i.guess}\right]$$

$$P_{0i} = 167.258 \cdot \text{kN}$$

$$z_{bottom} := \left(h - \frac{l_{concrete.element}}{2}\right) - x_1 = 0.104\,\text{m}$$

$$M_{cr} := \frac{I_I}{z_{bottom}} \cdot \left[f_t + \frac{P_{0i}}{A_I} + \frac{\left(P_{0i} \cdot e_{excentricity}\right) \cdot z_{bottom}}{I_I}\right] = 21.62 \cdot \text{kN} \cdot \text{m}$$

Cracking load

$$P_{cr} := \frac{4 \cdot M_{cr}}{L} = 36.034 \cdot \text{kN}$$

$$P_{cr.DYNA} := 38.28\text{kN}$$

$$\Delta_{crackingload} := \frac{P_{cr}}{P_{cr.DYNA}} = 0.941$$

Deflection at midbeam due to cracking load and prestressing force

The deflection of the beam is increased by the applied point load while it is counteracted by the prestressing effect.

Curvature distribution due to the applied point load, Pcr

$$R_A := \frac{P_{cr}}{2} = 18.017 \cdot kN$$

$$M_{cr.max} := \frac{P_{cr} \cdot L}{4} = 21.62 \cdot kN \cdot m$$

$$\kappa_{.Pcr} := \frac{M_{cr.max}}{E_c \cdot I_I} = 3.269 \times 10^{-3} \frac{1}{m}$$

$$A_{.Pcr} := \frac{\kappa_{.Pcr} \cdot \frac{L}{2}}{2} = 1.961 \times 10^{-3}$$

$$x_{.Pcr} := \frac{L}{2} \cdot \frac{2}{3} = 0.8\,m$$

Curvature distribution due to the applied prestressing force, P_{0i}

$$M_{max.prestressing} := P_{0i} \cdot e_{excentricity} = 8.363 \cdot kN \cdot m$$

$$\kappa_{prestressing} := \frac{M_{max.prestressing}}{E_c \cdot I_I} = 1.264 \times 10^{-3} \frac{1}{m}$$

$$A_{prestressing} := \kappa_{prestressing} \cdot \frac{L}{2} = 1.517 \times 10^{-3}$$

$$x_{prestressing} := \frac{L}{2} \cdot \frac{1}{2} = 0.6\,m$$

Deflection at midspan just before cracking

$u_{mid} := A_{.Pcr} \cdot x_{.Pcr} - \left(A_{prestressing} \cdot x_{prestressing}\right) = 0.659 \cdot mm$

$u_{mid.DYNA} := 0.776mm$

Difference:

$\Delta_{deflection} := \frac{u_{mid}}{u_{mid.DYNA}} = 0.849$

Ultimate capacity of the prestressed beam

In the ULS-calculations full strain compatibility is assumed between the prestressing steel and surrounding concrete. I.e. the calculations is based on the "**Strain compatibility approach**".

Material data

$\alpha_R := 0.810$ $\beta_R := 0.416$

$f_{p.ultimate} = 1.86 \times 10^3 \cdot MPa$ $f_{p.yield} = 1.59 \times 10^3 \cdot MPa$

$\varepsilon_{p.ultimate} := 0.035$ $\varepsilon_{p.yield} := \frac{f_{p.yield}}{E_p} = 7.571 \times 10^{-3}$

$\varepsilon_{p0inf} := \frac{P_{0i}}{E_p \cdot A_p} = 6.001 \times 10^{-3}$

$\varepsilon_{cc.ultimate} := 0.0035$

Calculation when the concrete strain limitation is decisive

First assumption

Top reinforcement does not yield

Prestressing steel does not yield

Bottom reinforcement does yield

$$\sigma_{s.top1}(x_{01}) := E_s \cdot \left(\frac{x_{01} - d'}{x_{01}} \right) \cdot \varepsilon_{cc.ultimate}$$

$$\varepsilon_{p1}(x_{01}) := \left(\frac{d_p - x_{01}}{x_{01}} \right) \cdot \varepsilon_{cc.ultimate} + \varepsilon_{p0inf}$$

$$\sigma_{p1}(x_{01}) := E_p \cdot \varepsilon_{p1}(x_{01})$$

$$\sigma_{s.bottom1} := f_s = 500 \cdot MPa$$

Horizontal equilibrium, (first assumption)

$$x_{01.guess} := 0.07m$$

$$x_{01} := root\left[\begin{matrix} \alpha_R \cdot f_c \cdot b \cdot x_{01.guess} + \sigma_{s.top1}(x_{01.guess}) \cdot A'_s \cdots \\ + \left(-\sigma_{s.bottom1} \cdot A_s - \sigma_{p1}(x_{01.guess}) \cdot A_p \right) \end{matrix} \right], x_{01.guess}$$

$$x_{01} = 0.049\,m$$

Control of assumptions, (first assumption)

$\varepsilon_{sy} = 2.381 \times 10^{-3}$

$\varepsilon_{p.yield} = 7.571 \times 10^{-3}$

$\varepsilon_{p.ultimate} = 0.035$

$\varepsilon'_{s1} := \frac{x_{01} - d'}{x_{01}} \cdot \varepsilon_{cc.ultimate} = 1.652 \times 10^{-3}$ No yielding

$\varepsilon_{s1} := \frac{d - x_{01}}{x_{01}} \cdot \varepsilon_{cc.ultimate} = 0.01$ Yielding

$\varepsilon_{p1} := \frac{d_p - x_{01}}{x_{01}} \cdot \varepsilon_{cc.ultimate} + \varepsilon_{p0inf} = 0.014$ Yielding
No snapping

Assumptions not correct!

New assumptions has to be made

Second assumption

Top reinforcement does not yield

Prestressing steel does yield

Bottom reinforcement does yield

$\sigma_{s.top2}(x_{02}) := E_s \cdot \left(\frac{x_{02} - d'}{x_{02}} \right) \cdot \varepsilon_{cc.ultimate}$

$\sigma_{p2} := f_{p.yield} = 1.59 \times 10^{3} \cdot MPa$

$\sigma_{s.bottom2} := f_s = 500 \cdot MPa$

Horizontal equilibrium, (second assumption)

$x_{02.guess} := 0.07m$

$x_{02} := root\left[\left(\alpha_R \cdot f_c \cdot b \cdot x_{02.guess} + \sigma_{s.top2}\left(x_{02.guess}\right) \cdot A'_s - \sigma_{s.bottom2} \cdot A_s - \sigma_{p2} \cdot A_p\right), x_{02.guess}\right]$

$x_{02} = 0.034\,m$

Control of assumptions, (second assumption)

$\varepsilon_{sy} = 2.381 \times 10^{-3}$

$\varepsilon_{p.yield} = 7.571 \times 10^{-3}$

$\varepsilon_{p.ultimate} = 0.035$

$\varepsilon'_{s2} := \frac{x_{02} - d'}{x_{02}} \cdot \varepsilon_{cc.ultimate} = 7.86 \times 10^{-4}$ No yielding

$\varepsilon_{s2} := \frac{d - x_{02}}{x_{02}} \cdot \varepsilon_{cc.ultimate} = 0.017$ Yielding

$\varepsilon_{p2} := \frac{d_p - x_{02}}{x_{02}} \cdot \varepsilon_{cc.ultimate} + \varepsilon_{p0inf} = 0.019$ Yielding
No snapping

Assumptions correct!

Ultimate moment capacity

Moment equilibrium at the level of the prestressing steel:

$M_{Rd} := \alpha_R \cdot f_c \cdot b \cdot x_{02} \cdot \left(d_p - \beta_R \cdot x_{02}\right) \ldots + \sigma_{s.top2}\left(x_{02}\right) \cdot A'_s \cdot \left(d_p - d'\right) + \sigma_{s.bottom2} \cdot A_s \cdot \left(d - d_p\right) = 50.737 \cdot kN \cdot m$

$P_{ultimate} := \frac{4 \cdot M_{Rd}}{L} = 84.561 \cdot kN$ $P_{ultimate.DYNA} := 99.222kN$

$\Delta_{ultimate.deflection} := \frac{P_{ultimate}}{P_{ultimate.DYNA}} = 0.852$

Deflection at midspan just before failure

The centre of gravity, and hence also the neutral layer, will change when the beam cracks.

Cross sectional data, state II

Centre of gravity for the cracked section

$x_{cg} := 0.1m$

$$x_{CG} := \text{root}\left[\left[b \cdot x_{cg} \cdot \frac{x_{cg}}{2} + (\alpha - 1) \cdot A'_s \cdot \left(x_{cg} - d'\right) - \alpha \cdot A_s \cdot \left(d - x_{cg}\right) - \alpha_p \cdot A_p \cdot \left(d_p - x_{cg}\right)\right], x_{cg}\right]$$

$x_{CG} = 0.051\,m$

$x_{CG} := 0.034m$

$$A_{II} := b \cdot x_{CG} + (\alpha - 1)A'_s + \alpha \cdot A_s + \alpha_p \cdot A_p = 0.011\,m^2$$

$$I_{II} := \frac{b \cdot x_{CG}^3}{12} + b \cdot x_{CG} \cdot \left(\frac{x_{CG}}{2} - x_{CG}\right)^2 + (\alpha - 1) \cdot A'_s \cdot \left(x_{CG} - d'\right)^2 \ldots = 5.708 \times 10^{-5}\,m^4$$
$$+ \alpha \cdot A_s \cdot \left(d - x_{CG}\right)^2 + \alpha_p \cdot A_p \cdot \left(d_p - x_{CG}\right)^2$$

Deflection at midspan just before failure

Curvature distribution due to the applied point load, $P_{ultimate}$

$P_{ultimate} = 84.561 \cdot kN$

$$M_{max.ultimate} := \frac{P_{ultimate} \cdot L}{4} = 50.737 \cdot kN \cdot m$$

Regions with positive curvature distribution

$$\kappa_{.Pultimate} := \frac{M_{max.ultimate}}{E_c \cdot I_{II}} = 0.029\,\frac{1}{m}$$

$$A_{.Pultimate} := \frac{\kappa_{.Pultimate} \cdot \frac{L}{2}}{2} = 0.017$$

$$x_{.Pultimate} := \frac{L}{2} \cdot \frac{2}{3} = 0.8\,m$$

Curvature distribution due to the applied prestressing force, P_{0i}

$$M_{max.prestressing.ultimate} := P_{0i} \cdot e_{excentricity} = 8.363 \cdot kN \cdot m$$

$$\kappa_{prestressing.ultimate} := \frac{M_{max.prestressing.ultimate}}{E_c \cdot I_I} = 1.264 \times 10^{-3} \frac{1}{m}$$

$$A_{prestressing.ultimate} := \kappa_{prestressing.ultimate} \cdot \frac{L}{2} = 1.517 \times 10^{-3}$$

$$x_{prestressing.ultimate} := \frac{L}{2} \cdot \frac{1}{2} = 0.6\,m$$

Deflection at midspan just before failure

$$u_{mid.ultimate} := A_{.Pultimate} \cdot x_{.Pultimate} - \left(A_{prestressing.ultimate} \cdot x_{prestressing.ultimate}\right) = 13.01 \cdot mm$$

$$u_{mid.ultimate.DYNA} := 10.6mm$$

Difference:

$$\Delta_{deflection.ultimate} := \frac{u_{mid.ultimate}}{u_{mid.ultimate.DYNA}} = 1.227$$

E.4 Capacity for Beam Case 3

Geometries

$L := 2.4m$ $h := 0.22m$ $b := 0.22m$

$\phi_{top} := 0.012m$ $\phi_{bottom} := 0.012m$ $\phi_{p} := 0.013m$

$n_{top} := 2$ $n_{bottom} := 2$

$c_{concrete.cover} := 0.02m$

$l_{concrete.element} := 0.01m$

Material data

$f_c := 48MPa$ $f_t := 3.177MPa$ $E_c := 30.65GPa$

$\varepsilon_{cu} := 0.0035$ $\alpha_R := 0.81$ $\beta_R := 0.416$

Reinforcement B500B

$E_s := 210GPa$ $f_s := 500MPa$ $\varepsilon_{sy} := \frac{f_s}{E_s} = 2.381 \times 10^{-3}$

Prestressing steel Compacted 7-wire strand

$E_p := 210GPa$ $f_{p.ultimate} := 1860MPa$ $f_{p.yield} := 1590MPa$

$\varepsilon_{p.yield} := \frac{f_{p.yield}}{E_p} = 7.571 \times 10^{-3}$ $\varepsilon_{p.ultimate} := 0.035$

Modular ratios

$\alpha := \frac{E_s}{E_c} = 6.852$ $\alpha_p := \frac{E_p}{E_c} = 6.852$

Uncracked beam, state I

Cross sectional data, state I

$e_{excentricity} := 0.05m$

$d := h - \left(c_{concrete.cover} + \frac{\phi_{bottom}}{2} \right) = 0.194\,m$

$d' := c_{concrete.cover} + \frac{\phi_{top}}{2} = 0.026\,m$

$d_p := \frac{h}{2} + e_{excentricity} = 0.16\,m$

$A_c := b \cdot h = 0.048\,m^2$

$A_p := \pi \cdot \left(\frac{\phi_p^{\,2}}{4} \right) = 1.327 \times 10^{-4}\,m^2$

$A_s := n_{bottom} \cdot \pi \cdot \left(\frac{\phi_{bottom}^{\,2}}{4} \right) = 2.262 \times 10^{-4}\,m^2$

$A'_s := n_{top} \cdot \pi \cdot \left(\frac{\phi_{top}^{\,2}}{4} \right) = 2.262 \times 10^{-4}\,m^2$

$A_I := b \cdot h + (\alpha - 1) \cdot A'_s + (\alpha - 1) \cdot A_s + (\alpha_p - 1) \cdot A_p = 0.052\,m^2$

$$x_1 := \frac{(b \cdot h) \cdot \frac{h}{2} + \left[(\alpha - 1) \cdot A'_s \right] \cdot d' + \left[(\alpha - 1) \cdot A_s \right] \cdot d + \left[(\alpha - 1) \cdot A_p \right] \cdot d_p}{A_I} = 0.111\,m$$

$$I_I := \frac{b \cdot h^3}{12} + b \cdot h \cdot \left(\frac{h}{2} - x_1 \right)^2 + (\alpha - 1) \cdot A'_s \cdot \left(x_1 - d' \right)^2 \ldots + \left[(\alpha - 1) \cdot A_s \cdot \left(d - x_1 \right)^2 + (\alpha_p - 1) \cdot A_p \cdot \left(d_p - x_1 \right)^2 \right] = 2.158 \times 10^{-4}\,m^4$$

Cracking moment

$$z_{bottom} := \left(h - \frac{l_{concrete.element}}{2} \right) - x_1 = 0.104\,m$$

$$M_{cr} := \frac{f_t \cdot I_I}{z_{bottom}} = 6.577 \cdot kN \cdot m$$

Cracking load

$$P_{cr} := \frac{4 \cdot M_{cr}}{L} = 10.961 \cdot kN$$

$$P_{cr.DYNA} := 11.44kN$$

$$\Delta_{crackingload} := \frac{P_{cr}}{P_{cr.DYNA}} = 0.958$$

Deflection at midspan just before cracking

$$u_{mid} := \frac{P_{cr} \cdot L^3}{48 \cdot E_c \cdot I_I} = 0.477 \cdot mm$$

$$u_{mid.DYNA} := 0.542mm$$

$$\Delta_{deflection} := \frac{u_{mid}}{u_{mid.DYNA}} = 0.881$$

Ultimate capacity, state III

The concrete strain limitation is assumed to be decisive.

First assumption

Top reinforcement does not yield

Prestressing steel does not yield

Bottom reinforcement does yield

$$\sigma'_{s1}(x_1) := E_s \cdot \left(\frac{x_1 - d'}{x_1}\right) \cdot \varepsilon_{cu}$$

$$\sigma_{p1}(x_1) := E_s \cdot \left(\frac{d_p - x_1}{x_1}\right) \varepsilon_{cu}$$

$$\sigma_{s1} := f_s = 500 \cdot \text{MPa}$$

Horizontal equilibrium, (first assumption)

$$x_1 := 0.05\text{m}$$

$$x_1 := \text{root}\left[\left(\alpha_R \cdot x_1 \cdot b \cdot f_c + \sigma'_{s1}(x_1)\, A'_s - \sigma_{p1}(x_1) \cdot A_p - \sigma_{s1} \cdot A_s\right), x_1\right]$$

$$x_1 = 0.04\,\text{m}$$

Control of assumptions, (first assumption)

$$\varepsilon_{sy} = 2.381 \times 10^{-3}$$

$$\varepsilon_{p.yield} = 7.571 \times 10^{-3}$$

$$\varepsilon_{p.ultimate} = 0.035$$

$$\varepsilon'_{s1} := \frac{x_1 - d'}{x_1} \cdot \varepsilon_{cu} = 1.24 \times 10^{-3}$$ Does not yield

$$\varepsilon_{s1} := \frac{d - x_1}{x_1} \cdot \varepsilon_{cu} = 0.013$$ Yields — Assumptions not correct!

$$\varepsilon_{p1} := \frac{d_p - x_1}{x_1} \cdot \varepsilon_{cu} = 0.01$$ Yields, No snapping

Second assumption

Top reinforcement does not yield

Prestressing steel does yield

Bottom reinforcement does yield

$$\sigma'_{s2}(x_2) := E_s \cdot \left(\frac{x_2 - d'}{x_2} \right) \cdot \varepsilon_{cu}$$

$$\sigma_{p2} := f_{p.yield} = 1.59 \times 10^3 \cdot MPa$$

$$\sigma_{s2} := f_s = 500 \cdot MPa$$

Horizontal equilibrium, (second assumption)

$$x_2 := 0.05m$$

$$x_2 := root\left[\left(\alpha_R \cdot x_2 \cdot b \cdot f_c + \sigma'_{s2}(x_2) A'_s - \sigma_{p2} \cdot A_p - \sigma_{s2} \cdot A_s \right), x_2 \right]$$

$$x_2 = 0.034\,m$$

Control of assumptions, (second assumption)

$$\varepsilon_{sy} = 2.381 \times 10^{-3}$$

$$\varepsilon_{p.yield} = 7.571 \times 10^{-3}$$

$$\varepsilon_{p.ultimate} = 0.035$$

$$\varepsilon'_{s2} := \frac{x_2 - d'}{x_2} \cdot \varepsilon_{cu} = 7.86 \times 10^{-4}$$ No yielding

$$\varepsilon_{s2} := \frac{d - x_2}{x_2} \cdot \varepsilon_{cu} = 0.017$$ Yields — Assumptions correct!

$$\varepsilon_{p2} := \frac{d_p - x_2}{x_2} \cdot \varepsilon_{cu} = 0.013$$ Yields
No snapping

Ultimate moment capacity when the concrete strain limit is desicive

Moment equilibrium at the level of the prestressing steel:

$$M_{Rd} := \sigma'_{s1}(x_2)\cdot A'_s\cdot(d_p - d') + \alpha_R\cdot x_2\cdot b\cdot f_c\cdot(d_p - \beta_R\cdot x_2) + \sigma_{s1}\cdot A_s\cdot(d - d_p) = 50.737\cdot kN\cdot m$$

$$P_{ultimate} := \frac{4\cdot M_{Rd}}{L} = 84.561\cdot kN$$

$$P_{ultimate.DYNA} := 93.50kN$$

$$\Delta_{P.ultimate} := \frac{P_{ultimate}}{P_{ultimate.DYNA}} = 0.904$$

Deflection at midspan just before failure

The centre of gravity, and hence also the neutral layer, will change when the beam cracks.

Cross sectional data, state II

Centre of gravity for the cracked section

$$x_{cg} := 0.1m$$

$$x_{CG} := root\left[\left[b\cdot x_{cg}\cdot\frac{x_{cg}}{2} + (\alpha - 1)\cdot A'_s\cdot(x_{cg} - d') - \alpha\cdot A_s\cdot(d - x_{cg}) - \alpha_p\cdot A_p\cdot(d_p - x_{cg})\right], x_{cg}\right]$$

$$x_{CG} = 0.051\,m$$

$$A_{II} := b\cdot x_{CG} + (\alpha - 1)A'_s + \alpha\cdot A_s + \alpha_p\cdot A_p = 0.015\,m^2$$

$$I_{II} := \frac{b\cdot x_{CG}^{\,3}}{12} + b\cdot x_{CG}\cdot\left(\frac{x_{CG}}{2} - x_{CG}\right)^2 + (\alpha - 1)\cdot A'_s\cdot(x_{CG} - d')^2 \ldots = 5.305\times 10^{-5}\,m^4$$
$$+\left[\alpha\cdot A_s\cdot(d - x_{CG})^2 + \alpha_p\cdot A_p\cdot(d_p - x_{CG})^2\right]$$

Deflection at midspan just before failure

The deflection just before failure will only be calculated approximately since it will only serve as a rough comparison to the ultimate deflection in the FE-model. The approximation lies within the assumption that the beam is fully cracked along its length. I.e. the moment of inertia for state II, I_{II} are valid along the whole beam and elementary cases can be used to solve the deflection.

$$u_{mid.ultimate} := \frac{P_{ultimate} \cdot L^3}{48 E_c \cdot I_{II}} = 14.977 \cdot mm$$

$$u_{mid.ultimate.DYNA} := 33.71mm$$

$$\Delta_{ultimate.deflection} := \frac{u_{mid.ultimate}}{u_{mid.ultimate.DYNA}} = 0.444$$